Development of Infrared Imaging Bolometer and Measurement of 3-D Plasma Radiation Structure in LHD

Naoko Ashikawa

DOCTOR OF PHILOSOPHY

Department of Fusion Science

School of Mathematical and Physical Science

The Graduate University for Advanced Studies

2001

Abstract

A new bolometer system using an infrared (IR) camera has been developed to measure the 3-D structure of plasma radiation. This bolometer is called the IR imaging bolometer (IRIB) and of this diagnostic there are two types of the mask pattern that are known as the Segmented Mask Infrared Imaging Bolometer (SIB) and the Infrared Imaging Video Bolometer (IRVB). The incident radiation power coming from the plasma is collimated by an aperture and then absorbed by a thin foil located in the vacuum vessel. An IR camera outside of the vacuum vessel measures the temperature rise of the foil by means of the thermal radiation that passes through the vacuum interface by means of an IR vacuum window. Therefore, this system does not use electrical vacuum feed-throughs, and has a very simple design as described above, compared to conventional resistive bolometers. The difference between the two IR bolometer systems is in how the spatial channels are determined. The spatial channels of the SIB foil are physically defined and separated by the segmented mask and those of the IRVB are determined by numerically dividing up the space on a single large foil exposed to the plasma radiation.

In this study, the design, production and installation of the two differential types of IRIB systems were made for LHD.

The mask was designed by taking into consideration the incident power of the radiation. For a sufficient signal-to-noise ratio of the detected foil temperature, a thin metal foil was used in the mask, aluminum with a thickness of about 0.8 μm for the SIB system and gold with a thickness of about 1 μm for the IRVB system were selected. The other parts of these systems including the aperture plate, the light shielding pipe and the support of the IR camera were also designed.

After the installation of these IR bolometers, an in-situ calibration experiment was done. The common parameters for both systems, the calibration factor (K/mW) and the cooling decay times, were measured using a He-Ne laser as a known radiation source. For the SIB system, the calibration was done for each channel and for the IRVB system, a combination of in-situ calibration and model

profile of the temperature rise of the foil was used.

Using these coefficients, the plasma radiation power density at the foil was calculated from the two-dimensional temperature distribution of the foil as measured by the IR camera. This resulted in images of the plasma radiation intensity with a sufficient signal and a time response to demonstrate the usefulness of this two-dimensional diagnostic system for plasma radiation.

The merits of the IR bolometer are as follows:

1. Broad two-dimensional radiation brightness profiles are measured by one IR camera using infrared camera imaging technology.

2. Electrical vacuum feed-throughs are not necessary in this system as the information about the foil temperature is passed as IR radiation through an IR vacuum window to the IR camera.

3. One IR bolometer has over one hundred spatial channels.

4. For the case of the IRVB, these spatial channels can be determined after the plasma experiments with flexibility depending on the experimental objectives and the conditions of the plasma.

In the latter half of this thesis, some experimental results are shown using the IRVB data. At present two IRVBs are installed, one at an upper port and the other at a tangential port, and began to measure the plasma radiation from two directions simultaneously during the 2001-2002 experimental campaign in LHD. Both of these IRVB view the same field period and use a 1 μm thick gold foil. The frame rates of these IR cameras are 15 Hz for that with the tangential view and 60 Hz for that with the view from the upper port.

Initial measurements with the IRVB at the tangential port show the variations of the radiative structure as two-dimensional brightness profiles and are compared to data from resistive bolometer arrays, the visible CCD camera and the magnetic field line simulation. Images from two different limiter experiments show the source of the radiation to be localized near the plasma-limiting surface. Also comparison with the magnetic field line calculation shows the structure of a hollow radiation profile in the helical geometry of LHD during standard discharges using the natural helical divertor.

In particular, a change in the radiation structure was observed as a continuous series of images or movie made by the IRVB as the discharge passes through asymmetric radiative collapse.

Finally, using data from the two IRVBs, the three-dimensional position of the radiation source in the field of view of the two cameras was determined during the collapse. The brightness source region of the inboard asymmetric collapse was observed to be below the horizontal midplane at the vertically elongated cross-section of the plasma and this region continued in an axisymmetric manner in the field of view of the two cameras (approximately half of a field period). This was confirmed by qualitative agreement of the measured images with a calculation of the two-dimensional brightness profiles at each camera resulting from an axisymmetric model of the radiation source localized at the lower inboard side of the torus.

Acknowledgements

Contents

1   Introduction

1.1 Objective

The various widely used thin-metal foil resistive bolometer systems are the standard radiation measurement systems for thermal fusion plasma experiments. However, in the case of a future reactor many detectors will be needed, but the cables of these resistive bolometers are subject to noise and vacuum leaks at the feed-through.

With aim of measuring the radiation structure of the three-dimensional plasma in the Large Helical Device (LHD) a new diagnostic system to measure the plasma radiation was envisaged. At the same time, infrared (IR) technology has been developing quickly including IR cameras. Using IR camera technology, a new two-dimensional bolometer diagnostic system was developed. This bolometer is called the IR imaging bolometer (IRIB). In this system only the IR camera is installed outside the vacuum vessel and the thin metal foil is installed inside the vacuum vessel with supporting masks. This system has the ability for two-dimensional measurements and the possibility of gaining three-dimensional information using two IR bolometers, which is an important point for the LHD plasma.

In this thesis, the development of the IR bolometer with two different mask types and the results of images by the IR bolometers are shown. Images from the IRVB of some interesting radiation structures such as the radiation collapse, the wall limiter experiment and the movable limiter experiment are shown. Finally, the three dimensional position of the brightness peak during the asymmetric radiation collapse by two IRVBs with different fields of view is shown.

From the details of the IR bolometer systems and each experimental result, the advantages of the IR bolometer are also shown in this thesis.

1.2 Information on the Large Helical Device (LHD)

The Large Helical Device (LHD) is the largest helical device in the world. LHD is a large-scale superconducting heliotron system in the National Institute for Fusion Science (NIFS) with poloidal and toroidal period numbers l/m = 2/10, and the major and minor radii of R/a = 3.55-4.0/0.5-0.65 m that is shown in Fig. 1.2.1. The maximum magnetic field produced by two superconducting helical coils is about 3 T [1]. The various heating systems of the Electron Cyclotron Heating (ECH), the Ion Cyclotron Resonance Heating (ICRH) and the Neutral Beam Injection (NBI) are installed and flexibly used and combined for each experiment. Three types of gyrotrons with the frequencies of 84 GHz, 82.6 GHz and 168 GHz are used for plasma production and electron heating with a power of 0.45 – 1.9 MW. The main heating systems for the LHD plasma are three NB injectors with a total power of 9 MW.
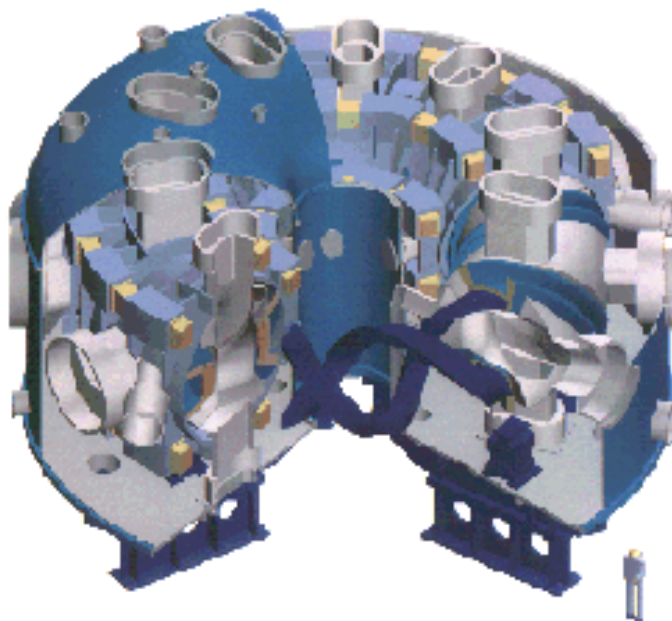
Fig. 1.2.1 The outward form of the Large Helical Device (LHD) in NIFS

1.3   Bolometers in general

Bolometer diagnostics measure the total radiation from the plasma. The wavelengths covered are from the infrared to x-rays. The total radiation power can provide an estimate of the radiation power loss for study of the power balance of plasma [2] and profile information can be used in impurity transport studies, for example breathing plasma [3]. The energy balance of the plasma is estimated from the comparison of the heating input to the radiation and other losses. These diagnostics are important systems for plasma experiments.

1.3.1   Radiation from plasma

The sources of plasma radiation include cyclotron radiation from free electrons, bremsstrahlung from ion-electron interaction, recombination from free-bound transitions, and line radiation of impurities from bound electrons. The strongest source of radiation is the line radiation of impurities. The major intrinsic impurities in LHD are C, O, and Fe [4], but Fe was reduced after changing the diverter plates from stainless steel to carbon.

1.3.2   History of bolometers

The term bolometer means something used to measure heat flux, something like a thermometer. In the study of fusion plasma, it is used to measure energy losses due to plasma radiation. In 1961, a semiconductor type bolometer with a wavelength response of about 1 nm to 1 mm was used in the Perhapsatron S-4 [5]. In 1975, a bolometer having an oxidized nickel film with 25 μm thickness was used in the ATC-tokamak [6].

Since then, these types of semiconductor or metal film resistive bolometers have been used in other tokamaks [7-8]. This technical system was established including a calibration method of the response time, reflectance of wavelength absorption and sensitivity.

The one common thing among these measurement systems is that basically one spatial channel

results from one detector and in general these detectors are connected to one another to make an array. Then one array measures one radial profile at one poloidal cross-section of a device.

G. Apruzzese and G. Tonini had another idea for a bolometer diagnostic using an infrared (IR) camera, which was the first proposal of this type [9]. In addition, semiconductor technology was improved and diodes could also be used to measure radiation from the plasma. Presently, some devices already installed this type of diode [10-11] (shown in the next section) and the bolometer using an IR camera was actually developed for LHD [12-15].

1.3.3   Bolometer detector types

Table 1.3.3.1 shows a comparison of the bolometer detector types used in LHD. At present, three types bolometer systems are installed in LHD and two of these systems are basically the same as those used on other fusion devices. The most popular system is the resistive metal foil bolometer that is a well-established system and is sold commercially [16]. In LHD, ASDEX-type bolometers [16] are used and each bolometer represents one spatial channel. Figure 1.3.3.2 shows a picture of the resistive bolometer array using a gold foil with thickness of 4 μm with 12 channels. The gold foil faces the plasma and the plasma radiation is absorbed by a gold foil. The other side of this foil is attached to the Kapton sheet of insulation and a gold resistive meander grid. Due to the temperature rise on the foil, the resistance of the resistive grid at the backside of the foil changes and this value is transformed into an electrical signal that shows the plasma radiation power. This resistive bolometer has to subtract the change in the temperature of the bolometer mount due to plasma radiation, so the reference channels as shown in Fig. 1.3.3.2 were covered by an aluminum plate.

The field of view (FOV) depends on the pinhole size and its position. At one field period, a wide-angle bolometer was installed and measured the total radiation by normalization to the total radiation power measured by the bolometer array.

The Absolute eXtreme UltraViolet (AXUV) detector is another type of bolometry system as shown in Fig. 1.3.3.2. This detector has a flat spectral power response from ultraviolet to x-ray photon energies as shown in Fig. 1.3.3.4, and with a slightly increased efficiency all the way down to visible wavelengths [11]. This type has a very high time response and does not detect low energy neutrals which point is different from the resistive and IR imaging bolometers. The detectors using the metal foil such as the resistive bolometer and the IR imaging bolometer absorb the plasma radiation and the neutrals, these two sources cannot be separated. To determine the neutral contribution is one problem in estimating the radiation power. By comparing with the AXUV diode, the neutral contribution can be estimated and at present this study is being carried out in LHD.

The third one is the IR imaging bolometer (IRIB). The merits of the IR bolometer relative to other bolometers are flexibility to measure two-dimensional profiles and no electrical feed-throughs for the vacuum vessel. More details are shown in Sec. 1.4.

For various cross-sections of the three dimensional plasma in LHD, bolometer systems were installed.

Table 1.3.3.1   Bolometer Detector Types

Type	Merit	Demerit
• Metal film resistive	• sensitive • rad-hard • good Δt (1 ms) •	• electric -noise • vacuum leak risk • expensive •
• IR bolometer	• 2-D flexible • rad-hard • low \$/ch •	• less sensitive • poor Δt (60 Hz) • fragile •
• AXUV photodiode	• very sensitive • high Δt(100 µs) • no low energy neutrals	• rad-weak • low E_{photon} • electric -noise
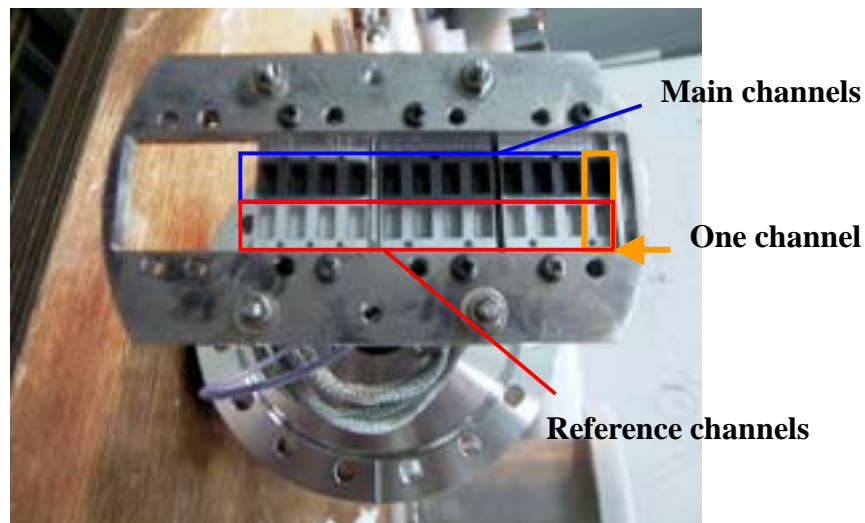
Fig. 1.3.3.2 Picture of the resistive bolometer array with 12 channels in LHD. Each small rectangle is one spatial channel and a gold foil with a thickness of 4 μm is installed in this rectangle. This side looks toward the plasma (photo by B.J. Peterson).
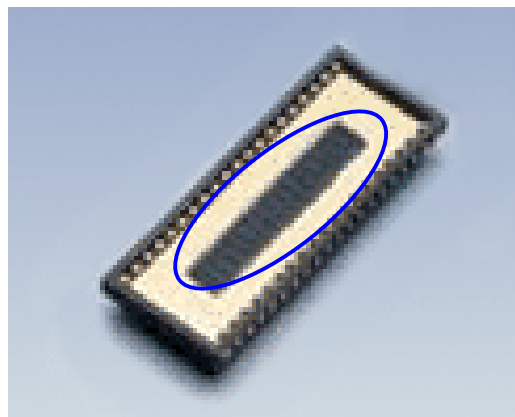
Fig. 1.3.3.3 Picture of the AXUV diode with 16 channels. Inside of the blue line is the array of detectors. The size of one channel is about 2 x 5 mm^2.

(International Radiation Detectors Inc. , www.ird-inc.com)
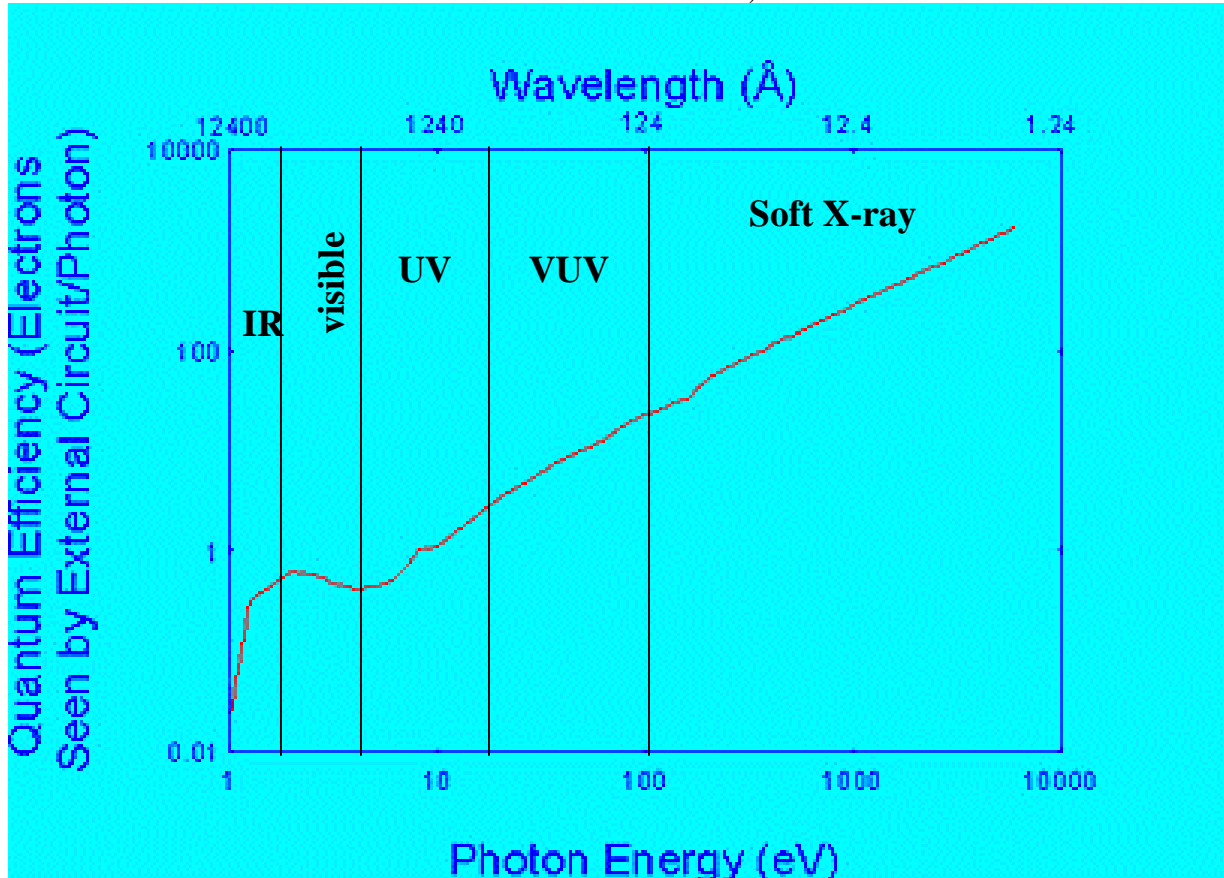
Fig. 1.3.3.4 The quantum efficiency of the AXUV diodes. The quantum efficiency is constant (0.27 A / W) in most of the range (above 10 eV)

1.4   IR imaging bolometer

The first proposal to use an IR camera for a bolometer was by G.Apruzzese and G.Tonini [8]. After this proposal, the concept was revived in 1997 by G.A. Wurden in Los Alamos National Laboratory with sensor based on a two-dimensional segmented matrix of raised absorbers [17]. An original design was considered for LHD called the Segmented mask Infrared imaging Bolometer (SIB) that was also proposed by G.A. Wurden, *et al*. [12]. The SIB is one of the mask types of the IR imaging bolometer. In this proposal, the actual mask design was considered and the model of the detected radiation power density to the metal foil of the SIB was estimated. In addition, the first SIB was tested on the Compact Helical System (CHS) in the National Institute for Fusion Science (NIFS) [13]. This test was only to detect the plasma radiation and the values of radiation signal could not be estimated due to a lack of calibration for each pixel (corresponding to spatial channels as shown in Sec. 1.4.3).

The other concept of a single large foil was proposed as the Infrared Imaging Video Bolometer (IRVB) by B.J. Peterson [14]. The IRVB is the other mask type of the IR bolometer. The spatial channels of the IRVB can be determined after experiments since they are determined by numerical analysis. More details of the IRVB are shown in Sec. 1.4.4.

In this study, new designs for the SIB and the first IRVB were done for LHD and they were manufactured and the installed in LHD prior to the 3rd campaign (1999-2000). In addition, the first steady-state measurement was done using the SIB and the IRVB in LHD. To calibrate both mask types, data were analyzed using the calibration parameters and the resulting radiation power density was shown as a two-dimensional image [15,18]

In Sec. 1.4, the basic concepts of the SIB and the IRVB are shown.

1.4.1   Basic equation for the detected radiation power density

The basic concept of the IR bolometer is to measure the profile of the temperature rise on a

foil by the plasma radiation using the IR camera. For this profile of the temperature on a foil, the two-dimensional heat diffusion equation with a source term and the blackbody radiation effect was estimated as follows,

$$\frac{\partial^2 T}{\partial x^2} + \frac{\partial^2 T}{\partial y^2} = \frac{1}{\kappa}\frac{\partial T}{\partial t} - \zeta_{rad} + \zeta_{bb} \qquad (1.4.1.1)$$

where, T is a temperature on the foil, κ is a thermal diffusivity, ζ_{rad} is the term of due to the incident radiation power to the foil and ζ_{bb} is the term due to the blackbody radiation from the foil. In this equation, the incident radiation power term, ζ_{rad}, and the blackbody radiation term, ζ_{bb}, are shown as follows,

$$\zeta_{rad} = P_{rad}\big/ k \cdot th \cdot A_{pix} \qquad (1.4.1.2)$$

and

$$\zeta_{bb}(x, y, t) = \frac{\varepsilon \sigma_{SB}(T^4 - T_0^{\;4})}{k \cdot th} \qquad (1.4.1.3)$$

where k is thermal conductivity, th is a thickness of a foil, A_{pix} is the area of the bolometer pixel, P_{rad} is the detected radiation power by the IR camera, ε is the blackbody thermal emissivity and σ_{SB} is the Stefan- Boltzmann constant, $\sigma_{SB} = 5.6697 \times 10^{-12}$ [W/(cm^{2}K^4)]. The mask temperature, T_0, (as shown in Sec. 1.4.2) is basically the temperature of the vacuum vessel. The solution for P_{rad} using Eqs. (1.4.1.1) – (1.4.1.3) are shown as follows,

$$P_{rad} = k \cdot th \cdot A_{pix}\left\{\frac{1}{\kappa}\frac{\partial T}{\partial t} - \left(\frac{\partial^2 T}{\partial x^2} + \frac{\partial^2 T}{\partial y^2}\right) + \frac{\varepsilon \sigma_{SB}\left(T^4 - T_0^{\;4}\right)}{k \cdot th}\right\} \qquad (1.4.1.4).$$

For the two-dimensional Laplacian term, different equations are used for the SIB and the IRVB.

1.4.2   Mask

The IR bolometer system uses a metal foil mounted in a mask to absorb the plasma radiation and the infrared (IR) camera measures the temperature rise on the foil. In Sec. 1.4.2, the details of the mask are shown. The detectors of both the SIB and the IRVB consist of one thin metal foil, two

10

masks and tightening bolts.

Figure 1.4.2.1 shows the conceptual cross-section of the IRIB mask. Only the IR camera side was blackened by a carbon spray to have a high IR emissivity of about 0.9. The other side was pure metal foil facing the plasma. Using a gold foil, this IR emissivity is about 0.07 at room temperature, 300K. This metal foil was sandwiched by two masks with the same patterns and bolts were used to tighten the masks and the metal foil. The tightening is important to avoid cross-talk for the SIB (shown in Sec. 3.1.1) and to keep the boundary condition. The exposed region of the metal foil to the plasma is the detecting area.

1.4.3   Segmented mask infrared imaging bolometer

Figure 1.4.3.1(a) shows a picture of the Segmented mask Infrared imaging Bolometer (SIB) for the LHD 3rd campaign. The spatial channels of the SIB are separated by the mask pattern. The small circle represents one pixel as shown in Fig. 1.4.3.1(b). The temperature rise at one pixel is modeled as an infinite solid cylinder (diffusion only in the radial direction), using the equation given by,

$$T(r,t) = \frac{2}{b} \times \frac{S_f}{k \times th} \sum_{m=1}^{\infty} \frac{J_0(\alpha_m \cdot r / b)}{J_1(\alpha_m)} \cdot \frac{1 - \exp\left[-\kappa(\alpha_m / b)^2 \times t\right]}{(\alpha_m / b)^3} \qquad , (1.4.3.1)$$

where k is the thermal conductivity, κ is the thermal diffusivity, S_f is incident power flux density, b is pixel radius, th is a thickness of a foil, r is the radial coordinate, t is the time coordinate, J_0 is the mth order Bessel function of the first kind and α_m is the m -th root of J_0 Bessel function [12,18].

Using this model, the foil radius b and the foil thickness th were varied for various metals to arrive at an optimum set of design parameters for LHD. The total radiation power was estimated to be about 4 MW, and the other parameters, the foil position from the plasma, the pinhole diameter, and the pixel radius were considered. The materials of nickel, titanium, aluminum, gold, carbon beryllium and stainless steel with the parameters, (the thermal conductivity, the thermal diffusivity,

11

the specific heat, and the density) were calculated. With the aim of finding the best material for the thin foil and to keep the signal to noise ratio (SNR) about 30 with the temperature rise over 2 degrees, an aluminum foil of dimensions 150 mm x 150 mm with a thickness of 0.8 μm was chosen for the SIB in the 3rd campaign. For this SNR, the signal was estimated using Eq. (1.4.3.1) and the noise was estimated using the temperature resolution, 80 mK of the IR camera.

The resulting foil segments have $b = 5.25$ mm and the total number of pixels on the mask is 118 limited by the foil size and the bolometer pipe diameter (shown in Sec. 2.2).

In the 4th campaign, the foil was changed to gold with a thickness of 1 μm in order to increase the upper limit of detectable photon energy as shown in Fig. 1.4.3.2. The new SIB mask was made by four gold foils and the total number of pixels is 114 with the pixel radius about 5 mm. This mask was divided at the center in order to use four foils and to maintain strong tightening to avoid cross-talk due to the dishing problem of the masks (more details about cross-talk are shown in Sec. 3.1.1).

At present, the SIB mask has some problems. One is the shadowing of the foil by the copper masks for the plasma radiation and that also may contribute to excessive deposition of carbon spray during its manufacture. The second one is thermal energy losses due to thermal contact by the edge of the pixel to the mask frame and the third one is overlaps of the field of view of the plasma.

On the other hand, one of merits of the SIB is an easy calibration for each pixel due to separate channels and the clearly estimated profile of the thermal source. The second merit is that the support by the mask frame is stronger than with the IRVB. The third one is that estimating thermal diffusion is simple due to the thermal isolation at the pixel edge.

Plasma side

Emissivity (gold foil)   = 0.07 @ 300 K

Mask with the same pattern

Bolt

Metal foil

Blackening by carbon
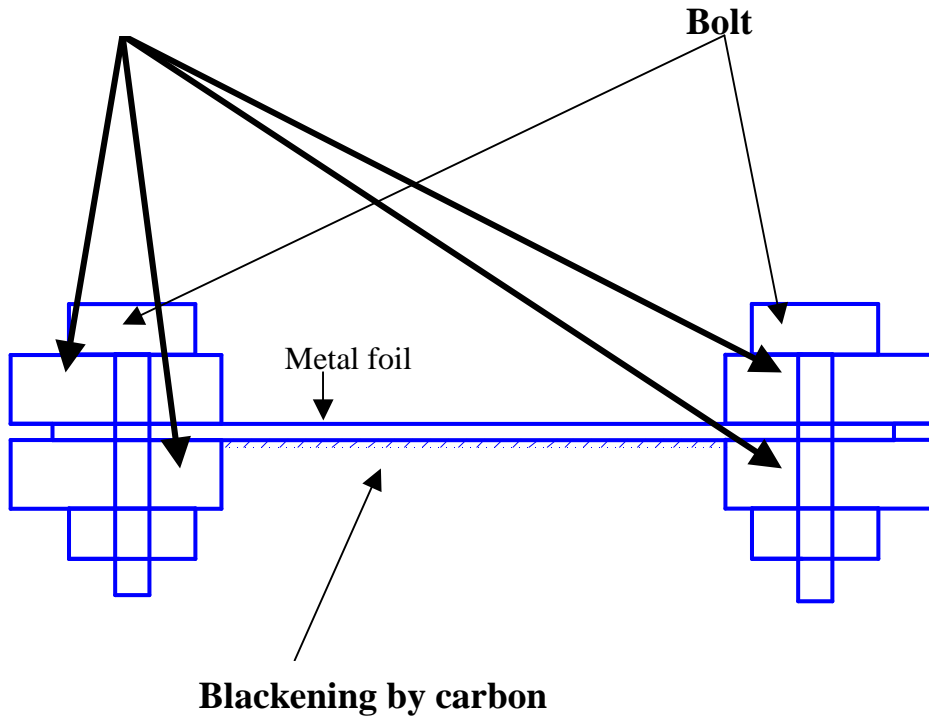
Emissivity (carbon) = 0.9

IR camera side

Fig. 1.4.2.1 Conceptual cross-section of the IRIB mask.
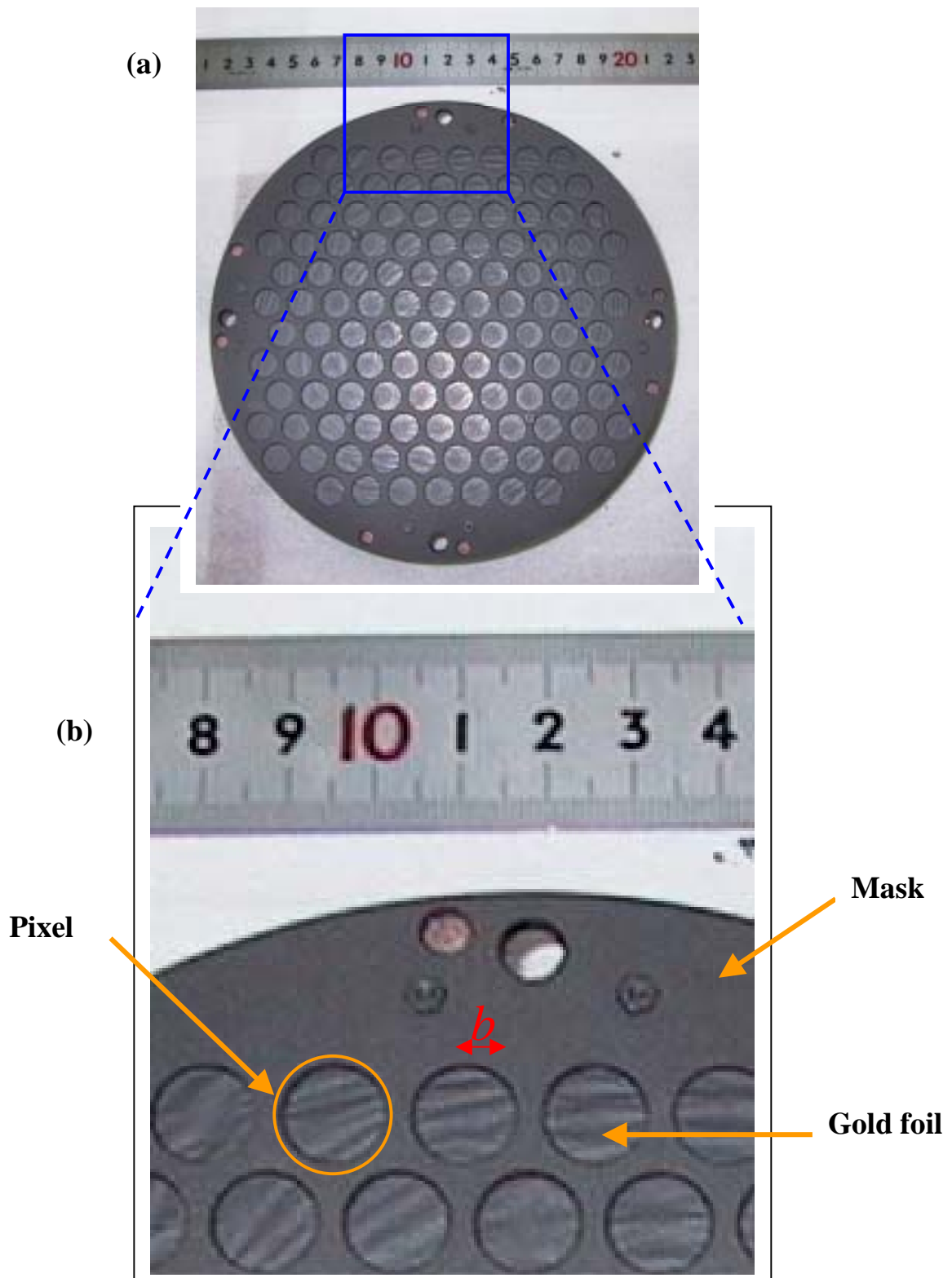
Fig. 1.4.3.1 (a) Picture of the SIB mask and (b) magnified picture of the SIB mask in the LHD 3rd campaign. The small circle shows a pixel with a radius, b = 5.25 mm. Total pixel number is 118. These masks were made at Los Alamos National Laboratory.

(a) Al Density=2.699, Angle=90.deg

2.1 nm

(b) Au Density=19.32, Angle=90.deg
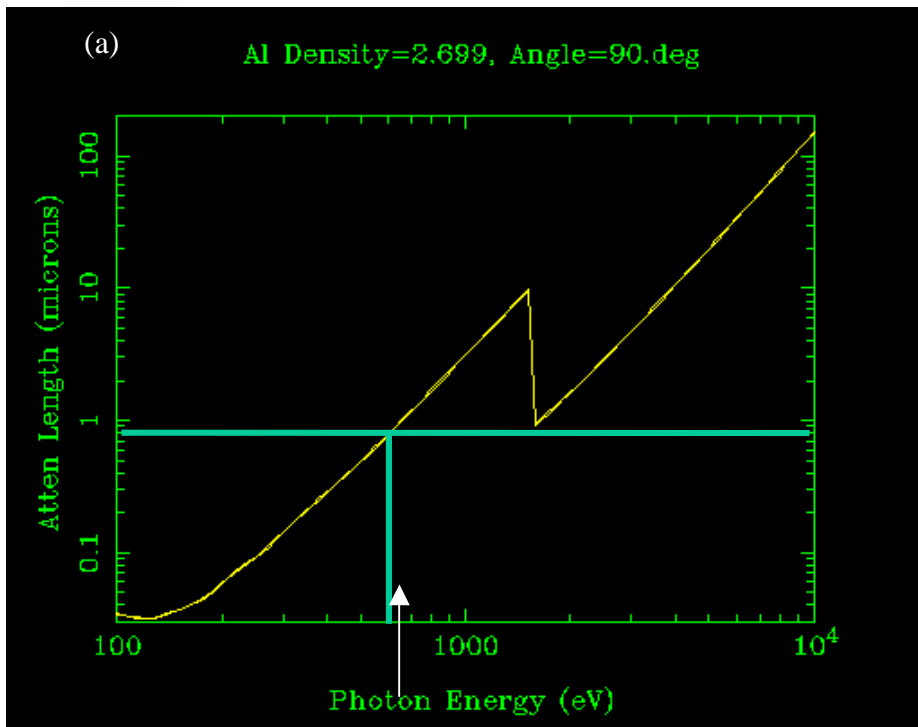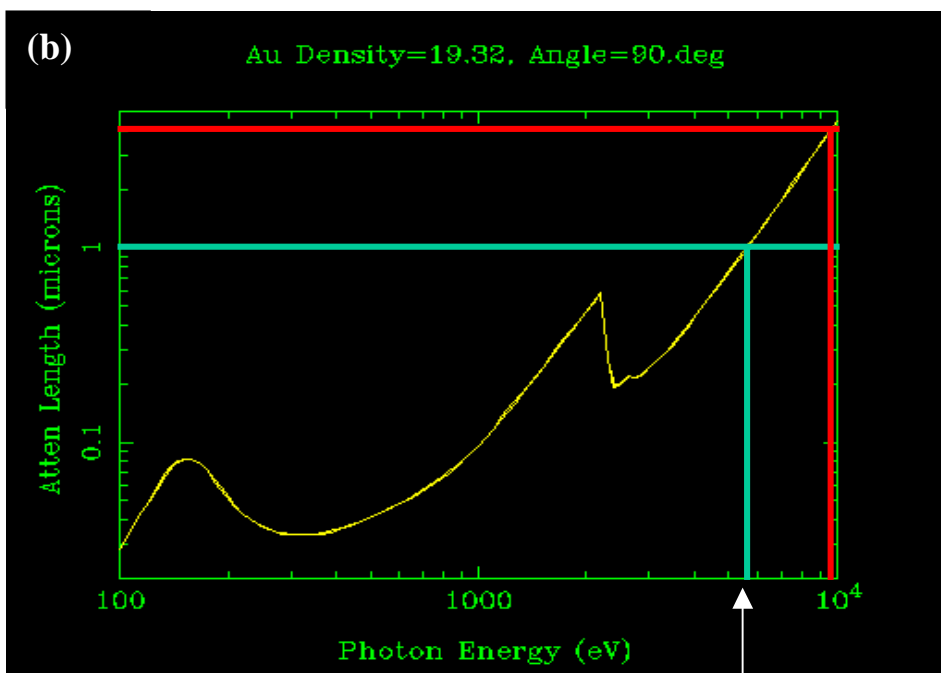
0.25 nm

Fig. 1.4.3.2 Attenuation length of (a) an aluminum and (b) a gold as a thin foil. Using this value for the photon energy, the minimum detected wavelength for each material was estimated.
(Lawrence Berkeley Laboratory, www-cxro.lbl.gov/optical_constants /atten2.html)

15

1.4.4 Infrared imaging video bolometer (IRVB)

The InfraRed imaging Video Bolometer (IRVB) is the other mask type of the IR bolometer with a exposed single large foil [14] as shown in Fig. 1.4.4.1. The large foil is supported only by the mask frames tightened with some bolts as shown in Fig. 1.4.4.2(a). The large exposed area of the foil should be very weak to pressure differences, but foils did not break during the plasma experiments in 1999-2002. So when the IR bolometer system was installed, care had to be taken to reduce the difference of the air pressure on either side of the foil in the vacuum vessel. In addition, when the foil was put on the mask frame, a special stand was used to support the foil.

Figure 1.4.4.2(b) shows the concept of the IRVB that has flexibility in the number of spatial channels that can be decided by the analysis, this means it is possible to determine the number of the spatial channels and the channel size on the foil in terms of the number of IR camera pixels after the experiments. The fundamental difference between the SIB and the IRVB is in how they deal with the thermal diffusion in the foil. Instead of using the copper mask to physically divide the foil into the thermally isolated circular pixel patterns of the SIB mask frames, the entire foil is numerically divided into square pixels of dimension l_{bol}, of the side of the bolometer pixel. The length l_{bol} should be greater than or equal to the length, l_{IR}, the side of the IR pixel, that gives the minimum spatial resolution by the IR camera. At present, the area of the spatial channel, A_{pix}, is equal to l_{bol}^2 for square pixels. The temperature rise, ΔT, of each bolometer pixel during Δt is written as the sum of the temperature rise including the incident power from the plasma radiation and the thermal diffusion from neighboring pixels.

At present, for the two-dimensional Laplacian term of the thermal diffusion in Eq. (1.4.1.4), the forward time center space (FTCS) algorithm was used as follows [20],

$$\frac{\partial^2 T}{\partial x^2} + \frac{\partial^2 T}{\partial y^2} = \frac{T(x, y+l) + T(x, y-l) + T(x+l, y) + T(x-l, y) - 4T(x, y)}{l_{bol}^2} \qquad (1.4.4.1).$$

The stability criterion for the FTCS algorithm is given by [20],

$$l_{bol}{}^2 \geq 2\kappa\Delta t \qquad\qquad\qquad (1.4.4.2).$$

The spatial derivation of the FTCS is calculated at t-Δt and more discussions about the algorithm for the diffusive term including the relationship between time steps are given in Sec. 3.5.

One of merits of the IRVB is the flexibility in the number of spatial channels that can be determined after the experiments. The second one is low influence from the edge of the mask frame including no shadowing of the foil by the mask frame and the thermal energy losses. For the thermal energy losses by the mask frame, that might be reduced using other isolation such as the Teflon sheet in the future. The third one is that simple two-dimensional images are shown on a foil because the images by the SIB system are a complicated due to shadowing by the mask frame between pixels.

On the other hand, one of the demerits is the weak support for the foil. The second one is a complicated calibration method (as shown in Sec. 3.1) due to no-separated spatial channels by the mask frames.

Copper mask frame

Gold foil
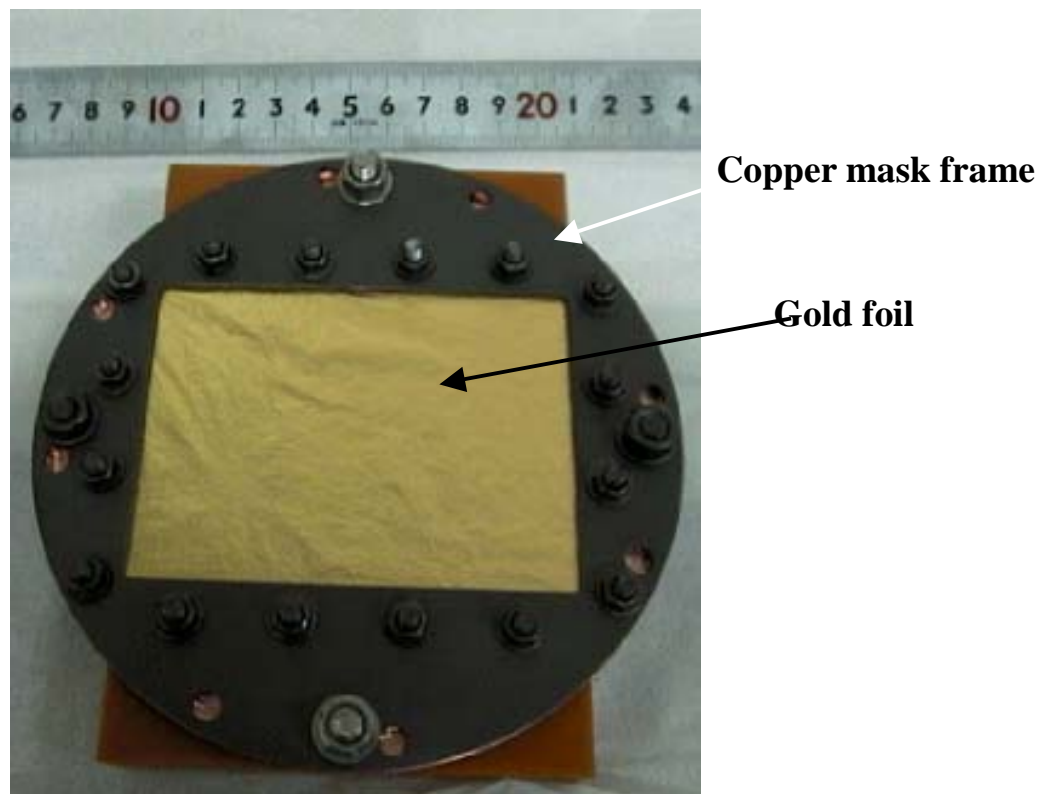
Fig. 1.4.4.1 Picture of the IRVB mask (plasma side). This detected area is 66mm x 90 mm.

90 mm

(a)

holes for clamping bolts

holes for mounting bolts

copper frame

thin metal foil

calibration laser beam size

(b)

IR camera pixel

bolometer pixel

x

y

$T(x,y+l_{bol})$

$T(x-l_{bol},y)$ $T(x,y)$ $T(x+l_{bol},y)$

a

b

$T(x,y-l_{bol})$

l_{IR}

l_{bol}
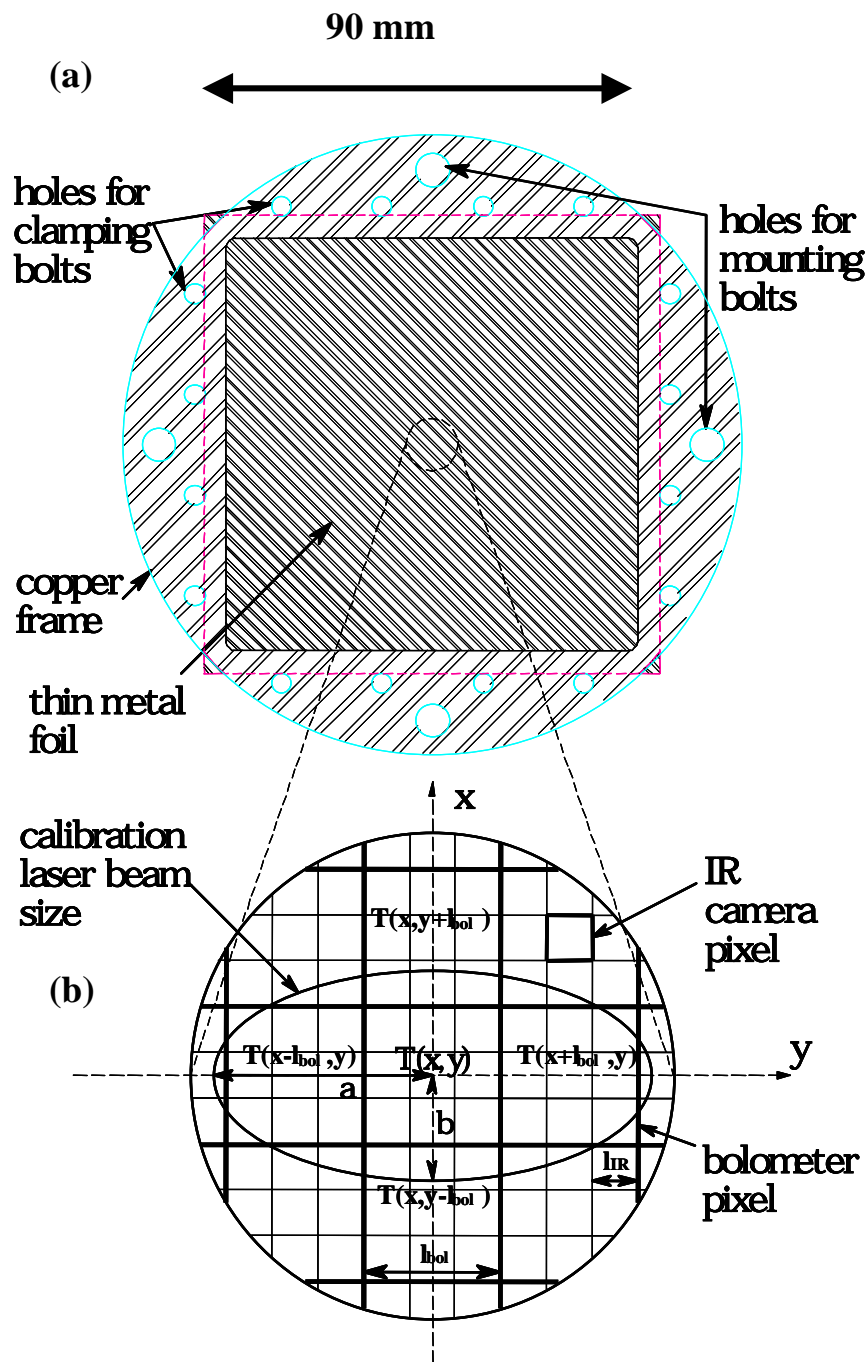
Fig. 1.4.4.2 (a)CAD drawing of the IRVB mask frame and (b) the concept of the spatial channels for the analysis algorithm [14].

2   Development

The IR bolometer consists of the IR camera, the bolometer tube with the mask and the vacuum window. Inside the vacuum vessel, the bolometer tube (that has a aperture plate at the tip of the tube and a mask is set inside the tube) is installed. The plasma radiation comes through the aperture to the foil, the temperature of the detected area on the foil rises about a few degrees above room temperature. The IR camera measures this temperature rise through the vacuum window. The IR camera does not need to exist in vacuum due to the IR vacuum window that separates it from the vacuum. The CAD of the installed configuration of the IR bolometer on the upper port in LHD is shown in Fig. 2.1.

2.1   Design of IR bolometer pipe

For an estimation of plasma radiation power, the absorbed power at the metal foil depends on each parameter of the IR bolometer, the distance from the foil to the last closed magnetic surface (LCMS), the size and position of the bolometer camera aperture, the foil materials, the area of the spatial channel and the thickness of the foil.

The design of the bolometer pipe for the SIB mask on the upper port in the 3rd campaign (1999-2000) is shown in this section as one example. From the distance from the foil to the midplane of the plasma, the solid angle of the foil, Ω_f, assuming that the aperture size is larger than the pixel area is estimated as follows,

$$\Omega_f = A_f \left(1/l_{fa}\right)^2$$

where A_f is the pixel area of the SIB mask and l_{fa} is the distance from the foil to the midplane of the plasma. The absorbed radiation power at the foil is estimated as follows,

$$P_f = \frac{2r_a \cdot \Omega_f}{r_{es} \cdot 4\pi} r_{es}^{3} S_{vp}$$

where r_a is the minor radius at the LCMS, r_{es} is the spatial resolution at the midplane, and S_{vp} is the

plasma radiation power density. S_{vp} was estimated as the total radiated power normalized by the plasma volume,

$$S_{vp} = \frac{P_{rad}}{V_p}$$

where P_{rad} is the total radiation power and V_p is the plasma volume.

Using P_f, the temperature rise, $\varDelta T$, on the pixel was estimated as shown in Eq. (1.4.3.1). From these equations, the position of the metal foil, which depends on the length of the IR bolometer pipe and the design of the mask frame and the foil materials were determined.

Finally, for the plasma radiation power of 1 MW, the plasma volume of 2.8 x 10^7 cm^3, the minimum detected temperature of the IR camera, delT, of 0.08 K with the aluminum foil of 0.8 μm thickness and the diameter of the pixel of 10.5 mm, the temperature rise, $\varDelta T$ was calculated to be about 6.5 K.
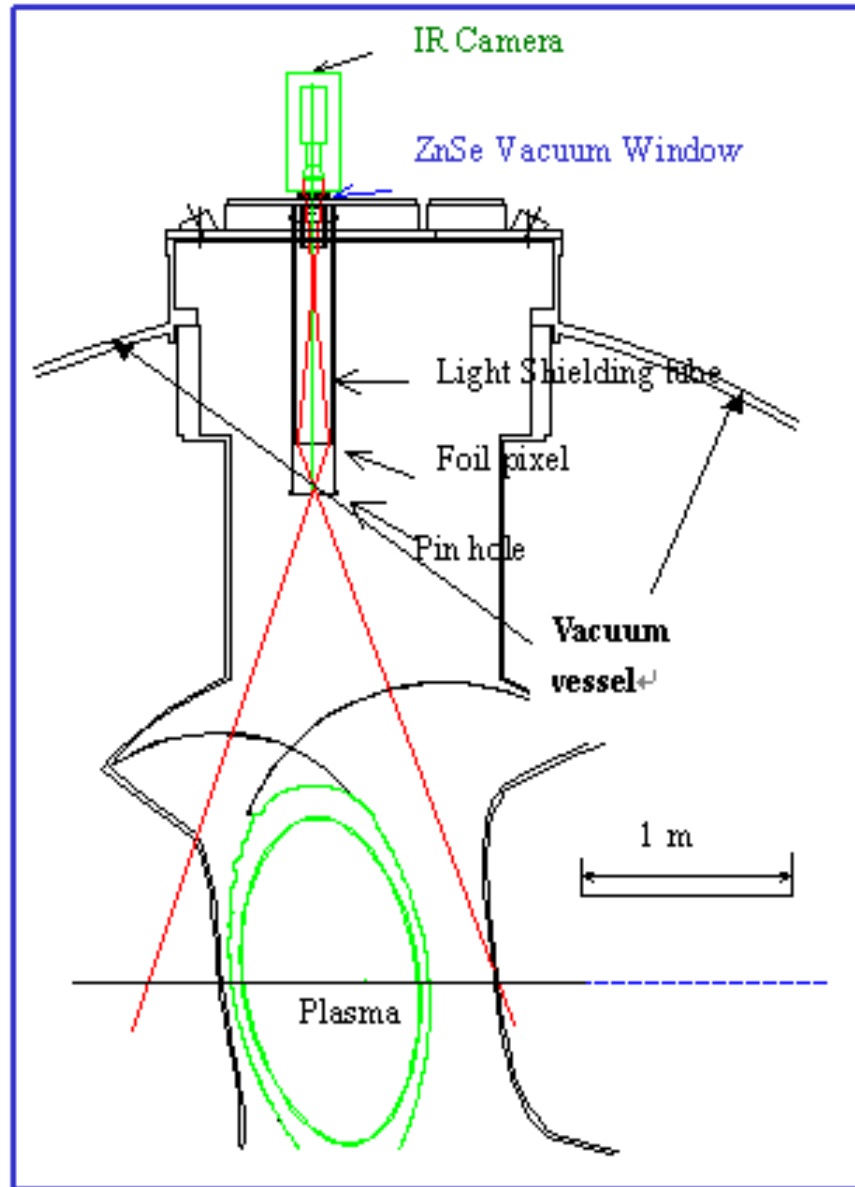
Fig. 2.1 Installed configuration of the IR bolometer on the upper port in LHD.

2.2   Mask

Two different mask types, the SIB and the IRVB, were used in the IR bolometer system as shown in Sec. 1.4. In Sec. 2.2, the actual details of each mask installed on LHD are shown. Table 2.2.1 shows the details of each mask of the IR bolometer systems on the LHD.

In 1999 for the 3rd LHD campaign, the SIB system was installed on the upper port and the IRVB system was installed at the tangential port on the LHD. But only one IR camera, the THV900LW, was used at this time. The first operation of the IR bolometer for the LHD plasma was made by the SIB system [21], and sufficient signals were measured by the IR camera. After these experiments, the THV900LW was moved to the tangential port and the IRVB system was also used [15].

After the 3rd campaign, the SIB mask was redesigned to avoid the cross-talk and the new design of the SIB mask had 114 pixels with a pixel diameter of 10 mm. This mask was made of four gold foils with dimensions of 10 cm x 10 cm in order to make a large mask with a diameter of 200 mm. The detected area on the mask frame was separated into four foils as shown in Sec. 3.1.

In addition, a new IRVB mask was made for the upper port with an area facing the plasma of 90 mm x 90 mm. Two new IR cameras, the TVS-620 and the SC500 were tested and installed before the LHD 4th campaign (2000-2001). Basically the masks during the 4th campaign and the 5th campaign (2001-2002) were the same. The number of the spatial channel of the IRVB systems is one exception, because the spatial channels of the IRVB system are determined by the analysis after the experiments.

During the LHD 5th campaign, the number of the IR camera pixels for one bolometer pixel of the IRVB systems was less than the 4th campaign's to get higher spatial resolution. The data of the IRVB on the upper port in the 4th campaign was not analyzed due to insufficient images, the number of spatial channels was not shown.

Table 2.2.1 Details of each mask of the IR bolometer systems on LHD

	3rd campaign		4th and 5th campaign		
	SIB	IRVB	IRVB	IRVB	SIB
Port	upper	tangential	upper	tangential	lower
Material	Aluminum	Gold	Gold	Gold	Gold x 4
Thickness	0.8 μm	1 μm	1 μm	1 μm	1 μm
Pixel number	118	---	---	---	114
Pixel diameter	10.5 mm	---	---	---	10 mm
Faced foil size	---	66 mm x 90 mm	90 mm x 90 mm	66 mm x 90 mm	---
spatial channel	---	10 x 14	---	10 x 14 (4th)	---
			10 x 10 (5th)	12 x 17 (5th)	---
IR camera	THV900LW	THV900LW	SC500	TVS-620	
				/THV900LW	
Slit size	24 mm x 20 mm	φ 10 mm	24 mm x 20 mm	8 mm x 8 mm	16 mm x 16 mm

Note; In the 3rd campaign, only one IR camera was used and sometimes installed at a different port. In the 4th campaign, the TVS-620 was tested at the tangential port due to repair of the THV900LW, but mainly the THV900LW was used.

2.3 Field of view and spatial channels

In this thesis, the IR bolometer systems on the upper port and the tangential port were used. In this section, each field of view (FOV) is shown. As one example, the FOV of the poloidal cross-section from the upper port at the center of the IR bolometer port is shown in Fig. 2.3.1(a). Figure 2.3.1(b) shows the measured region at the midplane of the LHD plasma as the light blue line with the color image from the IR bolometer and the center of the port is at the nearly vertically elongated plasma and the center of the FOV in this case. This FOV was determined to observe a sufficient plasma region including the ergodic region but the LHD plasma rotated as a three-dimensional plasma and the edge of the FOV cannot fully see the plasma.

Figure 2.3.2(a) shows the FOV of the vertical cross-section from the tangential port and (b) shows the FOV at the midplane. The vertical cross-section in Fig. 2.3.2(a) is located on the solid green line in Fig. 2.3.2(b) that is near the center of the FOV and marked on the data of the IRVB.

In Fig. 2.3.2(a), the FOV from the upper port is also shown as a green line that is located just at the same cross-section as in Fig. 2.3.1(a)

The FOV from the tangential port goes through a long distance in the plasma and the images from the IR bolometer and the CCD camera are shown as twisted, complicated structures.

In addition, the CAD at the midplane on the LHD is shown in Fig. 2.3.3. The FOVs of the different three bolometers are shown as each line of a yellow (resistive bolometer), a red (IR bolometer), and a green (AXUV diode). The blue line shows the last closed magnetic surface and a light red line shows the ergodic surface and a light blue line shows the vacuum vessel.

(a)

Upper port

Center of LHD

112 cm

Plasma

Last closed magnetic surface

(b)

6 5U

LHD center

6T

11 x 11 ch
IRVB data
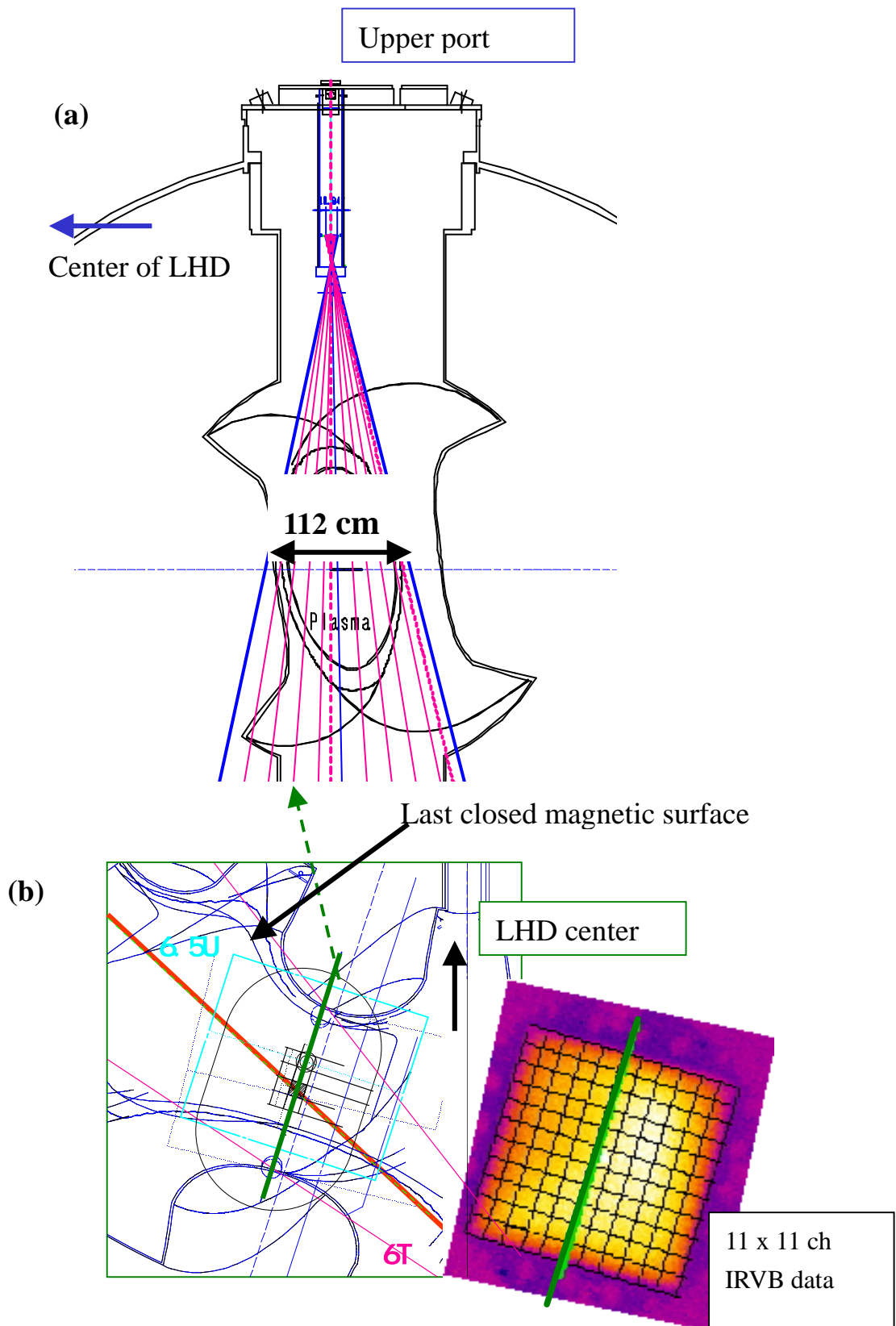
Fig. 2.3.1(a) The FOV of the poloidal cross-section from the upper port by the IRVB system in 2000 on the green line in (b). (b) the FOV is shown inside the blue line at the midplane and the red line shows the tangential view of the IRVB.

26

(a)

Upper port

Tangential port

1 m

vacuum
Vessel

（内寄配位，Rax＝3.6m，β＝0.22%）

(b)

16 x 14ch IRVB data

Midplane in LHD

6 5U

6T
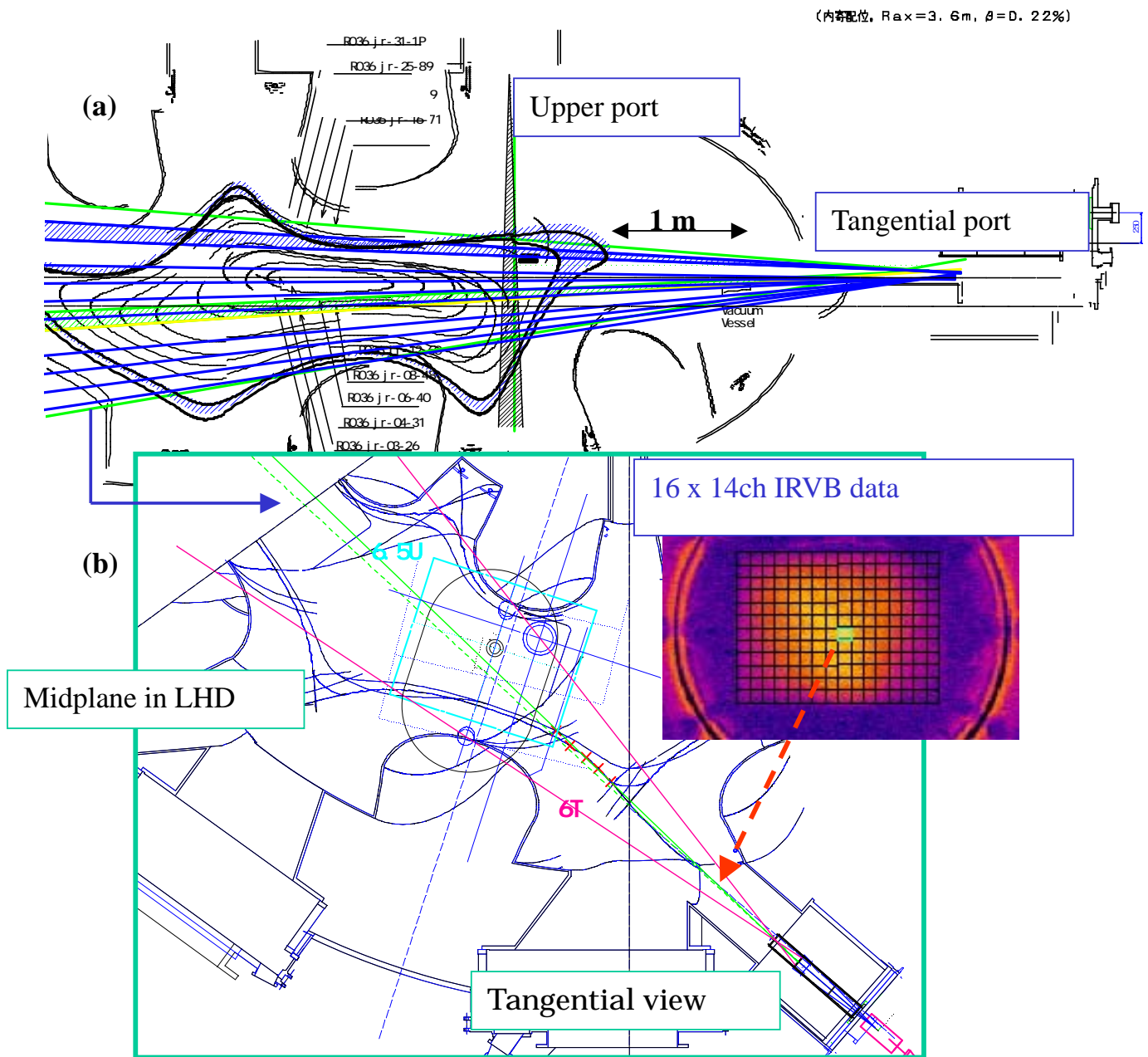
Tangential view

Fig. 2.3.2 (a)The FOV of the radial cross-section from the tangential port by the IRVB system in 2000. (b) the FOV at the midplane is shown inside the red lines and the IRVB data is shown.

Resistive Metal Film Bolometer Arrays

AXUV Diode Arrays

IR Imaging Bolometer Arrays

North

Vacuum
Vessel

8-O

7-O

5-O

LCMS

6T

1-O 1-T 2-O 10-O 10-T 9-O 3-O 4-O 7-T 6-O
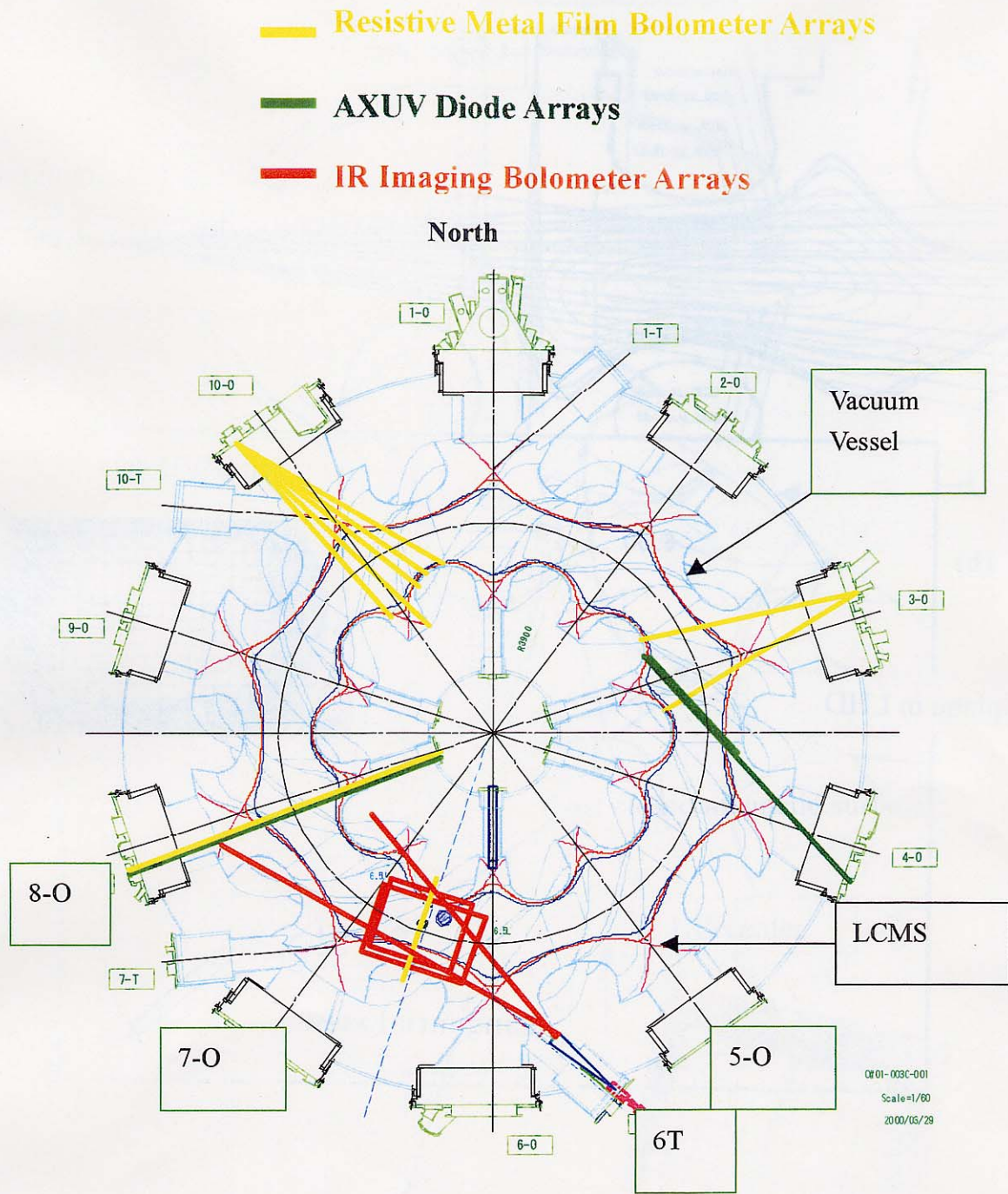
Fig. 2.3.3 CAD image at the midplane on the LHD. The FOVs of three different types of bolometers are shown as each line of a yellow (resistive bolometer), a red (IR bolometer) and a green (AXUV). The blue line shows the last closed magnetic surface(LCMS) and a light red line shows the ergodic surface and a light blue line shows the vacuum vessel.

28

2.4   Infrared(IR) Camera

The IR camera is a main part of the IR bolometer system. Three different IR cameras were tested for the IR bolometer system on LHD. In Sec. 2.4, the details of each IR camera and the working environment of the IR camera are shown.

2.4.1   Outline of each IR camera system

2.4.1.1   Agema THV900LW

The first one is the Agema Thermovision 900LW. The detected wavelengths of this camera are about 8 – 12 μm and the temperature range is from -30 degree to 1500 degree. This temperature range is separated into four regions and at present the region about -30 degree to 80 degree is used for good sensitivity. The minimum sensitivity is 0.08 degree at 30 degree (room temperature) and a total pixel number is 272 (horizontal) x 136 (vertical) at 15 Hz. During plasma experiments on the LHD, temperature noise fluctuations are large since this camera is very sensitive to the strong magnetic fields in LHD. The field of view of the lens is 5 degree x 10 degree with the minimum focus distance of 1 m, which size is very useful for the IR bolometer system on LHD. The detector is the Mercury Cadmium Telluride (MCT) type that needs a Stirling cycle cooler [21]. Table 2.4.1 shows the parameters of each IR camera.

The THV900LW can change the scanning area of the total pixels depending on the frequency. The case with 272 (horizontal) x 68 (vertical) is scanned at 30 Hz and the other case with 272 x 1 (that means only one line is scanned) is scanned at 2.5 kHz. For the plasma experiments, only the total pixel case, 272 x 136 has been used except for the calibration experiments, which sometimes used the 2.5 kHz mode.

This camera is controlled by a special control system and the data format is also analyzed as the special Agema type data.

2.4.1.2   Avio TVS-620

The second one is the Avio TVS-620 that is made by a different company. The detected wavelengths of this camera are about 8 – 14 µm and the temperature range is from -20 degree to 300 degree. The minimum sensitivity is 0.1 degree at 30 degree as the room temperature and a total pixel number is 320 (horizontal) x 236 (vertical) at 30Hz. The field of view of the lens is 9.8 degree x 12.9 degree with the minimum focus distance of 1 m, and the detector is the staring array type with 2-dimensional pixels which doesn't need a forced cooling system.

This camera is basically the handy type but in this system the camera is controlled by a PC with an exclusive software.

The TVS-620 is very sensitive to the surrounding environmental temperature. The actual sensitivity was about 0.2 degree at room temperature without magnetic fields. In addition, to check the variation of the temperatures each time by a PC was difficult because this software shows only black and white images and this image was of bad quality.

In this thesis, the data of the TVS-620 were not used.

2.4.1.3   FLIR SC500

The third one is the FLIR SC500 whose company and Agema are the same due to the merger of companies. The detected wavelengths of this camera is about 7.5 - 13 µm and the temperature range is from -20 degree to 1200 degree, but during plasma experiments only the region from –20 degree to 120 degree is used for good sensitivity. The minimum sensitivity is 0.1 degree at 30 degree and the total pixel number is 320 (horizontal) x 240 (vertical) at 60 Hz. The field of view of the lens is 8 degree x 12 degree with the minimum focus distance of 2 m, and the detector is the staring array type with 2-dimentional pixels which doesn't need a forced cooling system.

This camera is controlled by a general PC using special software and the binary type files can be obtained directly.

2.4.1.4　The latest model

The latest model of the IR camera is also shown in Table 2.4.1. The detected wavelengths of this camera are about 3.5 - 5 μm. The minimum sensitivity is 0.02 degree at 30 degree and a total pixel number is 320 (horizontal) x 240 (vertical) at 420 Hz. The detector is the staring array type with two-dimensional pixels and this IR camera need the Stirling cycle cooling system. In addition, the scanning region of total pixels can be changed as 128 (horizontal) x 8 (vertical) at 13 kHz. The improvement of the sampling frequency, the minimum sensitivity and the number of pixels of the IR camera is a developing technology that is changing for the better every year.

2.4.1.5　Control system

Figures 2.4.2 – 2.4.4 show the control systems of each IR camera. During the plasma experiments, the IR cameras were remotely controlled from outside the LHD room. The differences of each IR camera are cables and the controllers.

Figure 2.4.2 shows the control system of the THV900LW. The THV900LW was installed in the neighborhood of the LHD vacuum vessel but this controller was set outside the LHD room, because of restricted access to the LHD room during plasma experiments. The data and the signals are sent by the three optical cables ant these cables are connected to the special cable of the THV900LW with the optical fiber relay units. An operator controls the IR camera from the diagnostics device room at present.

Figure 2.4.3 shows the control system of the TVS-620. The cable from the PC to the IR camera uses the IEEE 1394 cable with the optical repeater and plastic optical fibers, because the IEEE 1394 can not be used over a long distance.

Figure 2.4.4 shows the control system of the SC500. This camera has to use the special cable from the FLIR company and this cable is connected to the connection box with the RS-232C and the

RS-422 cables. These RS type cables are connected to the PC. In the future, an optical cable will be used from the connection box to the PC with RS type cables because this operation at the present length of about 15 m is not guaranteed.

The PCs of two systems are removed from the coils of LHD due to the necessity for installation at low magnetic field.

Table 2.4.1 Details of each IR camera on LHD and the latest model

	Agema THV900	Avio TVS-620	FLIR 500 A	Latest model (tested at B = 0.6 T)
Temperature	- 30　1500	- 20　300	- 20　1200	?
Wavelength	8 - 12 μm	8 - 14 μm	7.5 - 13 μm	3.5 - 5 μm
Sensitivity	0.08　30	0.1　30	0.1　30	0.02
detector type	scanning	staring array	staring array	staring array
cooling style	Stirling cycle cooling	no-cooled	no-cooled	Stirling cycle cooling
Lens FOV	10°　5°	12.9°　9.8°	12°　8°	
Pixel number	272　136	320　236	320　240	320　240
Frequency	15Hz　(272x136　30Hz　272x68　2.5kHz　(272x1	30Hz	60Hz	420Hz　(320 240 .... 13 Hz　(128x8
Used on IR bolometers				
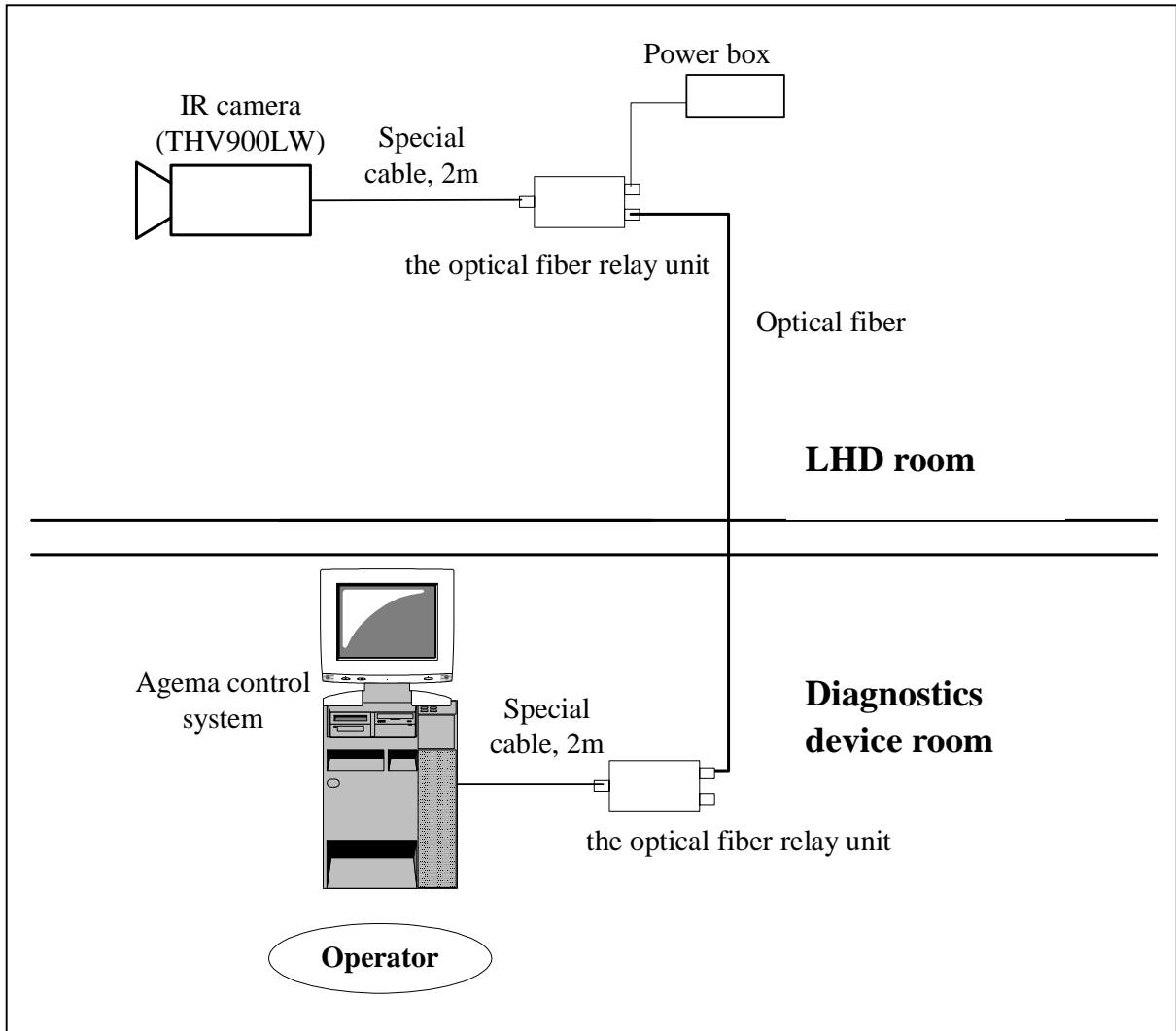
Fig. 2.4.2 The control system of the THV900LW. The IR camera is installed on LHD and controlled by the Agema control system from outside the LHD room. The data and signals are send by three optical cables and these cables are connected to the special cables. The power cables are connected to the power box and the control system.
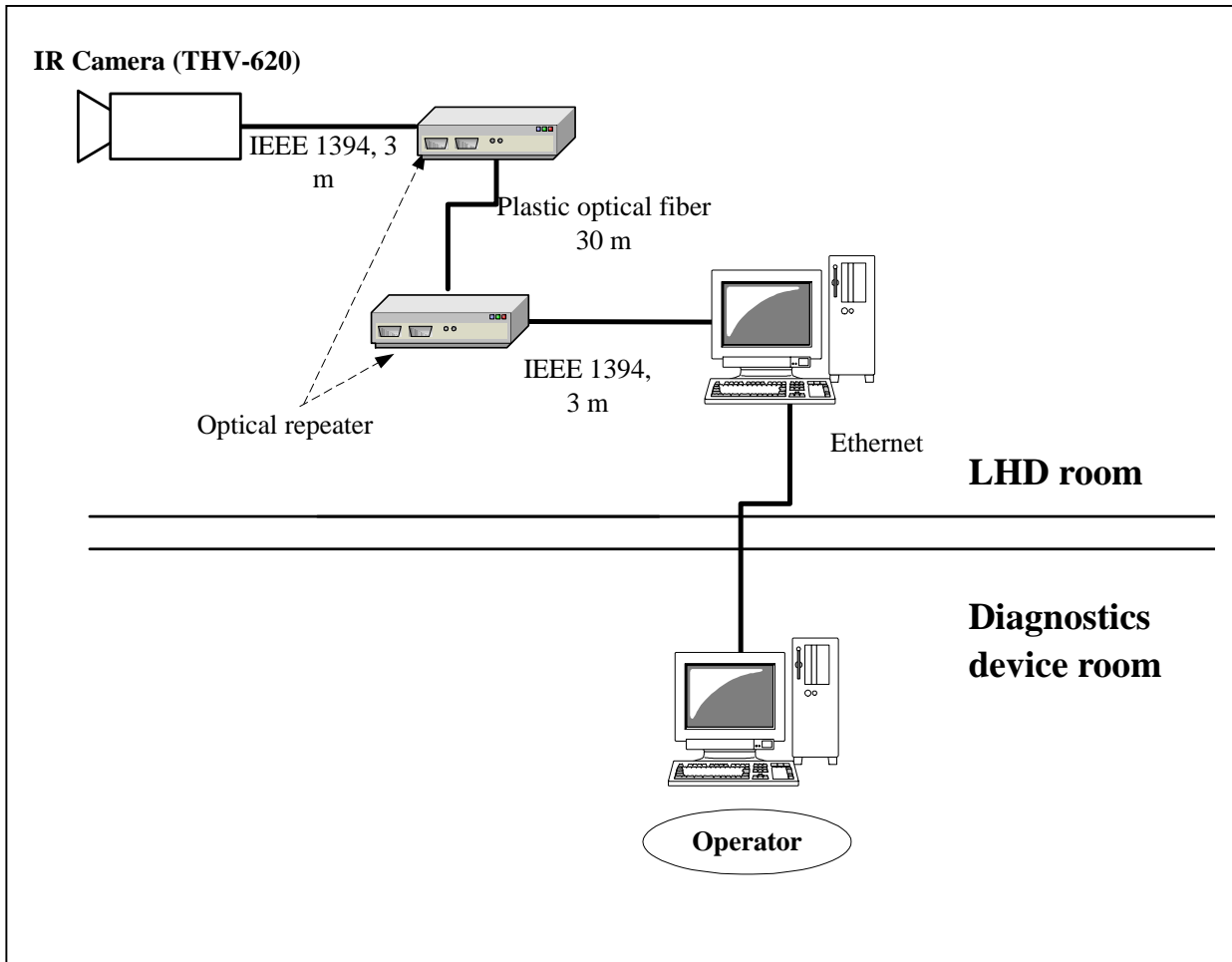
Fig. 2.4.3 The control system of the TVS-620. The IR camera is installed on LHD and controlled with a general PC using special software from outside the LHD room. The data and signals are sent by the IEEE 1394 cables and the optical cable with the optical repeater.

IR camera
(SC500)

Special
cable, 3m

Power box

Connection box

Extention spetial cable,17m

RS-232C 15 m
RS-422   15 m

Ethernet   **LHD room**

**Diagnostics
device room**

Operator
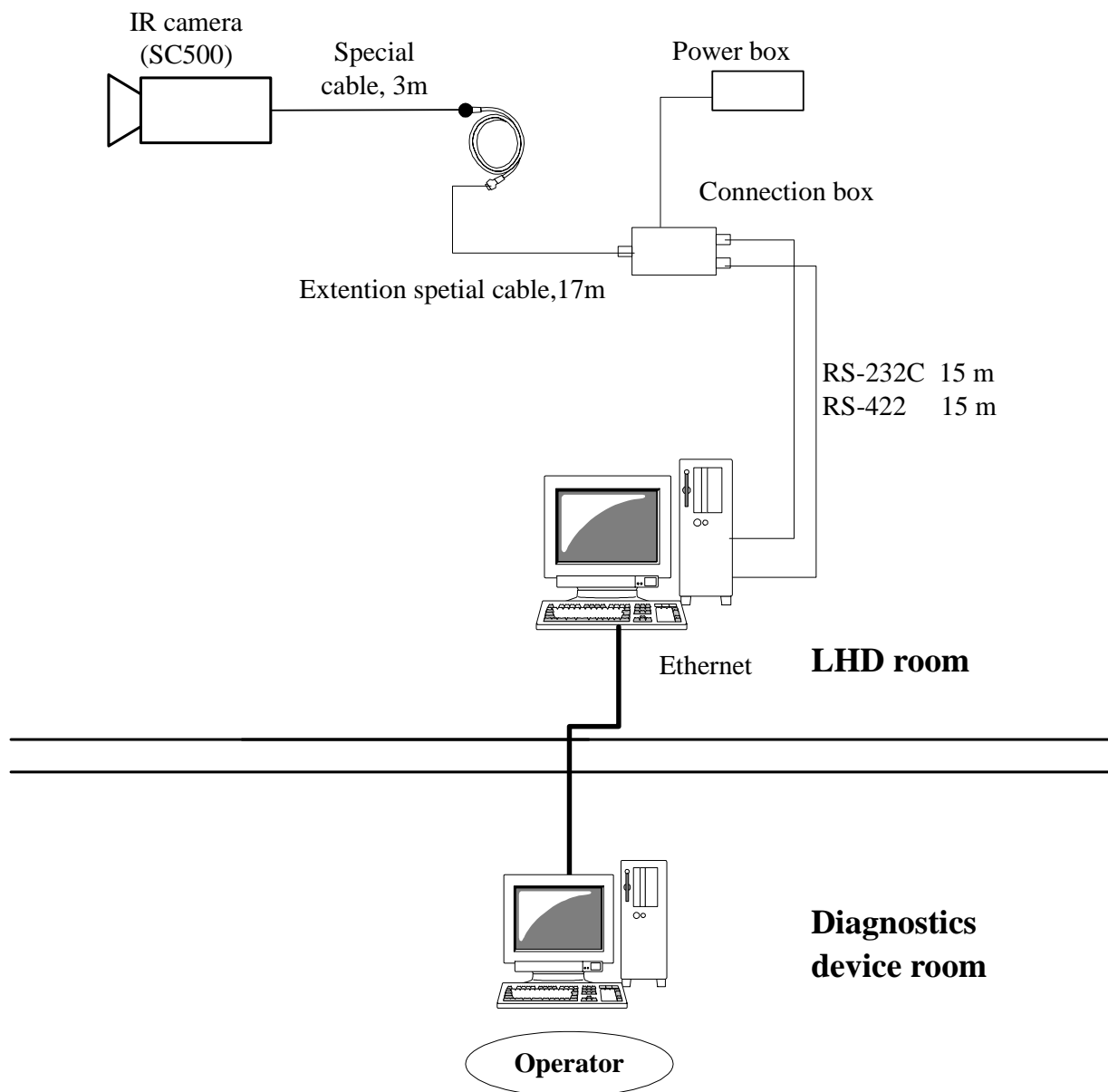
**Fig. 2.4.4 The control system of the SC500. The IR camera is installed on LHD and controlled with a general PC using special software from outside the LHD room. The data and signals are sent by the special cables and the RS-232C and RS-422 cables.**

2.4.2 Detected wavelength by IR camera

The wavelength region of plasma radiation varies widely from the x-ray to the infrared. But in the IR bolometer system, the minimum and the maximum limits of the detected wavelength depend on the materials of the foil in the mask. For the 1 μm thick gold foil, the minimum limit is about 0.25 nm and the maximum limit is about 600 nm. In this region, the plasma radiation can be absorbed on the foil and this absorbed power is changed into the thermal radiation.

The spectral emissive power of blackbody radiation as the Planck distribution [22] is

$$E(\lambda,T) = \frac{C_1}{\lambda^5 [\exp(C_2/\lambda T)-1]} \qquad (2.4.2.1)$$

where the first and second constants are $C_1=2\pi hc_0^2 = 3.742 \times 10^8$ (W μm^2 / m^2) and $C_2 = (hc_0/k) =$ 1.439 x 10^4 (μm K) with Boltzmann constant, $k = 1.3805 \times 10^{-23}$ J/K. Figure 2.4.2.1 shows the Planck distribution with 500 K and 300 K. From Fig. 2.4.2.1 the blackbody radiation about the room temperature of 300 K peaks at 10 μm, so the long-wave IR camera type of the IR bolometer system is better, because the IR camera measures around room temperature.

The IR camera can not measure the radiation from the plasma directly as the view is obstructed by the bolometer pipe and the mask. The changing of the temperature on the vacuum vessel on LHD is very slow during one day, and during the discharge this temperature does not change. The temperatures of the bolometer pipe and the mask frame are also same as the temperature of the vacuum vessel due to thermal connection by the bolts. The blackbody radiation effect from the other regions (for example, the bolometer pipe) to the foil of the mask was negligible due to the same temperature as mentioned above.

The vacuum window is a ZnSe window with special coating for a high transmission of penetrated wavelengths about 3 – 13 μm with a transmission of over 90 %. The detected wavelength of the IR bolometer depends on each IR camera, and this region about 8 – 12 μm. At present, the losses of the other IR regions were not estimated for the data of the IR bolometer. Figure 2.4.2.2 shows the relationship of each wavelength region of the IR bolometer system.

37
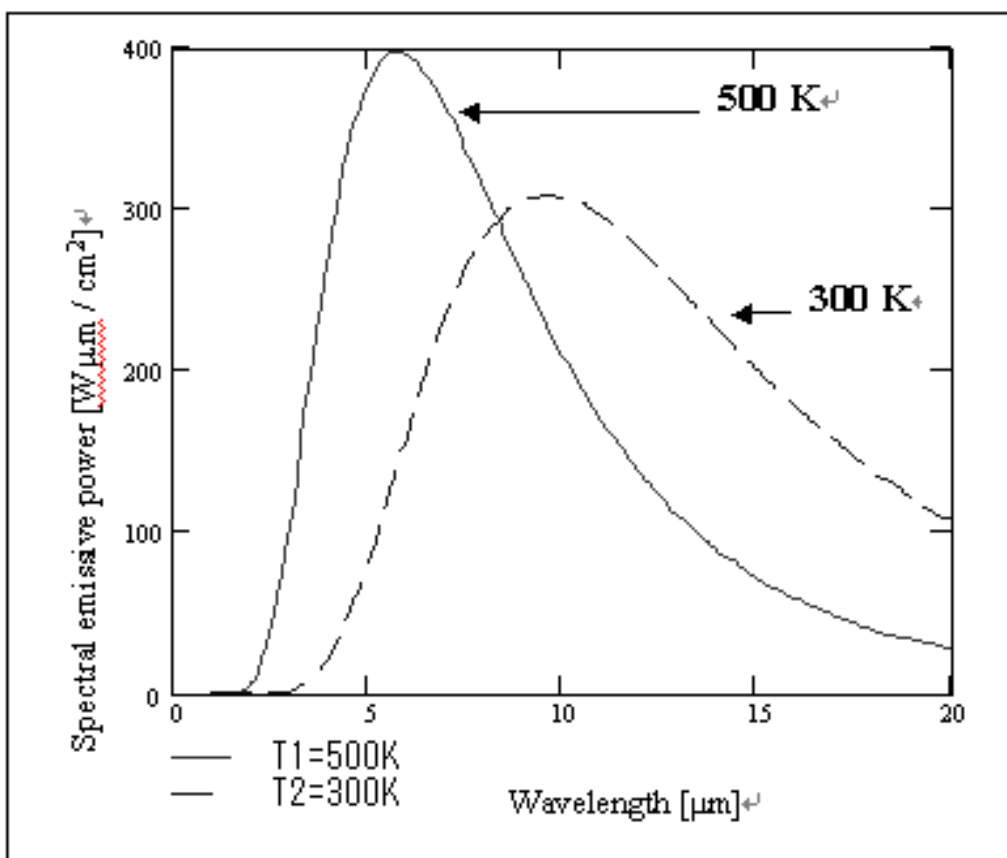
Fig. 2.4.2.1 The spectral emissive power of a blackbody with
Eq. (2.4.2.1).   For T2, this emissive power times 10.

Infrared Radiation

Thermal Radiation

Plasma Radiation

Temperature rise

Pinhole plate

Infrared Camera

Plasma

Infrared vacuum
window ZnSe)

Metal foil (gold, aluminum et.al) and mask

Inside vacuum vessel
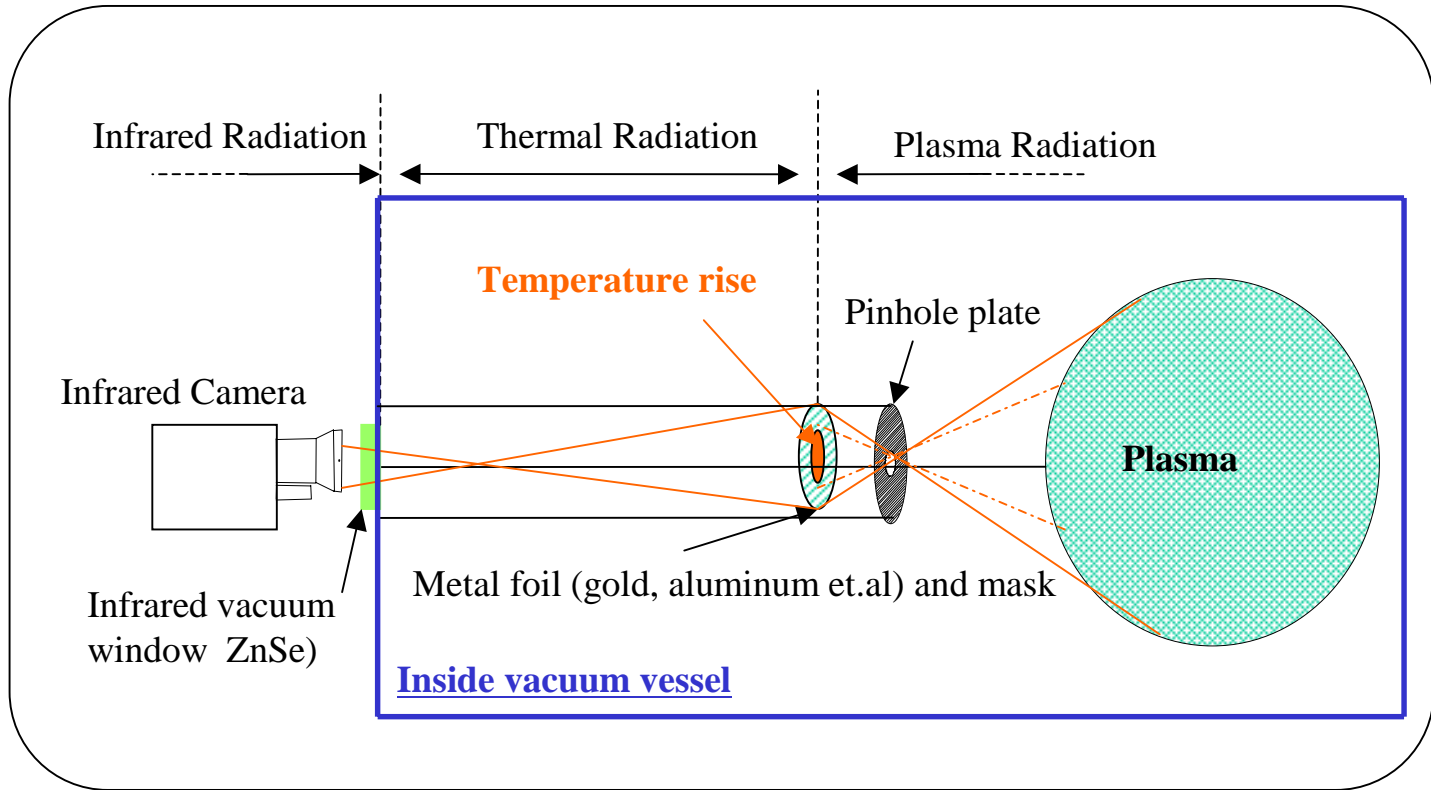
Fig. 2.4.2.2 Relationship of each wavelength region of the IR bolometer system. Due to the bolometer tube and the mask, the IR camera can not see the plasma directly and this camera does not measure the infrared radiation from the plasma.

2.4.3 Magnetic shielding

The essentially steady magnetic fields by the superconducting coils on LHD are a big problem for the IR camera because basically the IR camera is weak to the magnetic field. Each IR camera was tested by another magnetic source. Before this magnetic field test, only the THV900LW was tested under 300G [23] but this value was not sufficient for the installation of the IR bolometer. In this section, some steps for each camera are shown.

2.4.3.1 Agema THV900LW test

Initially, the position of installation for the THV900LW was designed for the upper port. The THV900LW IR camera has several components which might be susceptible to magnetic fields due to having four electric motors at a minimum. These are a cooling motor, a lens focus motor, and two motors for the X and Y scanning mirrors. The stray magnetic field at the designed position was estimated at about 1.0 T with the magnetic field at the magnetic axis about 3.0 T on the LHD. Using a linear magnetic coil system in NIFS with a maximum magnetic field of about 0.6 T, the THV900LW was tested without the shielding box. In addition, the effect of the direction of the magnetic field lines was observed. From these test, it was observed that the motors of the THV900LW were weak to the large magnetic gradient since the perturbation of the measured temperature relative to the direction of the magnetic field was confirmed.

Due to the limited space around the linear magnetic coil system, the effect of the magnetic shielding for the IR camera was tested during the test of the superconducting coils on LHD. The THV900LW was installed to fix the direction relative to the strong magnetic field line at the upper port. The magnetic shielding box was made of the soft iron plate with a thickness of 6 mm. The magnetic field was changing 0.1 T per minute as the magnetic field at the magnetic axis on the LHD. At first, the motor of the focus lens was not controlled and the cooling motor also did not move, finally the complete control system did not work. The magnetic field was estimated to be about 2.0

T at the magnetic axis at the timing of the trouble.

From this result, to minimize the magnetic field for operating of the IR camera, the position of the IR camera was shifted up to give a magnetic field of about 0.4 T and is was determined that the IR camera has to be covered with a shielding box during the magnetic field on LHD.

The value of about 0.4 T was smaller than the result of the linear magnetic coil system. The reason for this was estimated to be that the effect of opening of the shielding plate was too large due to the diameter of the neck of the lens. For the cooling inside the shielding box, a fan was setting at the backside. The extra boxes including the power source and the optical fiber relay unit (components of the camera) were also installed at the lower magnetic field area of about 0.1 T.

The conditions to use the THV900LW on LHD during the plasma experiments were estimated as follows,

(1) IR camera was shielded by an iron box with a thickness of $t = 6$ mm,

(2) The highest magnetic field outside the iron box is under 400 G, as determined by calculations and field measurements,

(3) The optical fiber relay unit (component of the camera) was also installed at a low magnetic field area.

Figure 2.4.3.1 shows the drawing of the shielding box for the THV900LW with a thickness of $t = 6$ mm.

2.4.3.2 Avio TVS-620 test

For the second case, the other company's IR camera, TVS-620 was tested in the magnetic field. For the magnetic field, this type is better than the THV900LW due to no-cooling and no-motors. Basically, the main system of the IR camera was strong but the power box was weak due to the low capacity of the DC/DC converter. This converter was damaged at about 0.5 T. From this experience, a shielding box for the power box was made.

2.4.3.3 FLIR SC500 test

For the third case, the SC500 was tested during the magnetic field with the soft iron shielding box on LHD. This type was also strong to the magnetic field due to the same reason with the TVS-620. For both case, the THV900LW and the TVS-620, the poison at the upper port was determined to have a magnetic field of about 0.6 T and the extra boxes including the power source and the optical fiber relay unit (component of the camera) were installed at about 0.3 T. But the DC/DC converter was damaged. From this result, the positions of the extra boxes were determined which had a magnetic field of under 0.1 T. The main system of the IR camera basically doesn't have any large problems. But for the case during the local island diverter (LID) magnetic field and in the case of the shifted magnetic axis to the inboard side, about 3.5 - 3.57 m, the observed temperature by the IR camera has perturbations on the signals.

At present, the SC500 is working with the soft iron magnetic shielding box with a thickness of t = 6 mm and the extra boxes are not used.

2.4.3.4 Personal computer(PC)s

For the PCs of the TVS-620 and the SC500 as shown in Figs. 2.4.3 and 2.4.4, the magnetic fields at the installed positions were calculated. From the experience of troubles for hard disks by other groups, the maximum magnetic field for using the PC of the IR bolometer system was estimated to be about 0.1 T.
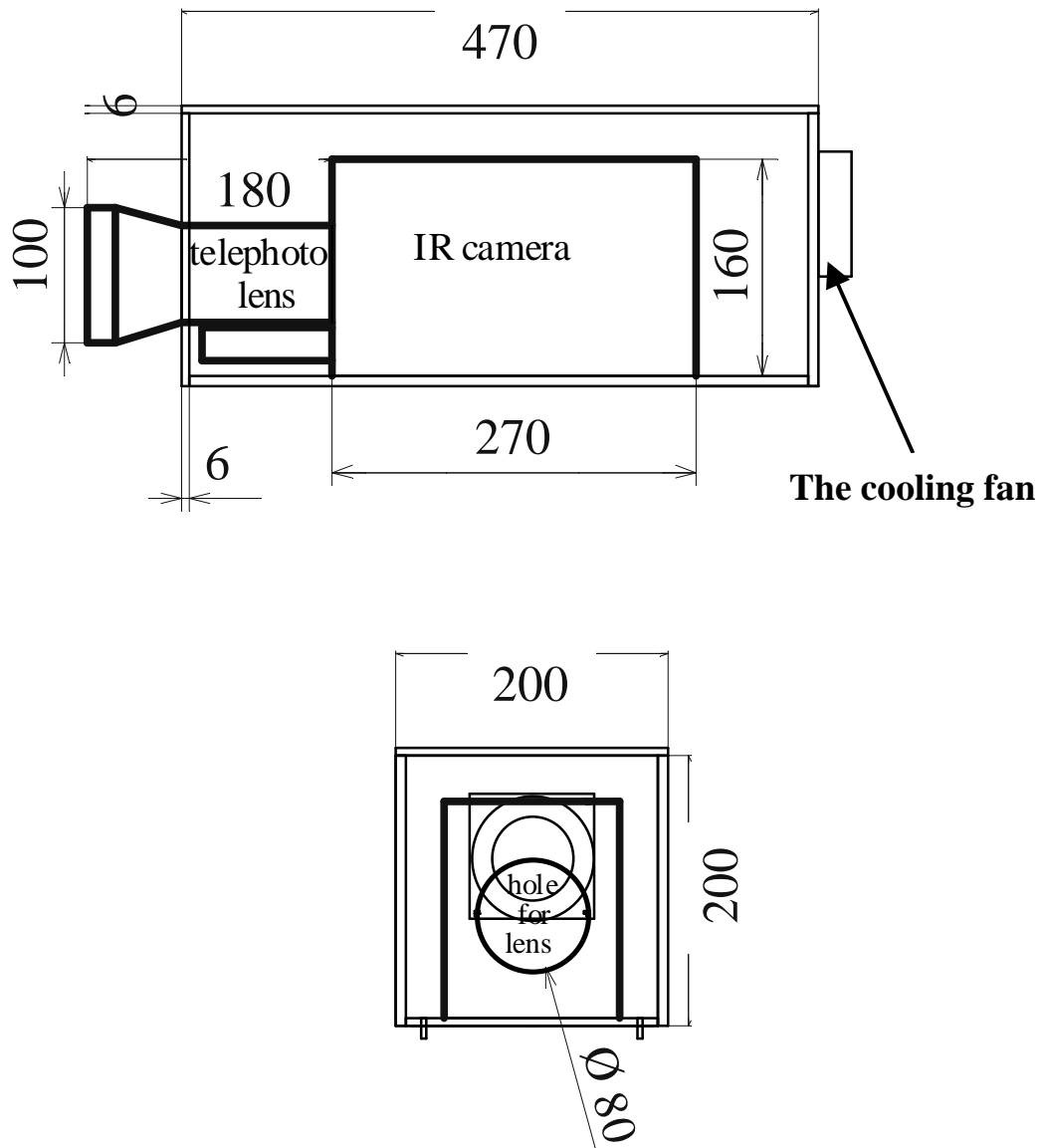
Fig. 2.4.3.1 The magnetic shielding box of the THV900LW with a thickness of t = 6 mm. This size is about 200 mm x 200 mm x 470 mm. The cooling fan is set at the backside of the box.

3 Details of IR bolometer system

3.1 Calibration method

For the thermal diffusion equation as in Eq. (1.4.1.1), the area of pixel is multiplied as shown in Eq. (3.1.1)

$$A_{pix}\left(\frac{\partial^2 T}{\partial x^2} + \frac{\partial^2 T}{\partial y^2}\right) = \frac{A_{pix}}{\kappa} \cdot \frac{\partial T}{\partial t} - \frac{P_{rad}}{k \cdot t_f} + \frac{A_{pix} \cdot \varepsilon \sigma_{SB}\left(T^4 - T_0^{\,4}\right)}{k \cdot t_f} \qquad (3.1.1).$$

Where A_{pix} is an area of bolometer pixel, κ is a thermal diffusivity, k is a thermal conductivity, t_f is a thickness of a foil, P_{rad} is a incident radiation power, ε is the blackbody thermal emissivity, σ_{SB} is the Stefan- Boltzmann constant, σ_{SB} = 5.6697 x 10^{-12} [W/(cm^{2}K^4)]. Solving for the incident radiation power, P_{rad} of Eq. (3.1.1), is shown as follows,

$$P_{rad} = k \cdot t_f \frac{A_{pix}}{\kappa} \frac{\partial T}{\partial t} - k \cdot t_f \cdot A_{pix}\left(\frac{\partial^2 T}{\partial x^2} - \frac{\partial^2 T}{\partial y^2}\right) + k \cdot t_f \cdot A_{pix}\varepsilon \sigma_{SB}\left(T^4 - T_0^{\,4}\right) \qquad (3.1.2)$$

In this equation, the parameters, κ, k, and ε depend on the materials, but the emissivity, ε is estimated as a constant equal to unity due to the blackening effect. The actual other parameters of a foil depend on the foil condition, and are not uniform on a foil. This is due to (1) variation in thickness due to manufacturing, (2) the effect of uneven deposition of carbon on the foil, (3) the wrinkles on the foil.

For the actual κ and k of each spatial channel on a foil, the calibration parameters were determined as the calibration coefficient K = 1/(k t_f) [K/mW] and the cooling decay time $\tau = A_{pix}/\kappa$ [s] that have been used for the other bolometer types [16, 24, 25]. For these reasons, K and τ are measured for each spatial channel by the calibration experiment.

For the measured temperature on one IR bolometer pixel using the IR camera, ΔT, if an effective temperature distribution including the blackbody radiation effect on the area of the bolometer pixel is defined as follows,

$$\Delta T = A_{pix}\left\{\varepsilon \sigma_{SB}(T^4 - T_0^{\,4}) - \left(\frac{\partial^2 T}{\partial x^2} + \frac{\partial^2 T}{\partial y^2}\right)\right\} \qquad (3.1.3).$$

where T_0 is the mask temperature estimated as room temperature and T is the rise temperature by a heat source (plasma radiation or calibration heat source). On the right hand in Eq. (3.1.3), T is calculated at each position, x and y, but ΔT is normalized on the pixel area. Solving for the incident radiation power, P_{rad}, using Eq. (3.1.3), K, and τ, is shown as follows,

$$P_{rad} = \frac{1}{K}\left(\Delta T + \tau\frac{\partial T}{\partial t}\right) \tag{3.1.4}$$

This is a common equation for both IR bolometer systems and also other bolometers [15, 21].

3.1.1   Calibration method of the SIB

For the SIB mask, K and τ of each pixel were determined by the calibration experiment. A He-Ne laser ($\lambda = 632.8$ nm) as a heat source is used for this calibration whose power is about 10 mW. Using small relay mirrors, the laser light was scanned for each pixel to heat the foil while being measured by the IR camera. The transmission power loss of the laser is about 5 % at each mirror. In general two or three mirrors were used, of which number depends on the position on the mask. In addition, the laser power decreased after passing through the infrared vacuum window by about 10%. Finally, the laser power arriving at the mask is about 80 % in the case using two mirrors. The effect of the laser incident angle to the IR vacuum window was small because the scanning angle of the laser is varied for only a few degrees since the mask was far from the laser light and also from the test chamber, and the angle was also kept as small as possible by changing the mirror position.

The detected power density of the plasma radiation, P_{rad}, on each pixel can then be calculated as shown in Eq. (3.1.4) [16, 24] with measured K and τ. The K is determined from the temperature rise, ΔT, divided by the incident laser power.

One example of a representative calibration experiment using the He-Ne laser is shown Fig. 3.1.1.1(a) that is the IR image using the THV900LW of the SIB mask with laser light for the pixel R5P4. In fact, this calibration experiment was done for all 118 pixels of the mask used in the 3rd

LHD campaign. Figure 3.1.1.1(b) shows the calibration data of the changing temperature on pixel R5P4 using the IR camera (THV900LW) data with line scanning at 2 kHz on the peak of the Gaussian profile of the laser. At 0.77 s, the chopper cut the laser light and the temperature was decreased to zero.

The decay time, τ, is determined by fitting the exponential decay time of the foil temperature when a chopper cuts the laser light as shown in Eq. (3.1.5),

$$\Delta T = m1 \cdot \left[1 - \exp\left(-t/_{m2} \right) \right] \quad , \quad (3.1.5).$$

Using this equation to relate t and ΔT, two parameters, $m1$ and $m2$ are solved for. The value, $m1$ shows the temperature rise and $m2$ shows the decay time.

For the pixel R5P4, the decay time is about 0.077 s as shown in Fig. 3.1.1.1(a). The decay time varies from pixel to a pixel, depending on the clamping of the mask and foil, and typically is about 0.13 s.

In the SIB mask, the pixels were referenced was called by R and P numbers as shown in Fig. 3.1.1.2. For each row, "R", the number of the position,"P" was given. For example, the pixel R5P4 was around the center of the mask.

On the pixel R5P4, $m1$ was about 4.3 deg. and the incident laser power was about 6.3 mW, so the calibration coefficient, K is about 0.68 deg./mW. A typical value of K for all pixels is about 0.80 deg./mW.

To determine K, a consideration was made of which type of ΔT is better. Figure 3.1.1.2 shows different values of ΔT, (a) is using the difference of the peak temperature of the Gaussian profile of the laser to the mask temperature and (b) is using the difference of the averaged temperature in the pixel to the mask temperature. For each of the pixels among 118 channels, a different color is marked on the mask indicating the level of K. The incident power of the He-Ne laser is deposited on an area that is smaller than the foil inside the pixel due to the beam width of the incident laser of about 1 mm which is smaller than the diameter of the pixel of about 10.5mm. Both cases have some

46

problems. For example in case (a) some pixels near the edge of the mask have too a high temperature rise (yellow pixels) and in case (b) the edge of the pixels did not detect laser power and for the present, the equation of the Gaussian profile is not included. In using each parameter for the actual plasma data, case (b) was chosen for K.

Some of the edge pixels of the SIB mask have cross-talk as shown in Fig. 3.1.1.3 which is an IR image of pixel R10P2 using the THV900LW. Cross-talk means the leakage of the signals to the neighboring pixels and these pixels are marked with a bold circle in Figs. 3.1.1.2(a) and (b). The weak tightening of the two masks with the foil is the reason for this problem and this SIB was only used in the 3rd LHD campaign. For the 4th campaign, a new SIB was designed with 114 pixels as shown in Fig. 3.1.1.4(a). To have sufficient tightening, a lot of bolts were used and this type did not show any cross-talk. One example of the IR image from the calibration experiments using the THV900LW is shown in Fig. 3.1.1.4(b).

From the calibration data, the cooling decay time of the SIB is almost the same as that for pure aluminum foil but the calibration coefficients are different from pure aluminum by a factor of 2.

At present all pixels of the SIB were calibrated using each parameter.

3.1.2　Calibration method of the IRVB

For the IRVB mask type, basically the same equation for the detected power density of the plasma radiation is used as shown in Eq. (3.1.4). The different point of the calibration parameters is that the two parameters, K and τ, are two-dimensional functions of (x, y) because each spatial channel is not separated on the foil. In Sec. 3.1.2.1, the estimated profile calibration method using data from the tangential IRVB is shown which is used at present for both the tangential and upper port IRVBs. In Sec. 3.1.2.2, the detailed pixel calibration method is shown that will be used in the future.

3.1.2.1　Estimated profile calibration of the IRVB

The spatial channels of the IRVB system were determined by the analysis because each channel is not separated on the foil by masks. For the first calibration of the IRVB, the simple method using the estimated profile of the cooling decay time on the foil was employed.

The absorbed power on a gold foil as a function of time was calculated including the time derivative term and the spatial derivative term. The thermal diffusivity was adjusted to fit the measured temperature rise by the IR camera to the incident laser power by the calorie-meter as shown in Fig. 1.3.2.1(a). The thermal conductivity was also adjusted to fit the measured cooling decay time by the IR camera. Matching the calculated power to the laser curve required the thermal diffusivity that was 0.83 times the value for pure gold ($\kappa_{AU} = 1.27$ cm^2/s) and the thermal conductivity that was 3.5 times the value for pure gold ($k_{AU} = 3.16$ W/cmK). From this result, the calibration coefficient, K, was determined to be about 0.90 [K/mW] that was assumed to be constant for all spatial channels on the foil. One notes from this figure that the time derivative term dominates initially, then gives way to the spatial derivative or diffusive term.

Using the chopped He-Ne laser, a variation in the decay time as a function of the distance from the mask frame was observed as shown in Fig. 3.1.2.1(b). By the parameter $\kappa = \kappa_{AU}/1.2$ and the observed data, this dependence to the mask frame was modeled as shown [15],

$$\kappa(x, y) = \kappa \left[\cos(\pi x/a_x) \cos(\pi y/a_y) \right]^{0.4} \qquad (3.1.6)$$

where a_x and a_y are the dimensions of the foil and x and y are the distance from the center of the foil. This result using Eq. (3.1.6) is shown in Fig. 3.1.2.1(b) with the observed data. From the Eq. (3.1.6), the cooling decay time was determined as

$$\tau(x, y) = A_{pix}/\kappa(x, y) \qquad (3.1.7)$$

for each spatial channel of the IRVB.

From these calibration data, the cooling decay time of the IRVB is almost the same factor to the pure gold foil but the calibration coefficients are different by a factor of 3.5 which is the same

tendency as with the SIB.

3.1.2.2 Detailed calibration method of the IRVB

In this section, the detailed calibration method of each spatial channel of the IRVB using the minimum spatial resolution of the IR camera is described [15].

The calibration parameters for the IRVB are measured using the heat source with as uniform a profile as possible whose power is unknown. The distribution of the foil temperature with the boundary condition and including the mask temperature using the heat production at a constant rate A_0 in the rectangle with keeping the surface temperature at $x = \pm\ a$ and $y = \pm\ b$ (the edge of the foil) is given by [26],

$$T_{rel} = \frac{A_0(a^2 - x^2)}{2k} - \frac{16A_0a^2}{k\pi^2} \cdot \sum_{n=0}^{\infty} \frac{(-1)^n \cosh[(2m+1)\cdot\pi\cdot x/2a]\cdot\cosh[(2m+1)\cdot\pi\cdot k\cdot y/2a]}{(2l+1)^2 \cosh[(2m+1)\cdot\pi\cdot k\cdot b/2a]} \quad (3.1.8).$$

Since the heat source A_0 is unknown, the ratio of the measured temperature by the calibration experiments to the temperature distribution using Eq. (3.1.8) is normalized to the center IR pixel of the foil giving the relative calibration of each bolometer pixels as follows,

$$K_{rel}(x, y) = \frac{T_{heat}(x, y)}{T_{rel}(x, y)} \quad (3.1.9)$$

Where, T_{heat} is the temperature distribution obtained by the calibration experiment, and K_{rel} is the relative calibration coefficient for each pixel (x, y).

The absolute calibration can be carried out for the IRVB mask by illuminating the center of the foil using a laser light source of a known power distribution. For instance, if a He-Ne laser of a known power, P_{laser}, with a Gaussian distribution given by

$$S_{laser}(x, y) = \frac{P_{laser}}{\pi(\alpha^2 + \beta^2)} e^{-\left(\frac{x^2}{\alpha^2} + \frac{y^2}{\beta^2}\right)} \quad (3.1.10).$$

Where S_{laser} is the observed heat flux, α and β are the width of the laser (in the case of a circular

laser power distribution, $\alpha = \beta$) and the x and y are the relative position inside the circle ($x <$ α, $y < \beta$).

The resulting temperature evolution near the center of the foil is given by

$$T_{laser}(x,y,t) = \frac{4\alpha\beta \, K(x,y)P_{laser}}{ab(\alpha^2 + \beta^2)} \sum_{m=0}^{\infty}\sum_{l=0}^{\infty} \frac{\cos\lambda_l x \cos\lambda_m y}{\lambda_{lm}^2} e^{-\left(\alpha^2\lambda_l^2 + \beta^2\lambda_m^2\right)/4}(1 - e^{-\kappa\lambda_{lm}^2 t})$$ (3.1.11)

where,

$$\lambda_l = \frac{(2l+1)\pi}{a}, \quad \lambda_m = \frac{(2m+1)\pi}{b}, \quad \lambda_{lm} = \sqrt{\lambda_l^2 + \lambda_m^2} \ , \quad \alpha,\beta << a,b$$ (3.1.12)

These *a* and *b* are the same value for Eq. (3.1.8). The relative time *t* is determined from the starting time of illumination at the center of the foil. Fixing the position of the incident laser power is too difficult, the x and y positions should be near the center of the foil but the x and y positions have to be measured.

This relation has been derived by analytically solving the heat diffusion equation in rectangular coordinates given by Eq. (1.4.3.2) using the Gaussian function given as Eq. (3.1.10) divided by *k,* as the boundary condition for the first derivative of the temperature in the *z* direction. Taking the temporal limit of this as the foil reaches thermal equilibrium ($t = \infty$) and integrating this over the IR pixel and dividing by its area gives the temperature of the center IR pixel, T_{center},

$$T_{center} = \frac{4\alpha\beta K_{center}P_{laser}}{ab(\alpha^2 + \beta^2)} \sum_{m=0}^{\infty}\sum_{l=0}^{\infty} \frac{\exp\left[-\left(\alpha^2\lambda_l^2 + \beta^2\lambda_m^2\right)/4\right]}{\lambda_{lm}^2}\left[1 - \frac{l_{IR}^2\lambda_{lm}^2}{24} + \frac{l_{IR}^4\lambda_l^2\lambda_m^2}{24^2}\right].$$ (3.1.13)

Solving for K_{center} in Eq. (3.1.13), the absolute calibration coefficient *K(x,y)* is determined.

$$K(x,y) = K_{center}K_{rel}(x,y).$$

Using these analyses, it would be possible to determine the calibration parameters for the each of the channels of the IRVB. Figure 3.1.2.2 shows one example of the mask at the tangential view that (a) is IR imaging data made by illumination with a heat lamp and (b) is the temperature profile at the center of the foil using the data in Fig. 3.1.2.2(a). Figure 3.1.2.2(c) shows the result of Eq.

(3.1.8) with the parameters, $a = 45$ mm, $b = 33$ mm, and $y = 0$ mm because this mask size is about

90 mm x 66 mm. The value of the temperature rise of this result is normalized to the experimental

result as shown in Fig. 3.1.2.2(b). The comparison of the experimental data with the calculated one

shows good qualitative agreement. Figure 3.1.2.3(a) shows the IR imaging data of the mask at the

upper port when illuminated by a heat lamp and (b) is the temperature profile near the center of the

foil using the data in Fig. 3.1.2.3(a). For the calibration using Eq. (3.1.8) the temperature is changed

to $a = 45$ mm, $b = 45$ mm, and $y = 7.2$ mm for this mask because this size of the detected area on

the foil is about 90 mm x 90 mm and the profile position is shifted only 7.2 mm. For the upper port

mask, the center of the foil has a different characteristic, that is a sharp peak on the temperature

profile as shown in Fig. 3.1.2.4. Seeing Fig. 3.1.2.4(a), the brightness spot in the center of the foil is

observed. The reason for this may be a thinner thickness in the center than the other area on the foil

but this difference could not be seen by human eyes.

In the future, calibration parameters from this technique for each spatial channel of the IRVB

will be used.
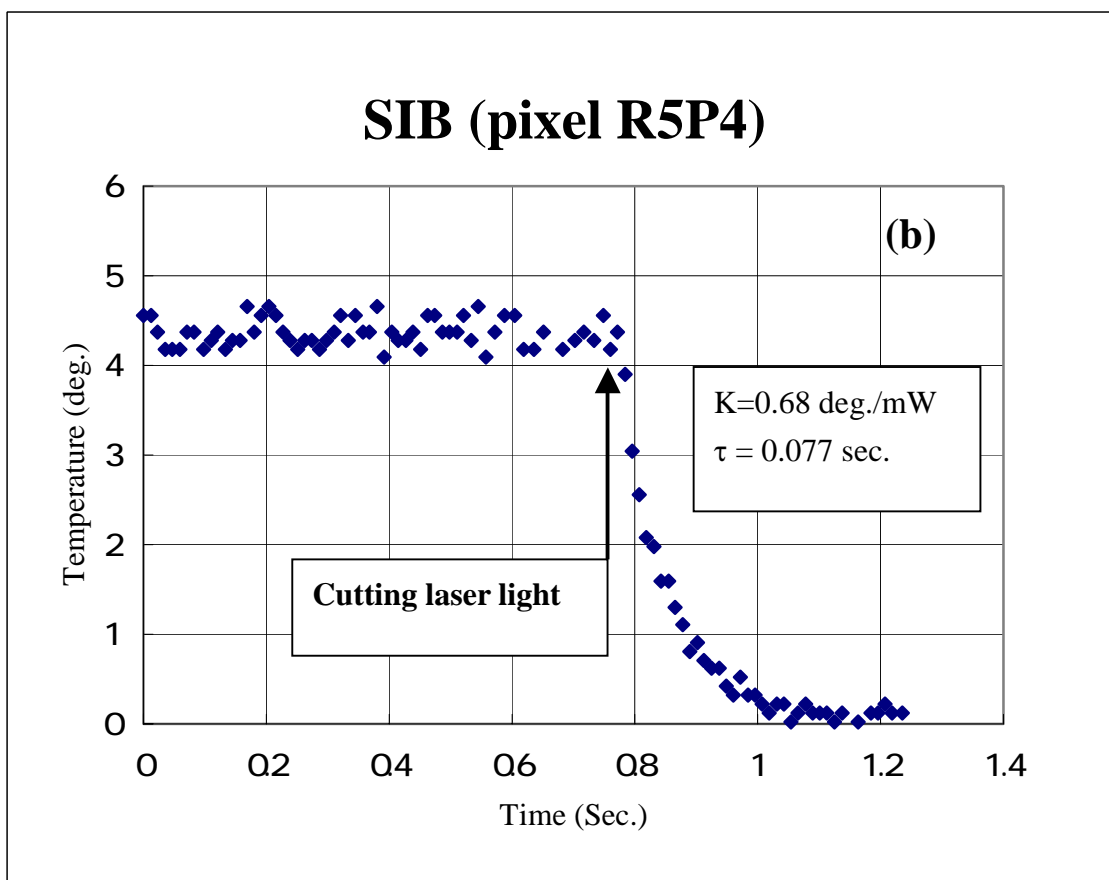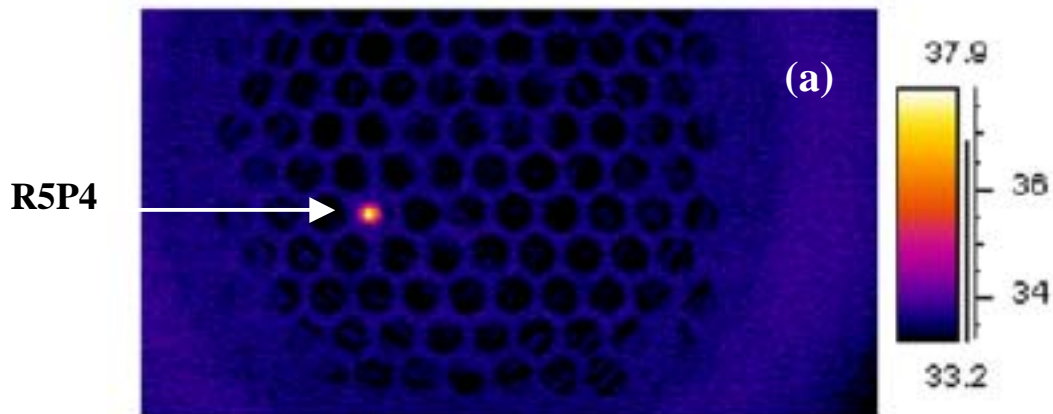
Fig. 3.1.1.1 (a) IR image using the THV900LW of the SIB mask with laser light and (b) the calibration data during the decay time with the temperature rise for pixel R5P4.

(a)

ΔT is the difference of the maximum temperature (the peak of Gaussian profile) to the mask temperature.

LHD center

Toroidal direction

(b)

R12

0.10-0.19deg./mW
0.20-0.29deg./mW
0.30-0.39deg./mW
0.40-0.49deg./mW
0.50-0.59deg./mW
0.60-0.64deg./mW

ΔT is the difference of the averaged temperature on the pixel to the mask temperature

R1

LHD center

Toroidal direction
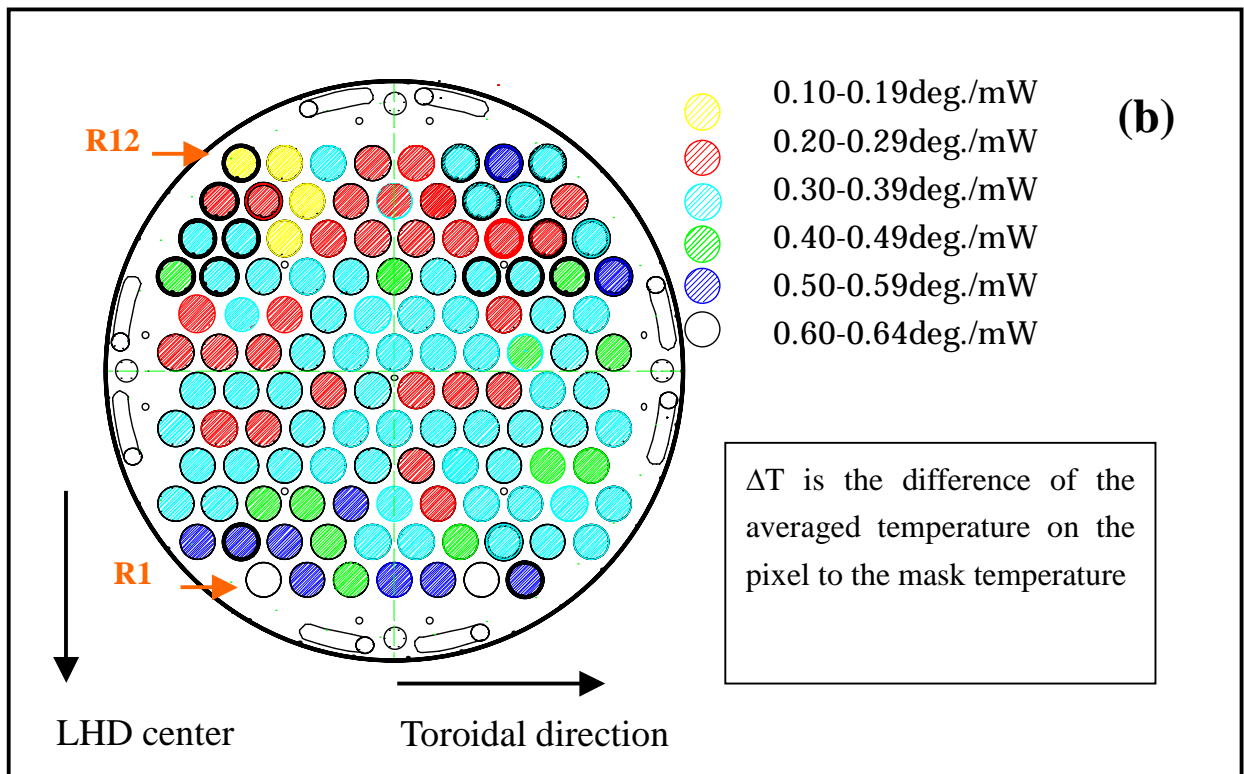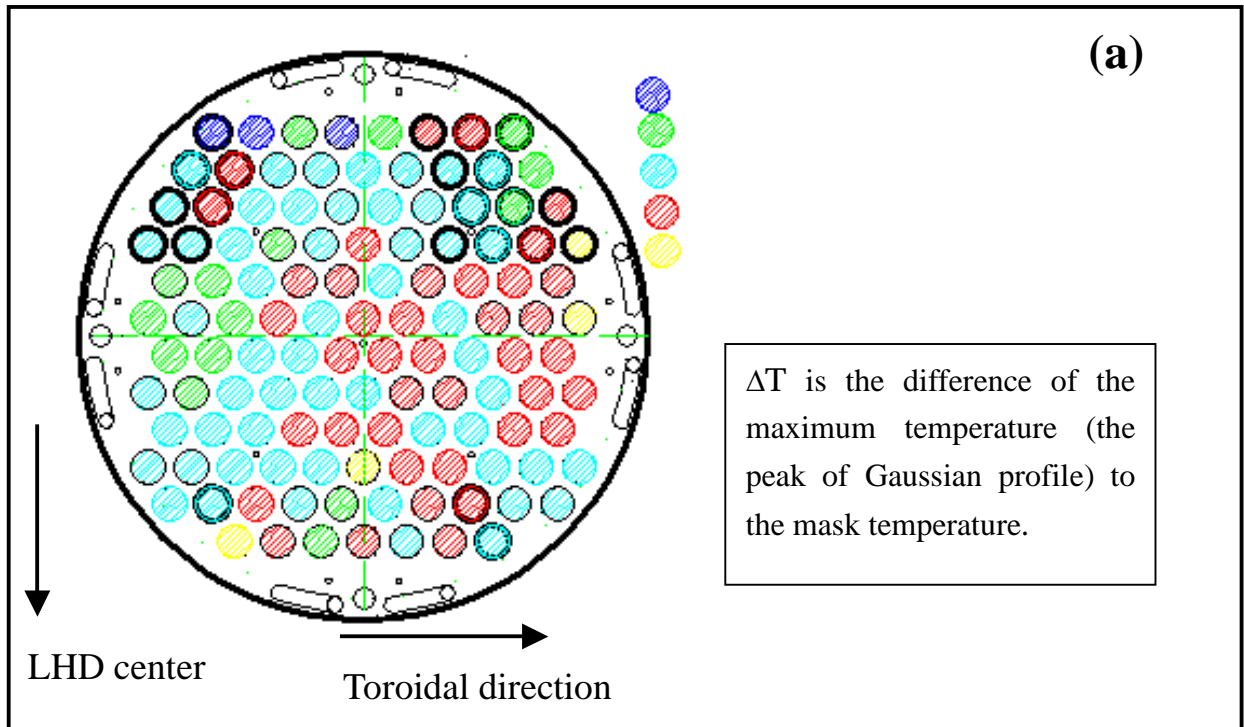
Fig. 3.1.1.2 (a) and (b) show the calibration results of the calibration factor *K* for all pixels. Some pixels with a bold circle near the edge of the mask have cross-talk of the incident signal.
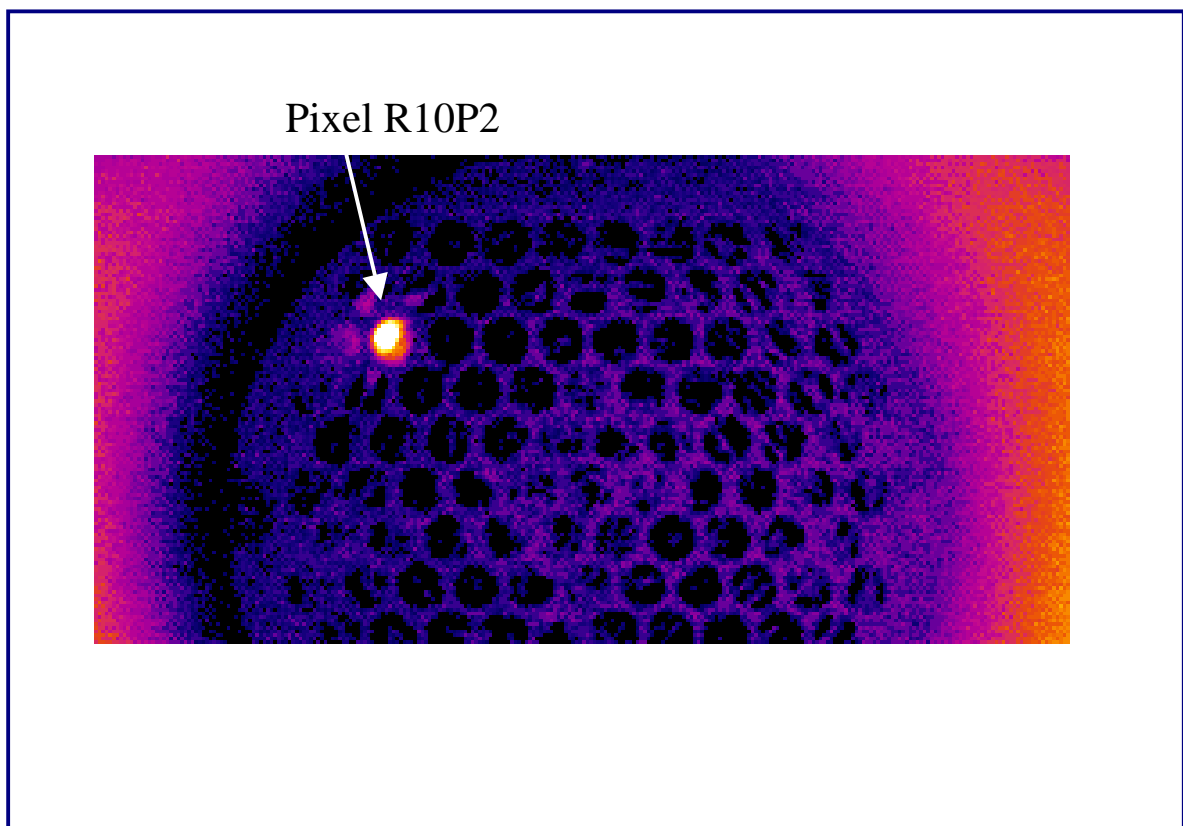
Fig. 3.1.1.3 IR image using the THV900LW of the pixel R10P2 with cross-talk to pixels near the edge.

(a)
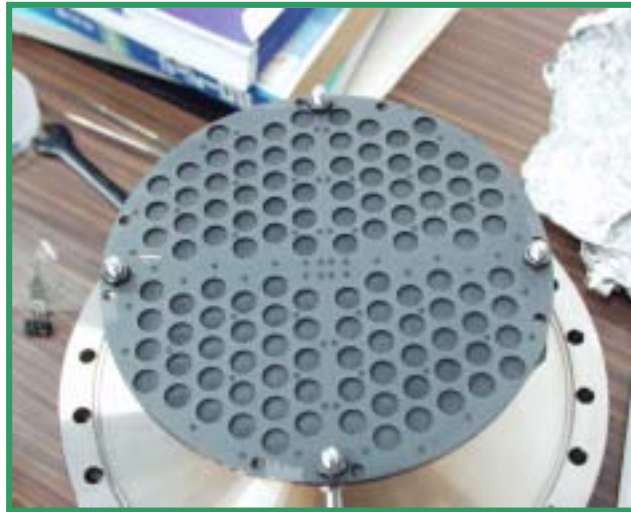
(b)
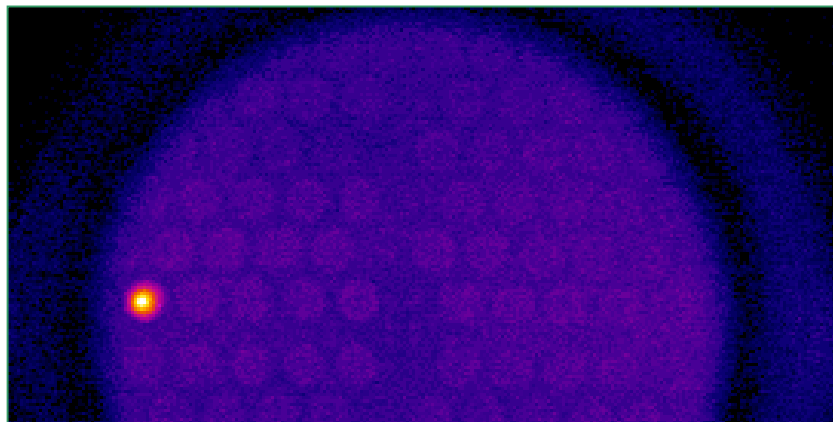
Fig. 3.1.1.4 (a) The picture of the new SIB mask that has been used during 4th and 5th LHD campaign. (b) The IR image using the THV900LW of the new SIB mask with the laser light to heat the edge pixel.
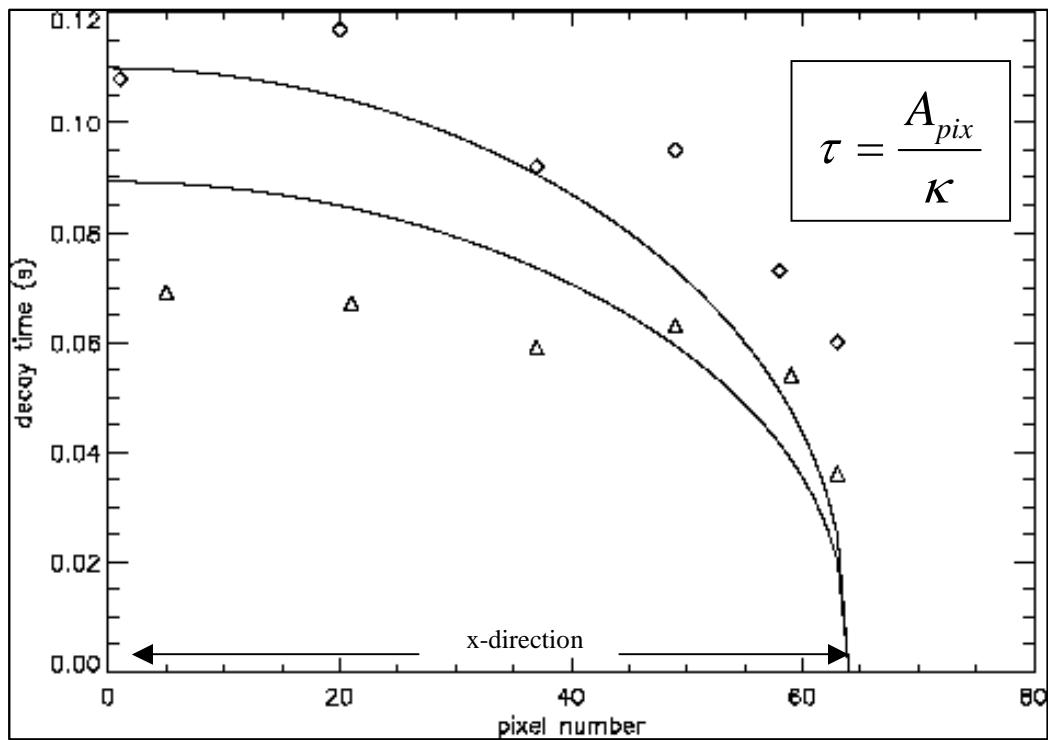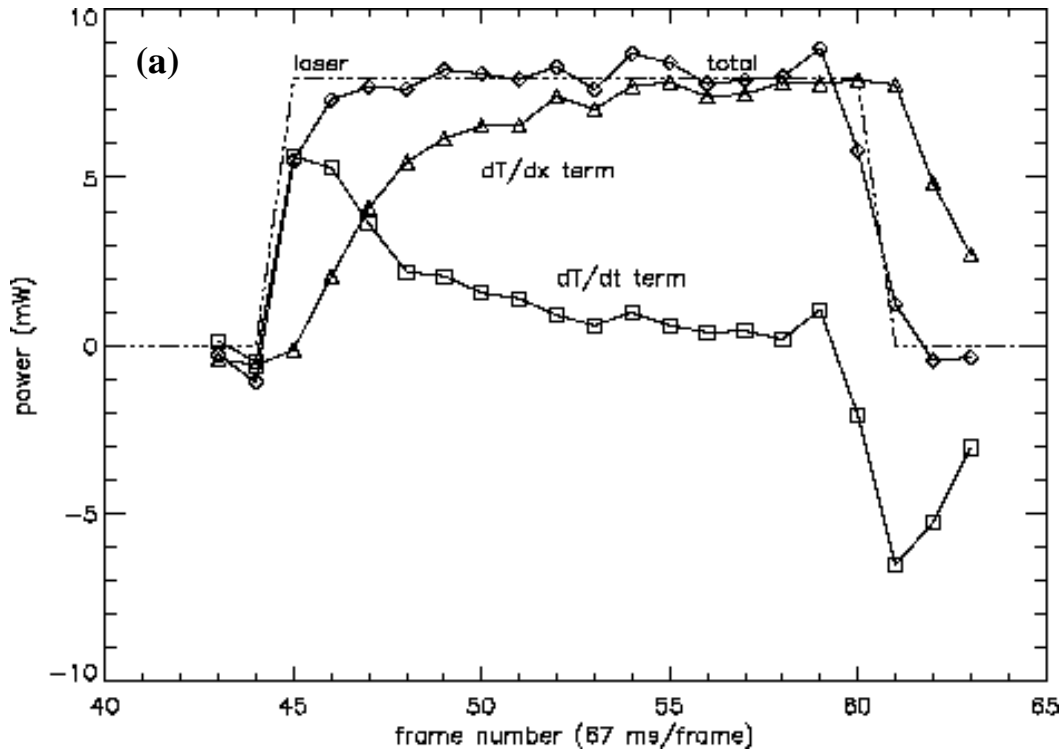
Fig. 3.1.2.1 **(a) The time evolution of the laser power (broken line) and measured laser power (diamonds – total, triangles – time derivative term, squares – spatial derivative term) for $\kappa = 1.2\kappa_{AU}$ and $k = 3.5\ k_{AU}$. (b)The estimated calibration for the full area using He-Ne laser for the cooling decay time, τ using Eq. (3.1.7). The difference of two lines are the vertical position [15].**

(a)

30.5□Ž
30
28
26.1□Ž

°C
34
(b)
32
30
28
26

(c)

Temperature rise (K)

2.258
3
2
1
0
−1

a = 45 mm, b= 33mm
y = 0mm

−40   −20   0   20   40
x

45   45
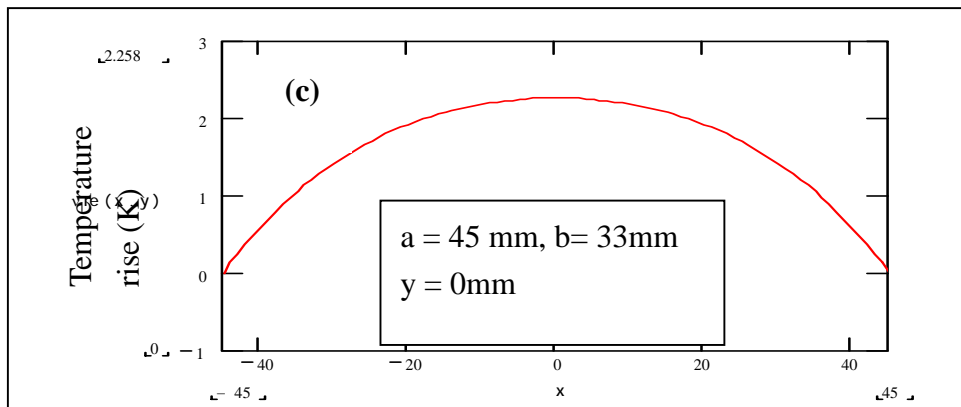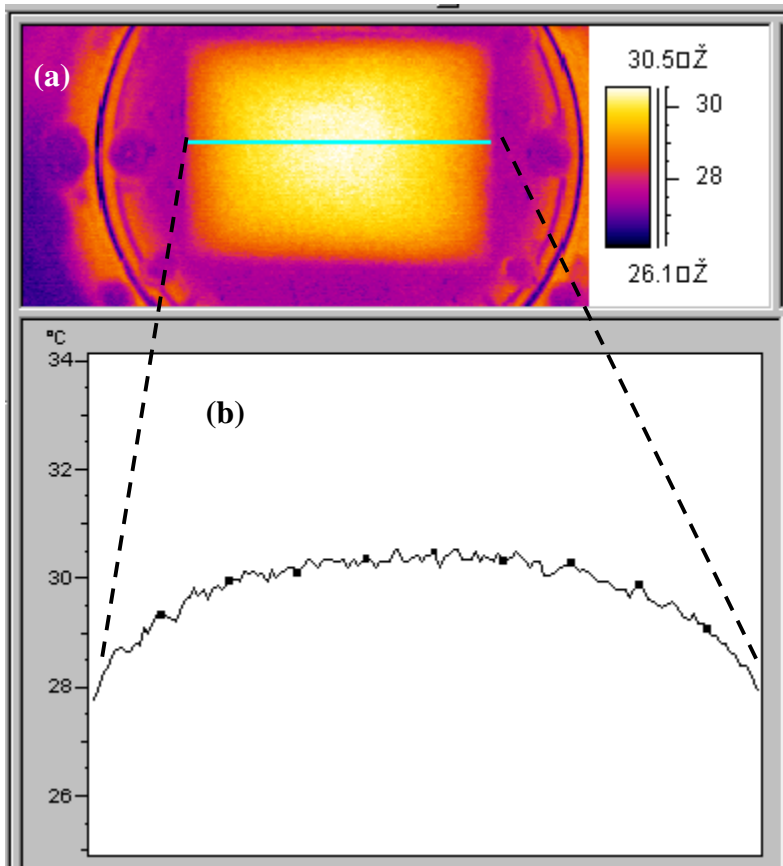
Fig. 3.1.2.2(a) The IR image of the IRVB mask at the upper port illuminated by a heat lamp. (b) is a temperature profile on the center of (a), and (c) is a result of the calculation using Eq. (3.1.8).

57

(a)

35.0□Ž

30

23.3□Ž

°C

34

(b)

32

30

28

26

Temperature rise (K)

$v_{(x,y)}$

3.084

0

4

3 **(c)**

2

1

0

−1

a=45, b=45, x=7.2

−40   −20   0   20   40
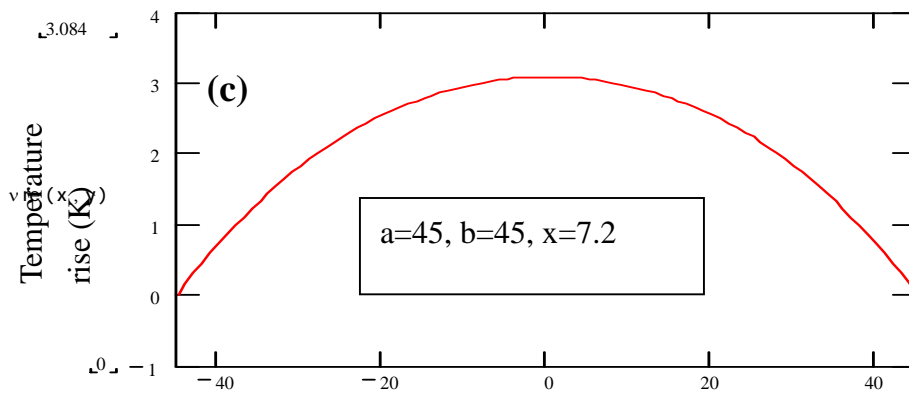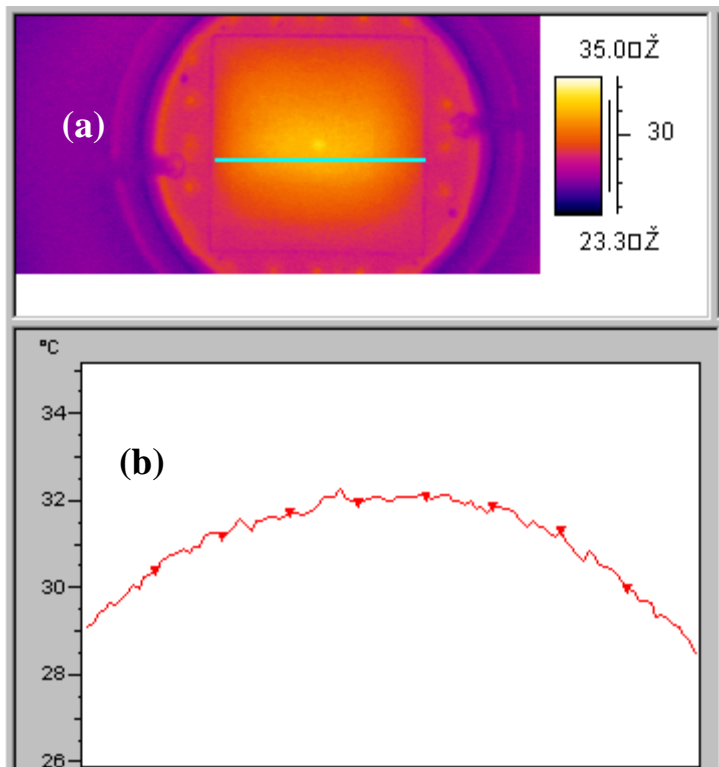
Fig. 3.1.2.3(a) The IR image of the IRVB mask at the upper port illuminated by a heat lamp. (b) is a temperature profile on the center of (a), and (c) is a result of the calculation using Eq. (3.1.8).
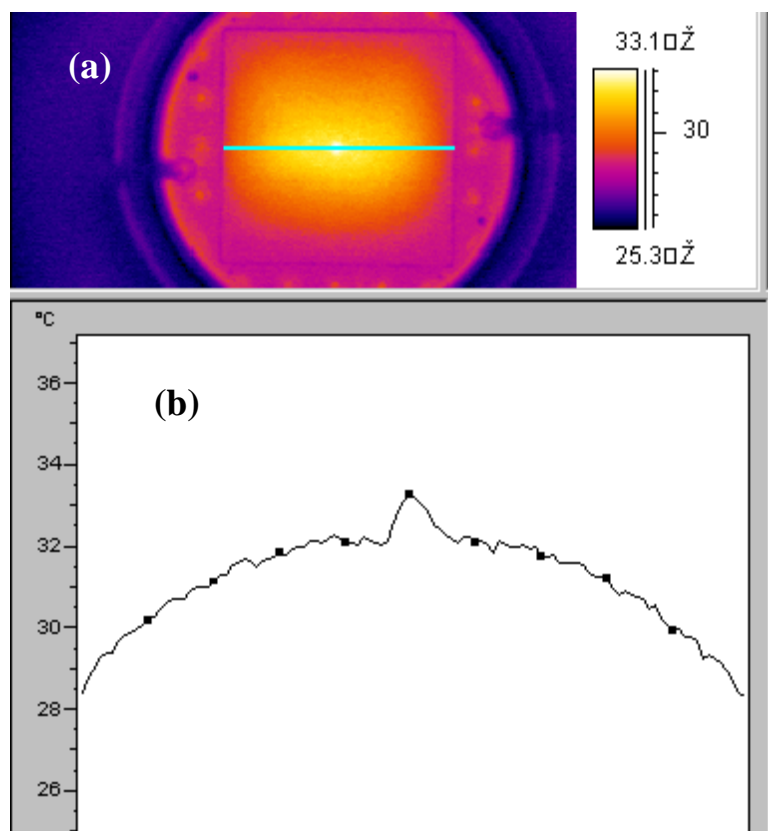
Fig. 3.1.2.4(a) The IR image of the IRVB mask at the upper port illuminated by a heat lamp and (b) is a temperature profile on the center of (a).

3.2 Noise Equivalent Power (NEP)

The noise equivalent power (NEP) is defined as the value of the minimum detectable power by the detecting system. In this system, that is estimated as the incident power flux equal to the noise level. The main source of the noise in the IR bolometer system is the error in the IR bolometer temperature measurement due to the thermal noise of the detector. In this section, the NEP of the SIB and the IRVB systems are shown and the comparison of both NEPs is also shown. For the analysis of the IRVB data, the forward time center space (FTCS) algorithm is used in this section. In addition, the blackbody effect for the detected radiation power as shown in Eq. (1.4.1.4) is not considered in this section.

3.2.1 NEP of the SIB system

Using the estimated incident power to the pixel of the SIB as $S_f = P_{rad}/\pi b^2$, the average temperature over the pixel of the SIB is calculated by integrating Eq. (1.4.3.1) over the pixel area and is given as follows,

$$T_{avg}(t) = \frac{4}{\pi}\frac{P_{rad}}{k \cdot th}\sum_{m=1}^{\infty}\frac{1-\exp[-\kappa\alpha_m^2 t/b^2]}{\alpha_m^4} \qquad (3.2.1.1)$$

where k is the thermal conductivity, κ is the thermal diffusivity, P_{rad} is the incident radiation power, b is pixel radius, th is a thickness of a foil, t is the time coordinate, J_0 is the mth order Bessel function of the first kind and α_m is the m -th root of J_0 Bessel function [13]. For the terms in the series in Eq. (3.2.1.1), only the first term is used, then Eq. (3.2.1.1) can be written as follows,

$$T_{avg}(t) = 4P_{rad}[1-\exp(-\kappa\alpha_1^2 t/b^2)]/\pi\alpha_1^4 k \cdot th \qquad (3.2.1.2)$$

This is a solution to the differential equation give by Eq. (3.2.1.3) which has the same form as Eq. (1.4.1.4). If the blackbody radiation term is neglected and the two-dimensional Laplacian is written as $T_{ave}(t) = \partial^2 T/\partial x^2 + \partial^2 T/\partial y^2$, the incident radiation power is given as,

$$P_{rad} = \frac{\pi\alpha_1^4 k \cdot th}{4}\left(T_{avg}(t) + \frac{b^2}{\kappa\alpha_1^2}\frac{\partial T_{avg}(t)}{\partial t}\right) \tag{3.2.1.3}$$

Using Eq. (3.2.1.3), the standard error analysis is applied. For example when the variable is $x = au \pm bv$, the error of x, σ_x, in terms of the errors in u, σ_u, and v, σ_v is shown [29],

$$\sigma_x^2 = a^2\sigma_u^2 + b^2\sigma_v^2 \tag{3.2.1.4}.$$

The error depends on the error in the IR camera temperature measurement, which is reduced by averaging over space and time. The spatial averaging is made by averaging over the IR camera pixels that make up one bolometer pixel. The time averaging is made by averaging over several IR camera frames. If the signal to noise level is not sufficient, this method can be used with $\Delta t = m\Delta t_{IR}$, where m is the number of the IR camera frames averaged over, Δt_{IR} is the frame interval of the IR camera and the Δt is the time resolution of the IR bolometer system.

The relationship between the original error of the IR camera temperature measurement and the error of averaged temperature on the bolometer pixel consisting of some IR camera pixels and multiple frames is shown as $\sigma_T = \sigma_{IR}/\sqrt{m \cdot N_{IR}}$, where σ_{IR} is the error of the IR camera temperature measurement, σ_T is the error in the averaged temperature on the bolometer pixel, and N_{IR} is the number of the IR camera pixels per bolometer pixel.

Using Eq. (3.2.1.4) to Eq. (3.2.1.3), the NEP, η is estimated as σ_{Prad} of the IR bolometer system, the NEP of the SIB system, η_{SIB} is given by [28]

$$\eta_{SIB} = \frac{\pi\alpha_1^4}{4}k \cdot th\frac{\sigma_{IR}}{\sqrt{mN_{IR}}}\sqrt{1 + \frac{2}{\alpha_1^4\pi^2}\frac{A_{pix}^2}{\kappa^2\Delta t_{IR}^2 m^2}} \tag{3.2.1.5}$$

where, $A_{pix} = \pi b^2$ is the bolometer pixel area.

For the SIB in the 3rd campaign with an aluminum foil using the THV900LW as shown in Table 2.2.1, the noise equivalent power density (NEPD) that is Eq. (3.2.1.5) normalized to the area of the pixel, is calculated to be about 300 μW/cm^2.

3.2.2　NEP of the IRVB system

The basic idea of the NEP of the IRVB system is the same the SIB system. From Eq. (1.4.1.4) and using the forward time center space (FTCS) algorithm as shown in Eq. (1.4.4.1), the solution for P_{rad} is given as,

$$
\begin{aligned}
P_{rad}(x,y,t) = th \cdot k \Big\{ A_{pix} \big[T(x,y,t) - T(x,y,t-\Delta t) \big] / \kappa \Delta t \\
+ \big[4T(x,y) - T(x,y+l) - T(x,y-l) - T(x+l,y) - T(x-l,y) \big]_{t-\Delta t} \Big\}
\end{aligned}
\tag{3.2.2.1}
$$

The standard error analysis is applied to Eq. (3.2.2.1). Using Eq. (3.2.1.4) in Eq. (3.2.2.1) the NEP of the IRVB system, η_{IRVB}, as the error of Eq. (3.2.2.1) is given as [28],

$$
\eta_{IRVB} = 2\sqrt{5}k \cdot th \frac{\sigma_{IR}}{\sqrt{mN_{IR}}} \sqrt{ 1 + \frac{1}{10} \frac{A_{pix}^2}{\kappa^2 \Delta t_{IR}^2 m^2} }
\tag{3.2.2.2}
$$

For the IRVB in the 3rd campaign with a gold foil using the THV900LW as shown in Table 2.2.1, the noise equivalent power density (NEPD) that is Eq. (3.2.2.2) normalized to the area of the pixel, is calculated at about 50 µW/cm^2.

3.2.3　Comparison of the NEP of the SIB and the IRVB

Using the same material parameters, the IR camera, the pixel area and $m = 1$, a comparison is made of the NEP of the SIB and the IRVB. For the area of the pixel, $A_{pix} = \kappa \Delta t$, the NEP in Eqs. (3.2.1.5) and (3.2.2.2) are

$$
\eta_{SIB} = \frac{\pi \alpha_1^4}{4} \frac{\sigma_{IR}}{\sqrt{N_{IR}}} \sqrt{ 1 + \frac{2}{\alpha_1^4 \pi^2} }
\tag{3.2.3.1}
$$

$$
\eta_{IRVB} = 2\sqrt{5} \frac{\sigma_{IR}}{\sqrt{N_{IR}}} \sqrt{ 1 + \frac{1}{10} }
\tag{3.2.3.2}
$$

from $\alpha_1 = 2.4$, the ratio of both NEP is $\eta_{SIB} / \eta_{IRVB} = 5.0$ that means the IRVB system is 5 times more sensitive than the SIB with the same IR bolometer pixel size.

The essential difference of these NEP values is caused by the two-dimensional term of the thermal diffusion in Eq. (1.4.1.4). The SIB system has a boundary condition for each pixel, but in the IRVB system only the edge spatial channels of the foil have a boundary condition. For the other channels of the IRVB, the incident power flux does not escape, this energy is kept on the foil, resulting in a higher foil temperature and therefore more signal.

3.3 Comparison of IR bolometer and other bolometers

3.3.1 Specs of each bolometer system

The resistive bolometer is one of the important plasma diagnostic systems in LHD with about 56 channels already installed. The total channel number of an IR bolometer is a larger than this number of resistive bolometers. This is a one of the merits of the IR bolometer due to the two-dimensional nature of the diagnostic system. The IR bolometer has a large number of channels (exceeding 100) from one IR camera. Currently one of the IRVBs has about 121 channels at the upper port and the other one has about 204 channels at the tangential port, but it is not a maximum number. The resistive bolometer arrays at the lower port have about 20 channels and 12 channels for the same cross-section. The AXUV diode is also used in a similar array system. Using the IR bolometer, these wide two-dimensional views could be measured and by two IR bolometers the three-dimensional position of the brightness radiation region during the collapse could be observed as shown in Chapter 5.

The time resolution of the IR bolometer depends mainly on the frame rate of the IR camera. The frame rate of the old IR camera, THV900LW, is 15 Hz (the time resolution is about 70 ms and the new one, SC500, is 60 Hz (the time resolution is about 15 ms). The fastest one of the bolometers in LHD is the AXUV diode with a time response of 10 μs. The IRVB time resolutions are worse than the present resistive bolometer (about 10 ms), but the latest model of the IR camera has a time resolution of about 2.5 ms, therefore in the future this problem will not be a main problem.

The sensitivity of the IR bolometer as the NEPD for the plasma experiment is about 500 μW/cm^2. At present, only half of the total number of pixels is used to measure the temperature rise on the foil, in the future a more optimal condition will be obtained by changing the FOV of the focus lens of the IR camera. The AXUV diode has the best sensitivity of these bolometers.

The cost per channel of the IR bolometer is better than the other bolometers. The IR camera is expensive but by averaging over many spatial channels, the cost per channel is not expensive, the

IR bolometer is also useful in the case of needing many channels like for a future large experimental fusion plasma device.

As the general value of the sensitivity, the specific detectivity, D* is shown as given by

$$D* = \frac{\sqrt{\Delta f A}}{NEP} \qquad , \quad \Delta f = \frac{1}{2\Delta t} \qquad (3.3.1.1)$$

where Δt is a frame interval, A is the detector area. From $D*$, the IR bolometer as a diagnostic system for the plasma radiation does not have the best time resolution and sensitivity, but as a two-dimensional diagnostics system, the IR bolometer complements the other bolometer systems. The parameters of the different types bolometers in LHD are shown in Table 3.3.1.1.

3.3.2   Comparison of the SIB data and the resistive bolometer data

Using the SIB data, the comparison of the resistive bolometer data and the SIB data in the LHD 3rd campaign shot number #8644 are shown. Figure 3.3.2.1(a) shows the resistive bolometer data on an outer port that is the total radiation power. Figure 3.3.2.1(b) shows the SIB data on the upper port that is the absorbed radiation power on a foil of the mask [21]. The three plots shown are from the different pixels of the SIB mask and the red one 'R5P6' is the pixel near the center of the mask frame and the other ones 'R2P9 and R10P1' are pixels near the edge of the mask frame. R and P numbers are the pixel indices on the mask as shown in Fig. 3.1.1.2. These two pixels do not have a good time response due to the thermal cross-talk between pixels.

This plasma discharge had three pellets but each pellet had a different number of particles. The strongest one is the second at a time of 1.3 s. The fourth radiation peak is the radiation collapse and this discharge was terminated by this collapse. When the plasma discharge is started, the absorbed radiation power of pixel R5P6 was rising and at the second pellet the SIB observed the radiation peak. For the first pellet, the SIB could not sufficiently measure the radiation level. For the third pellet, the SIB measured the small radiation peak and for the final radiation collapse the SIB could

measure the radiation peak. After this collapse the absorbed radiation power quickly decreased. From 2.7 s to 3.0 s, the SIB measured small signals but this signal level was not significant. This is because for the SIB system in the 3rd campaign, the NEP was estimated at about 0.4 mW using Eq. (3.2.1.5) with σ_{IR} of 0.15 K due to the actual fluctuation level of the THV900LW by the effect of the magnetic field from the LHD coils.

In the SIB system with the THV900LW in the LHD 3rd campaign, the SIB system could not measure the peak signals as well as the resistive bolometer because the time resolution was only 15 Hz. But the merit of this SIB system was the two-dimensional images, the mild peaks of the radiation power from the second pellet as measured by the SIB system were considered to be at a sufficient radiation level.

Some images of the SIB system are shown in Fig. 3.3.2.2. Figure 3.3.2.2(a) shows the mask prior to the start of the discharge and the signal due to the radiation from the second pellet at 1.34 s is shown in Fig. 3.3.2.2(b) with the radiation collapse at 2.54 s shown in Fig. 3.2.2(c). The poloidal rotation of the plasma shape in the toroidal direction due to the helical structure is evident in the inclination of the high radiation pixels from the upper left to the lower right on the mask. The center of the mask shows the vertically elongated plasma and pixels around the center absorbed high radiation due to the wide ergodic region in the near proximity of the bolometer at that toroidal angle.

This data is the first result on the LHD by the IR bolometer system, but at present the IRVB system with the SC500 on the upper port has a better time resolution of 17 ms.

Table 3.3.1.1 Comparison with the IR bolometer, a metal foil resistive bolometer and AXUV diode in LHD

Detector type	Resistive bolometer	AXUV diode	IR bolometer
NEPD (optimal)	10 µW/cm^2 (1 µW/cm^2)	60nW/cm^2	500 µW/cm^2 (10 µW/cm^2)
10000JPY/ch	150	15	1-10
Δt (optimal)	10 ms (1 ms)	1 ms (10 µs)	66 ms (1 ms)
Rad-hard	+	-	+
Vacuum feed	- - - (5 wires/ch)	- (1 wire/ch)	+ + (no wires)
Size	(4 ch - 2 x 3 cm)	(20 ch - 1 x 3 cm)	(150 ch -15 x 15 cm)
Other merit		No neutrals	2-D imaging, flexible
Steady-state	-	++ (real time)	+
D* ($(cm\sqrt{Hz}/W)$) [Optimal]	4 x 10^7 [4 x 10^8]	2 x 10^9 [1 x 10^{13}]	5 x 10^3 [4 x 10^6]

(a)

P_{rad} (MW)

time (s)

Pellet injection

(b)

Radiation Power (mW)

- R2P9
- R5P6
- R10P1

Time (sec.)
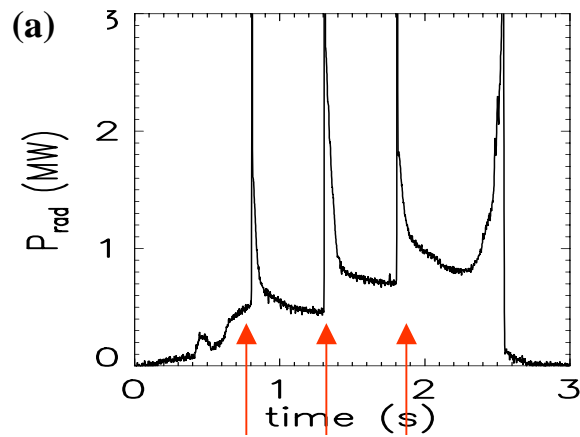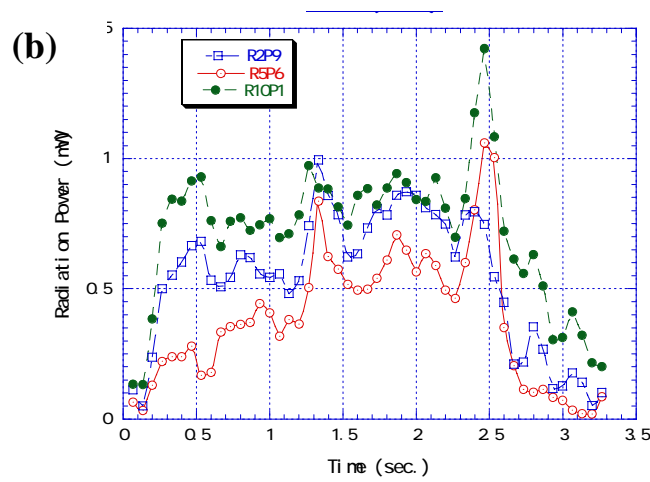
Fig. 3.3.2.1 (a) The total radiation power by the resistive bolometer and (b) the absorbed radiation power by the SIB at three pixels. The red plot in (b) is the pixel near the center of mask frame.

(a)   0.00 s

(b)   1.34 s

(c)   2.54 s

R10P1

R5P6

R2P9
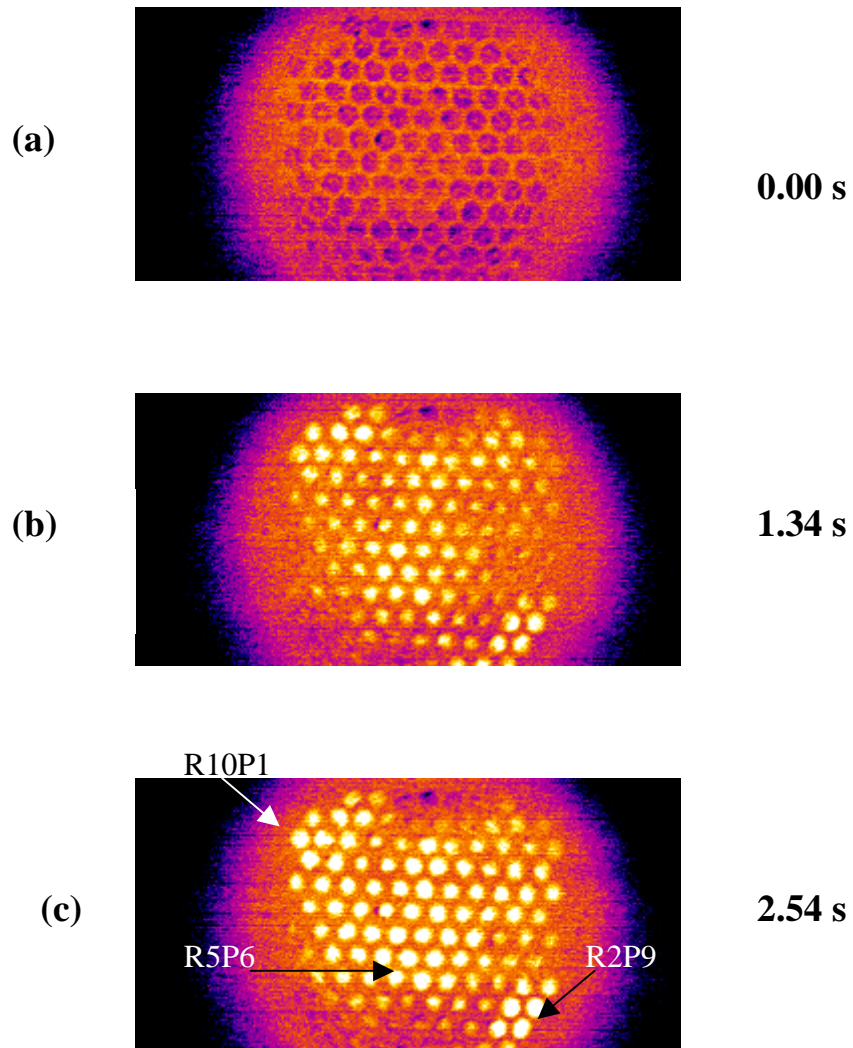
Fig. 3.3.2.2 The absorbed radiation power by the SIB system. (a) is the zero radiation image and (b) shows the second pellet at 1.34 s and (c) shows the radiation collapse at 2.54 s.

3.4   Resolution of IR bolometer system

In this section, the time resolution and the spatial resolution of the IR bolometer system are shown. Basically both the SIB and the IRVB systems have the same method, the case of the IRVB is shown as an example.

3.4.1   Time resolution
3.4.1.1   Minimum time resolution

The time resolution of the IR bolometer system is determined by the relationship between the frame time interval of the IR camera and the NEP of the absorbed radiation power given by Eq.(3.2.2.2). For the SC500, this frame time interval, Δt_{IR} is about 0.017 s. At present, for all discharges during each campaign used the same number of IR camera pixel per the IR bolometer pixel, and the sufficient NEPD = NEP / A_{pix} to measure the plasma radiation was estimated to be under 1mW/cm^2, then each parameter was determined.   For each parameter, the thermal diffusivity, κ, thermal conductivity, k, thickness, th, of the material, and frame time interval , Δt_{IR}, minimum detected temperature, σ_{IR}, of the IR camera, the area of the IR bolometer pixel, A_{pix}, the number of the IR camera pixel on the IR bolometer pixel, N_{IR}, the number of the sampling data, m, of the IR bolometer system, the NEPD with the SC500 on the upper port was estimated at about 270 $\mu\text{W/cm}^2$ with each parameter shown in Table 3.4.1 as case 1.

To keep under 1 mW/cm^2 for this system, the number of the sampling data, $m =1$, is sufficient. In this case the minimum time resolution of the IR bolometer system is determined only by the frame time interval of the IR camera, Δt_{IR}.

If the NEPD is over 1 mW/cm^2, the NEPD can be decreased by increasing m. In this case, the actual frame time interval of the IR bolometer system is shown as $\Delta t = m\Delta t_{IR}$.

The maximum acceptable level of the NEPD can be changed depending on the radiation power level, a condition of the plasma discharge.

3.4.1.2   Relationship between the cooling decay time and the time resolution

The two-dimensional heat diffusion equation with a source term and the blackbody effect as shown in Eq. (1.4.1.1) includes the effect of the thermal diffusivity as κ. At the calibration experiment, each parameter is determined only as the difference between the used foil and the pure material, the cooling decay time, τ, does not have an effect for the time resolution. If the pure material is used and is uniform and the black body radiation is neglected, for the SIB the cooling decay time is determined only by $\tau\,[\text{s}] = A_{pix}\,[\text{cm}^2]/\ \kappa[\ \text{cm}^2/\text{s}]$.

3.4.1.3   Limits of the time resolution

For the IRVB system using the FTCS algorithm, this algorithm has an upper limit for the time resolution as follows,

$$Apix \geq 2\kappa\Delta t$$

For case 1 in Table 3.4.1, $A_{pix} = 0.67$ is a sufficient value for $2\kappa\Delta t = 0.43$. The sampling time, Δt has to be under 0.26 s using the gold foil.

3.4.2   Spatial resolution
3.4.2.1   IRVB

Before the installation of the bolometer pipe, some parameters have to be determined. For the distance from the IR camera to the foil, these parameters, the FOV of the IR camera, the total pixel of the IR camera, the distance from the lens to the foil, a, as shown in Fig. 3.4.2.1 and the facing area of the foil, should be considered. For the distance, a, the FOV of the IR camera on the mask should be equal to the area of the facing foil of the mask.

For the distance from the foil to the plasma, these parameters, the diameter of the pinhole plate, the distance from the pinhole to the foil, b, and the distance from the pinhole to the plasma, c, as shown in Fig. 3.4.2.1 should be considered. To give high spatial resolution, a small diameter of the

pinhole is better. But using the small diameter pinhole, the incident radiation power to the foil is decreased. For the sufficient FOV of the plasma, d, the distance, b, and c, are determined considering the diameter effect of the pinhole plate.

After the installation of the IR bolometer pipe, the area of the spatial channel can be determined after the plasma experiment in the IRVB system. From a numerical point of view, one bolometer pixel equal to one IR camera pixel gives the minimum spatial resolution. At present, the IRVB system on the upper port as shown in Table 3.4.1 uses one bolometer pixel equal to 64 IR camera pixels and the FOV of one IR bolometer pixel at the midplane of the plasma is about 10.2 cm x 10.2 cm as shown in Fig. 3.4.2.2.

For the actual spatial resolution the effect of the NEPD has to be considered in the same way as the time resolution. When one IR bolometer pixel is equal to one IR camera pixel, this result of the NEPD is shown in case 2 in Table 3.4.1. For case 2, the NEPD is about 14 mW/cm^2 and this is over the maximum permissible value for the IR bolometer system which is 1 mW/cm^2. On the upper port, over $N_{IR} = 9$ is need to keep below this level of the NEPD, the FOV at the midplane using that case is about 4 cm x 4 cm.

If the spatial resolution at the expense of the time resolution should be emphasized, that means increasing m, to keep the same NEPD. For example, using the effective frame time interval, $\Delta t = 1/15$ sec with $m = 4$ for the SC500, one IR bolometer pixel consists of 4 times fewer N_{IR}, to maintain the NEPD that is under 1 mW/cm^2 resulting in the FOV at the midplane of 2.5 cm x 2.5 cm.

For the IR bolometer measurement in the LHD, the time resolution is thought to be more important at present, so this one as shown in case 3 in Table 3.4.1 has not been used.

3.4.2.2   SIB

For the SIB system, the spatial resolution is determined by the diameter of one pixel on the

mask frame in addition to the other parameters before the installation of the IR bolometer pipe. The limitation of the spatial resolution is considered with respect to the NEPD as in the IRVB case. The radius of the pixel, r, with the SC500 needed to keep the NEPD under 1 mW/cm^2 is calculated as case 4 as shown in Table 3.4.1. From this result, the radius of the pixel needs to be over 0.8 cm. If this SIB mask is installed on the upper port as in case 1 of the IRVB, the FOV at the midplane is estimated to be about 20 cm x 20 cm.

For the SIB system in the 3rd campaign with an aluminum foil of 0.8 μm, radius of the pixel, r = 0.55 cm and THV900LW, the spatial resolution was 17 cm (toroidal direction) x 26 cm (major radial direction).

3.4.3   Limitations of m and N_{IR} on the NEPD.

From the discussion about the NEP above, the limitations on the parameters, the IR camera pixel, N_{IR} and the number of the sampling data, m are considered. If the working sensitivity of the IR bolometer system is under 1 mW/cm^2, the relationship between m, N and the NEPD as given by Eq. (3.2.2.2) is shown in Fig. 3.4.3.1. For the number of the IR camera pixel, N_{IR}, the shape of the spatial channel is assumed to be a square, then root N_{IR} or one side of this square is used. The curved line on this figure is the limit of the FTSC algorithm and above this line is the working region. The other limit is the maximum value of the NEPD and the working region is under 1 mW/cm^2. Figure 3.4.3.1(a) shows the case of the THV900LW and (b) shows the case of the SC500, the difference of these IR cameras for the NEPD is the frame time interval and the IR camera sensitivity.

Table 3.4.1 Relationship of each parameter for both time and space resolution

|	Case 1	Case 2	Case 3	Case 4 (SIB)
IR camera	SC500	SC500	SC500	SC500
Port	upper	upper	upper	upper
Material	Gold	Gold	Gold	Gold
Area (cm^2)	0.67	0.0105	0.0420	2.01
k (W/cm/K)	3.16	3.16	3.16	3.16
κ (cm^2/sec)	1.27	1.27	1.27	1.27
Thickness	1 μm	1 μm	1 μm	1 μm
Pixel number N_{IR}	64	1	4	192
frame rate Δt (sec)	1/60	1/60	1/60 x 4	1/60
NEP	0.18 mW	0.14 mW	0.036 mW	190 mW
NEPD	0.27 mW/cm^2	14 mW/cm^2	0.86 mW/cm^2	0.90 mW/cm^2
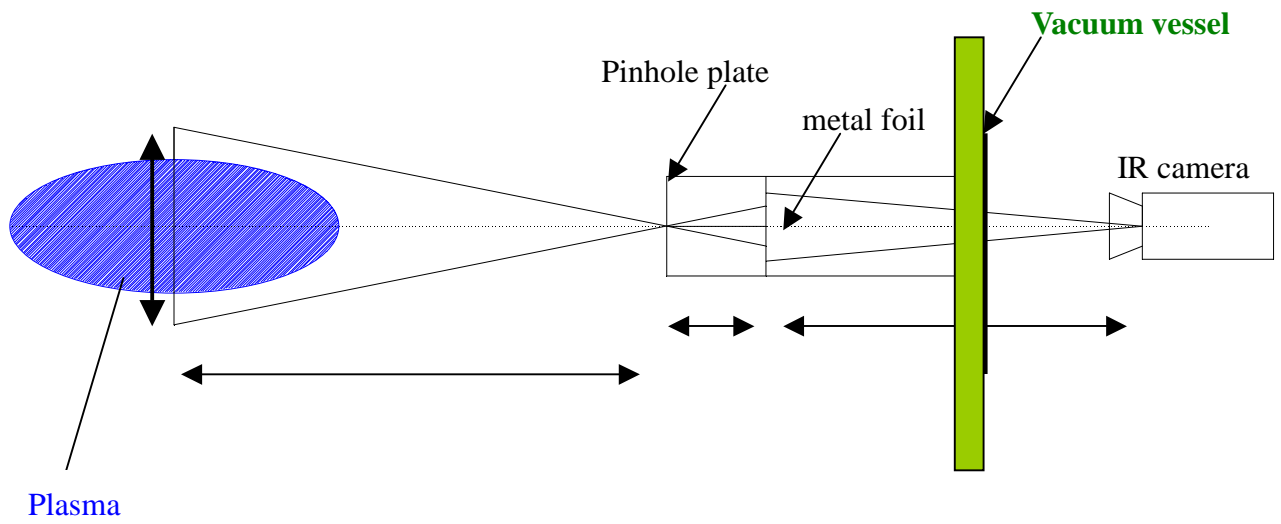
Fig. 3.4.2.1 The model of the bolometer pipe.
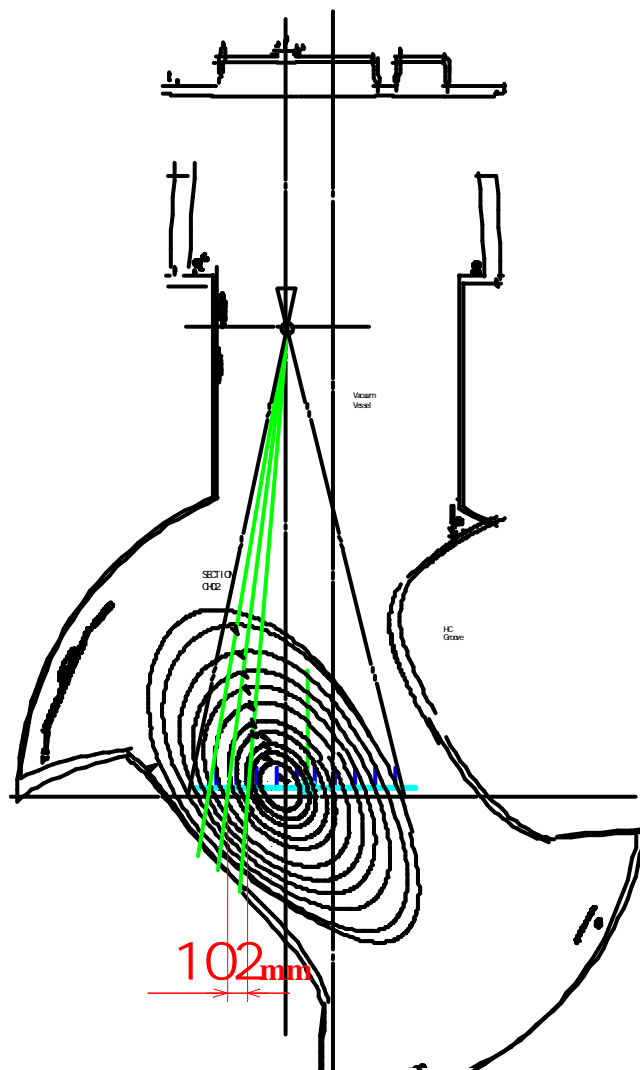
Fig. 3.4.2.2 The spatial resolution of one IR bolometer pixel at the plasma midplane.

(a)

NEPD (microwatts/cm2) Agema FTCS

1×10^2

5×10^2

FTSC stability limit

1 mW/cm² (NEPD limit)

2×10^3

1×10^4

5×10^4

(b)

NEPD (microwatts/cm2) SC500 FTCS

2×10^2

1×10^3

1 mW/cm² (NEPD limit)

FTSC stability limit

5×10^3

2×10^4
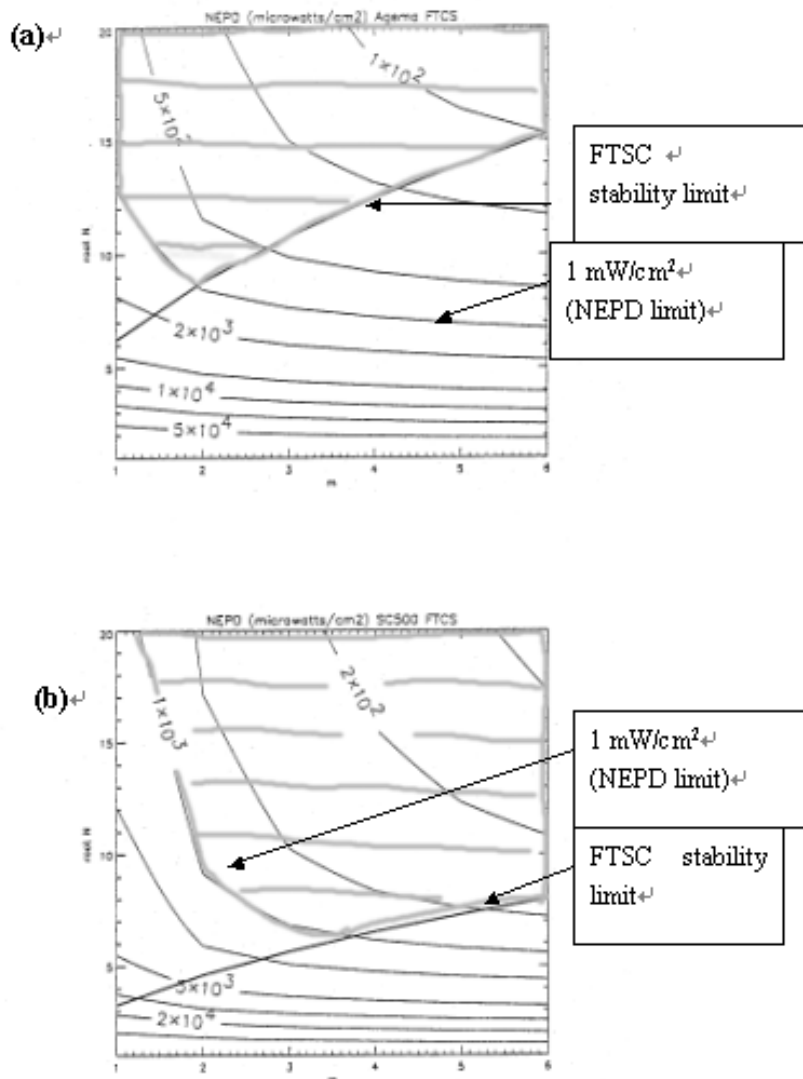
Fig. 3.4.3.1　Noise Equivalent Power Density (NEPD) is chosen to be under 1mW/cm² and $A_{one} / 2\kappa\Delta t_{IR} >= m / N_{IR}$. The region above the orange line is the working region of the IR bolometer system .
(a) is for the THV900LW and (b) is for the SC500 (figures (a) and (b) by B.J. Peterson).

3.5   Analysis of data for IRVB system

3.5.1   Forward Time Center Space (FTCS) algorithm

The spatial channels of the IRVB system have to be determined by the numerical algorithm as shown in Fig. 1.4.4.2. In this section, these algorithm techniques for IRVB data analysis [14] and the actual data images from the resampling of the IR camera pixels and the calculation of the algorithm [18] are shown.

Using Eq. (1.4.1.1) the absorbed plasma radiation power density is estimated from the thermal distribution on the foil. The thermal diffusion in the z-direction (from the plasma to the IR camera) was negligible due to the thin 1 μm foil used and only the blackbody radiation effect was considered in this direction. As one example of the analysis, the images using the THV900LW at the tangential port are shown in Fig. 3.5.1.1. Basically the same method is used for the SC500.

For the original thermal data of the IR camera, an equalization technique is used to avoid the influence of reflection by the mask frame. After this technique the resulting THV900LW thermal image has 136 x 272 pixels at a frame rate of 15 Hz. Of these, the observing pixels viewing the facing foil and the neighboring frame were chosen, then in the case in Fig. 3.5.1.1, the number of pixels, 120 (vertical) x 160 (horizontal) was used as in Figs. 3.5.1.1(a) and (b). It was determined that one bolometer pixel consisted of 100 IR camera pixels, these resampling results using a linear interpolation technique on (a) and (b) are shown in Figs. 3.5.1.1(c) and (d) which are 12 x 16 pixel images. This resampling of the data had a smoothing effect [18].

Starting with Eq. (1.4.1.1) and solving for the radiation power density $S_{rad} = P_{rad}/A_{pix} = \zeta_{rad} k \cdot th$ given by Eq. (1.4.1.2) one obtains three terms corresponding to the two-dimensional Laplacian, time derivative and blackbody radiation terms by the Forward Time Center Space (FTCS) algorithm [20],

78

$$S_L = \frac{k \cdot th}{l^2}\left[4T(x,y) - T(x,y+l) - T(x,y-l) - T(x+l,y) - T(x-l,y)\right]_{t-\Delta t} \qquad (3.5.1.1)$$

$$S_t = \frac{k \cdot th \cdot \tau}{l^2}\left[T(x,y,t) - T(x,y,t-1)\right] \qquad (3.5.1.2)$$

$$S_{bb} = \varepsilon\sigma(T^4 - T_0^{\ 4})_{t-\Delta t} \qquad (3.5.1.3)$$

shown in Figs. 3.5.1.1(e), (f) and (g) respectively where x and y are variables for the horizontal and vertical dimensions of the foil respectively, t is time, th is the foil thickness, k is the effective thermal conductivity of the foil, l is the dimension of the square bolometer pixel ($l^2 = A_{pix}$), κ is the effective thermal diffusivity of the foil, τ is the cooling decay time, σ_{SB} is the Stefan- Boltzmann constant and ε is the blackbody thermal emissivity. T_0 was estimated as the temperature of the mask frame that is the same as the room temperature and T was estimated as the temperature rise on the foil by the incident plasma radiation.

The plasma power density profile as shown in Fig. 3.5.1.1(h) is the result of S_{rad} (h) $= S_L$ (e) $+ S_t$(f) $+ S_{bb}$(g). The scales of (e) and (g) are the same, in addition the scales of (f) and (h) are also the same. For the blackbody term of (g), the emissivity on the foil is estimated with the IR camera side (carbon) of 0.9 and the plasma side (gold foil) of 0.07 [27]. The total emissivity on the foil is approximately one adding both sides.

In the 4th LHD campaign, the numbers of IR bolometer pixels as shown in Fig. 3.5.1.1 were chosen to give a sufficient number for the NEPD as shown in Sec. 3.2, this result using 10 x 14 bolometer pixels is sufficient to measure medium sized radiative structures on the order of 15 – 20 cm.

3.5.2 Other algorithms

Other algorithms for Eq. (1.4.1.1) are discussed in this section. One is the fully implicit and the other one is the Crank-Nicholson (C-N) [20]. The difference between these algorithms are in how to calculate the two-dimensional Laplacian and the time derivative terms, the comparative relationship

with time steps is shown in Fig. 3.5.2.1. These algorithm use two frames of IRVB data and this time frame rate is shown as Δt. The spatial derivation of the FTCS is calculated at t-Δt and the spatial derivation of the fully implicit is calculated at t. For the Crank-Nicholson, the intermediate time between t_1 and t_2 is used.

The fully implicit algorithm as shown in Eq. (3.5.2.1) [20],

$$\frac{\partial^2 T}{\partial x^2} + \frac{\partial^2 T}{\partial y^2} = \left[\frac{T(x,y+l)+T(x,y-l)+T(x+l,y)+T(x-l,y)-4T(x,y)}{l_{bol}^2} \right]_{t=t} \tag{3.5.2.1}$$

$$\frac{\partial T}{\partial t} = \left[T(x,y,t) - T(x,y,t-\Delta t) \right] / \Delta t$$

and the Crank-Nicholson as shown in Eq. (3.5.2.2)

$$\frac{\partial^2 T}{\partial x^2} + \frac{\partial^2 T}{\partial y^2} = \frac{T(x,y+l,t_1)+T(x,y-l,t_1)+T(x+l,y,t_1)+T(x-l,y,t_1)-4T(x,y,t_1)}{2 \cdot l_{bol}^2}$$
$$+ \frac{T(x,y+l,t_2)+T(x,y-l,t_2)+T(x+l,y,t_2)+T(x-l,y,t_2)-4T(x,y,t_2)}{2 \cdot l_{bol}^2} \tag{3.5.2.2}$$

$$\frac{\partial T}{\partial t} = \left[T(x,y,t_2) - T(x,y,t_1) \right] / \Delta t \qquad , \quad t_1 = t - \frac{\Delta t}{2} \qquad t_2 = t + \frac{\Delta t}{2}$$

The accuracy of the three algorithms using the Gaussian function on the foil as given by Eq. (3.1.10) as described in Ref. 15, were calculated as shown in Figs. 3.5.2.2. The solid line shows the Gaussian profile and the broken lines show the result of each algorithm.

The difference between the Gaussian profile and the FTSC algorithm was less than 6 % at the peak, and the result of the fully implicit algorithm is similar to the FTSC, but the difference between the Gaussian profile and the C-N algorithm was less than only 2 % at the peak. Therefore the C-N algorithm was shown to have better accuracy, but experimental results have already some errors about 10 % which is higher than the error of the algorithm error and for ease of use in calculating data the FTSC algorithm is used.

If it is necessary to reduce the NEPD for better accuracy of the images, in the future the C-N algorithm will be used.

IR Camera data
120 x 160 pixels

Resampled data
12 x 16 pixels

(a) ΔT(x,y,t-Δt) [K]

(c) ΔT(x,y,t-Δt) [K]

Δt

(b) ΔT(x,y,t) [K]

(d) ΔT(x,y,t) [K]
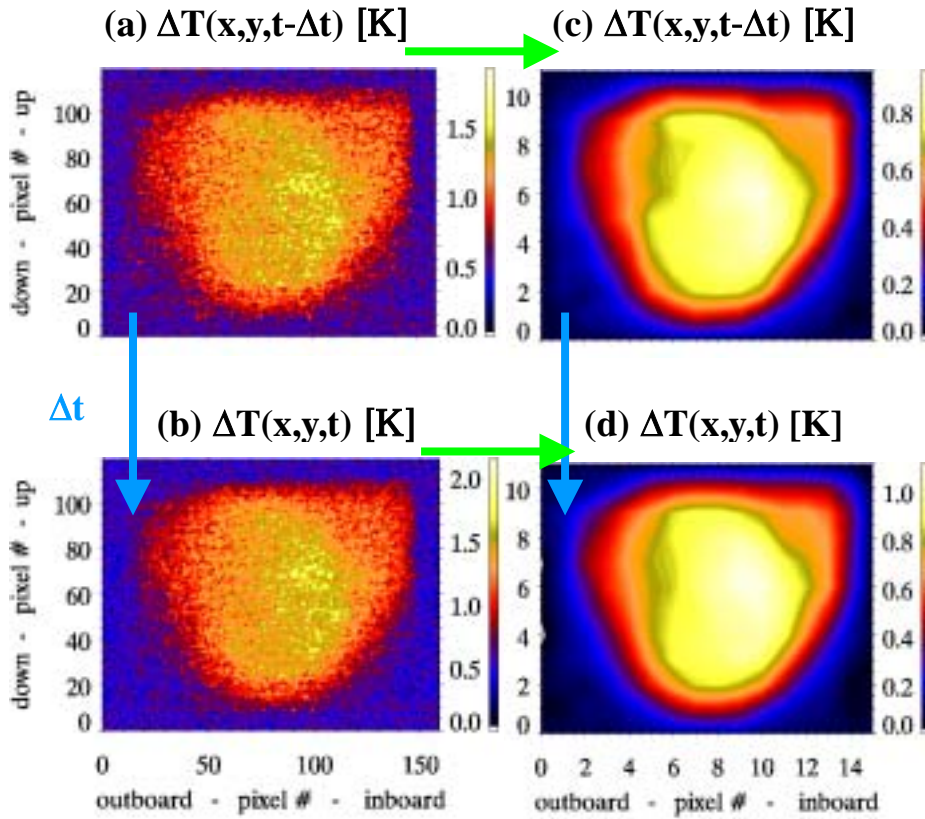
Fig. 3.5.1.1(1/2) Sequence of images showing data analysis technique of the IRVB. (a) and (b) two consecutive 120 x 160 pixel IR camera temperature images. (c) and (d) images (a) and (b) after resampling to 12 x 16 pixels [17].

(e) d^{2}T/dx^2 term   **+ (g) Black body term**

Emissivity

IR camera side (carbon)

= 0.9

Plasma side (gold foil)

= 0.07
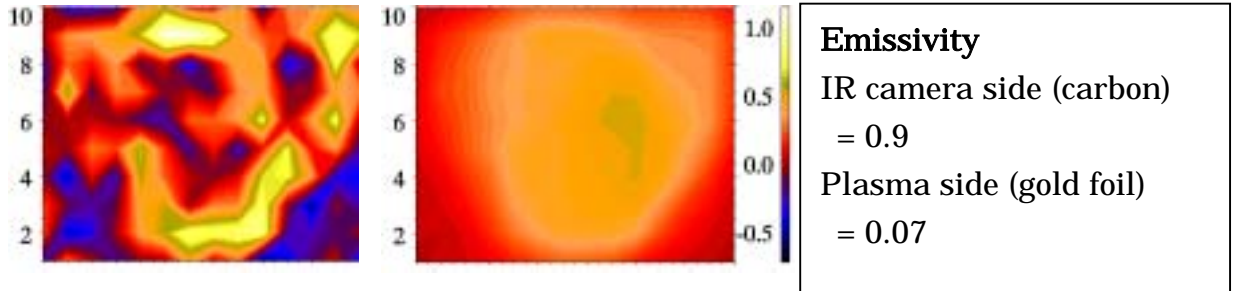
**+ (f) dT/dt term**   **=   (h)   Plasma radiation**
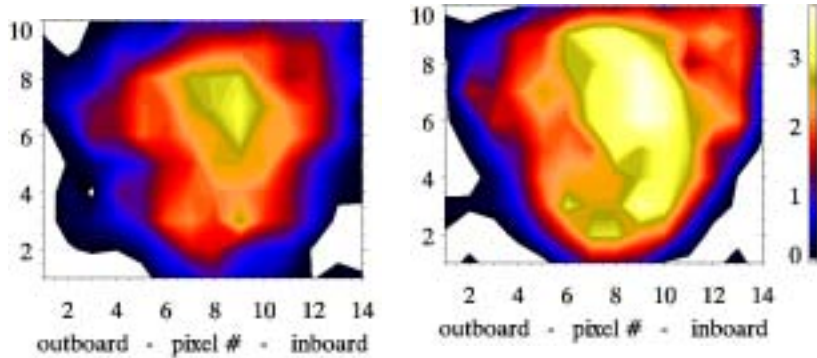
Fig. 3.5.1.1(2/2) Using resampled data (c) and (d), contributions to (h) radiated power density calculation using the FTSC algorithm : (e) two-dimensional Laplacian term, S_L (f) time derivative term, S_t (g) black body radiation term, S_{bb} for (c)+ (d). The plasma power density profile (h) = (e) + (f) + (g). Each scale shows the detected radiation power density (mW/cm^2). The top scale on the right is for (e) and (g), and the bottom scale is for (f) and (h) (images by B.J. Peterson).
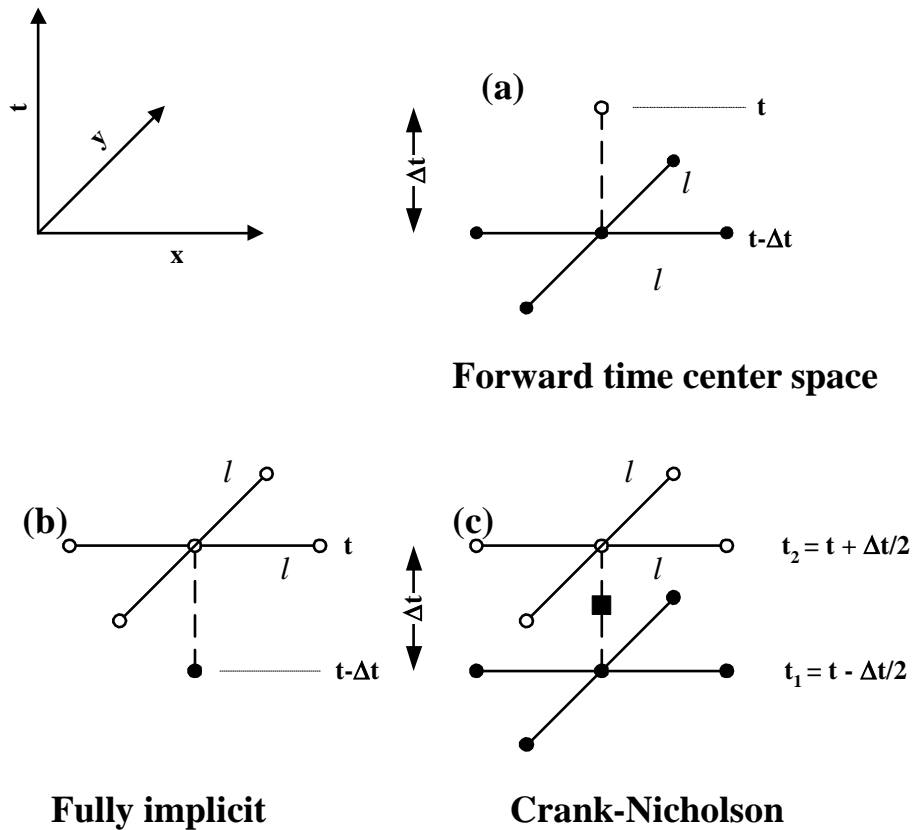
Fig. 3.5.2.1 Three differencing algorithms for the diffusive problems (a) Forward Time Center Space is the first order accurate, but stable only for sufficiently small timesteps. (b) Fully Implicit is stable for arbitrarily large timesteps, but is still only first order accurate. (c) Crank-Nicholson is second order accurate, and is usually stable for large timesteps [20]. The x and y -axis indicate the spatial coordinate and the t-axis shows the time coordinate.

(a)
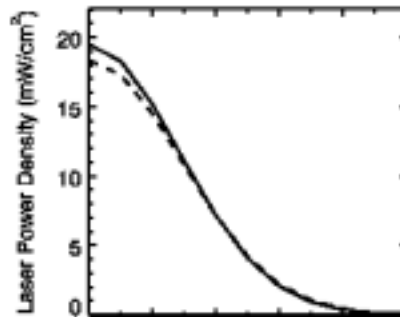
(b)
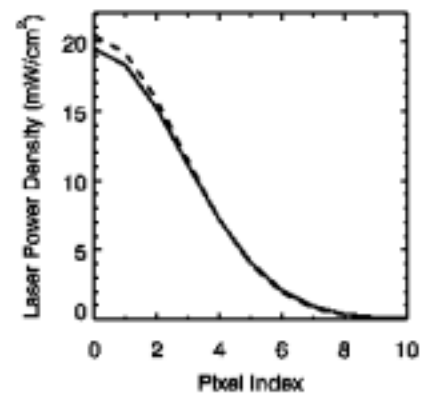
(c)
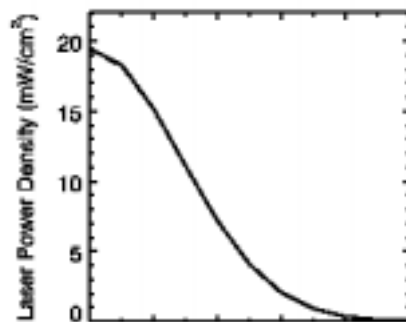
Fig. 3.5.2.2 Comparison with the Gaussian profiles (solid line) and the algorithm results (broken line). (a)FTSC algorithm, (b)Fully Implicit and (c)Crank-Nicholson [28].

3.6   Applicability for future large devices

In this section, the applicability to other devices of the IRVB is shown. For the future fusion device in particular, two problems are a lot of spatial channels with the large plasma diameter and the effect of neutrons from D-D or D-T plasma experiments.

For a lot of spatial channels for the future device, the IR bolometer is well suited to provide broad two-dimensional data as each IR bolometer in LHD has over 100 channels as shown in Table 2.2.1. By one design for a future device the necessary bolometer channels are estimated to be about 300-500 channels. By using the IR bolometer to provide this data one can avoid a vacuum leak by eliminating many feed-throughs.

For the second problem, the effect of neutrons damages some materials including the detectors. To consider each different type of bolometer system, the AXUV diode is the weakest one due to damaged to each diode and is considered difficult to use with strong neutrons in the device. In the case of the resistive bolometer it is considered that some electronic wiring to the resistive grid under the metal foil are damaged by neutrons [30]. In the case of the IR bolometer it is considered that the infrared vacuum window will be damaged. Damage to vacuum windows by neutrons is well documented, but the IR window of the IR bolometer does not need to face directly to the plasma, so this damage will be a small. For the damage to the metal foil, this is basically the same for resistive and IR bolometers. At present a gold foil is used for both bolometers in LHD but different metals also can be used for the IR bolometer. For gold, it is thought that the strong neutrons transmute gold to mercury. To avoid this, another kind of foil can be used for the IR bolometer system.

The limitations of neutrons on the use of the IR bolometer have not been quantitatively estimated. But the IR bolometer is considered stronger than the other bolometers to the effects of neutrons, this is also an advantage of the IR bolometer.

4 Plasma radiation images by IRVB

The LHD plasma has a helically twisted three-dimensional structure resulting from the set of l/m =2/10 helical coils. Using the advantages of the two-dimensional measurement of the IR bolometer system, some characteristic plasma radiation structures have already been shown. The one result of the IR bolometer was shown in Sec. 3.3 using the SIB system. In this section and the next section, only the IRVB data are shown because the IRVB is more sensitive, has flexibility for the analysis and reconstructing images of the plasma radiation profile is easier in comparison with the SIB.

In Chapter 4, the two-dimensional images from the tangential port are introduced. Section 4.1 shows a typical hollow profile of plasma radiation in the LHD, and Sec. 4.2 shows the comparison of the magnetic field calculation and the IRVB data. From these results, what is shown by the tangential IRVB data and where the high radiation sources are located can be understood.

In Secs. 4.3 and 4.4, IRVB images from the tangential port of localized radiation during the movable limiter and the wall-limiter experiments demonstrate the capabilities of the two-dimensional data of the IRVB.

4.1 Radiative structure of helical plasma

Figure 4.1.1 shows the discharge summary for LHD shot # 20740. This shot has three fueling pellet injections. Immediately after injection of the final pellet the plasma was prematurely terminated by radiative collapse as the plasma stored energy was rapidly reduced from its peak to zero, while the NBI continued according to plan. In Fig. 4.1.2, the brightness profiles during the final portion of the NBI discharge are shown from the resistive bolometer array set at a vertically elongated cross-section on the lower port in the field of view (FOV) of the IRVB. This contour plot shows the brightness profile changing from a symmetric profile prior to 1.04 s, to one that is asymmetric on the inboard side during the collapse from 1.09 s to 1.14 s, to a symmetric peaked brightness profile during the unabsorbed beam neutrals by the NBI phase after 1.14 s. This type of asymmetric radiation structure is commonly observed when the plasma reaches the density limit in LHD and has many features similar to a MARFE in tokamaks [31]. Previous observations of this phenomenon using various diagnostics at different toroidal cross-sections have indicated that it may be axisymmetric as in a tokamak, but the actual structure of the LHD has a non-axisymmetric magnetic field and vacuum vessel [32]. For example, at the vertically elongated cross-section the inboard asymmetries in density and radiated power have been observed [31]. At the horizontally elongated cross-section the symmetric up/down radiation profile has been observed [31] and an asymmetric temperature profile with lower temperature on the inboard side [32] indicating stronger radiation on the inboard side has been seen. However the experimental measurements for the full toroidal extent on the LHD were not made, as doing so is difficult only using the existing diagnostics such as the resistive bolometer.

Accordingly, these data leave some unanswered questions about the three-dimensional structure of this asymmetric radiative phenomenon. Therefore it is very interesting to look at this asymmetric radiative collapse with the tangentially viewing IRVB.

The IRVB images from the three time frames corresponding to each of these phases are shown in Fig. 4.1.3. The IRVB image from the period approximately corresponding to the phase with a

symmetric brightness profile prior to $t = 1.04$ s in Fig. 4.1.2 is shown in Fig. 4.1.3 (a). In this image the IRVB observes a very clear helical radiation structure. The lines from "A" to "D" and from "E" to "F" in Fig. 4.1.3(a) represent the position marker of the bright radiation region along the thick ergodic region of the plasma. The nearest point "A" to the mask of the IRVB shows high radiation intensity. As it goes to the far point "D", the intensity is reduced. Where it crosses the other field line at point "F" another bright spot was observed. The point "G" near the center of the IRVB data measures radiation predominantly from the core plasma, and there plasma radiation intensity is lower than from the edge plasma regions as has been typically observed during the steady-state portion of plasmas in LHD [33]. This is a typical helical radiation structure of the LHD plasma from a tangential view. The edge of the FOV as defined by the vacuum vessel walls and other structures are well reproduced by the dark edges of this image. A simultaneous image from a CCD camera using a CIII filter and having nearly the same view of the plasma is shown in Fig. 4.1.4 and these images are used for a reference for visible images and the ergodic regions. These three CCD images have almost the same timing as the IRVB images shown in Fig. 4.1.3.

In Fig. 4.1.3 (b) the next time frame from the IRVB shows the radiation image during the asymmetric radiative collapse corresponding to the time period from 1.09 s to 1.14s. Compared to the previous IRVB image in Fig. 4.1.3 (a), the radiation pattern is changed to a less helical structure and is more localized near the lower inboard edge at point "H". One notes that the maximum radiation power density is different, for example the point "A" in Fig. 4.1.3 (a) is about 4 mW/cm^2 but the point "H" in Fig. 4.1.3 (b) is about 8 mW/cm^2. This image confirms the observation from the resistive bolometers that the asymmetry occurs on the inboard side, and adds new information about the vertical position of the asymmetric structure of the radiation during the collapse of the plasma.

In Fig. 4.1.3 (c) the image from the unabsorbed beam neutrals by the NBI period of the discharge corresponding to the time after 1.14 s is shown. In the resistive bolometer brightness profile data shown in Fig. 4.1.2 a peaked symmetric profile at a lower level compared to the asymmetric period is

seen during this period. This radiation is interpreted to be mostly due to carbon coming from the graphite beam dump as confirmed by the strong CIII signal seen in the shot summary in Fig. 4.1.1(d). In the IRVB image of Fig. 4.1.3 (c), a much stronger signal than that of the previous image during the collapse is observed which is in contrast to the weaker signal seen in the resistive bolometers. The source of this strong central signal in the IRVB image during the period of unabsorbed beam neutrals by the NBI is believed to be the unabsorbed beam neutrals which can be measured easily from the tangentially viewing IRVB compared to the perpendicularly viewing (from the bottom) resistive bolometer arrays.

Each FOV of the bolometers is shown in Fig. 4.1.5. The FOV of the resistive bolometer is shown as the blue square and the FOV of the IRVB from the tangential port is shown as the three green lines of which the two outside lines indicate the FOV and the other one is the center of this FOV.

Two-dimensional images of the helical structure of radiation in LHD have been shown and compare well with CCD images of CIII light. Also, a change of the radiation structure during asymmetric radiative collapse of the plasma has been observed. In addition to confirming the results from the resistive bolometer arrays, which show an inboard asymmetry in the radiation, the IRVB adds information about the vertical position of the asymmetric radiation showing it to be coming from the lower inboard region of the plasma. This result demonstrates that the IR bolometer spatial resolution is adequate to provide new information on the structure of radiative phenomena in LHD [33].
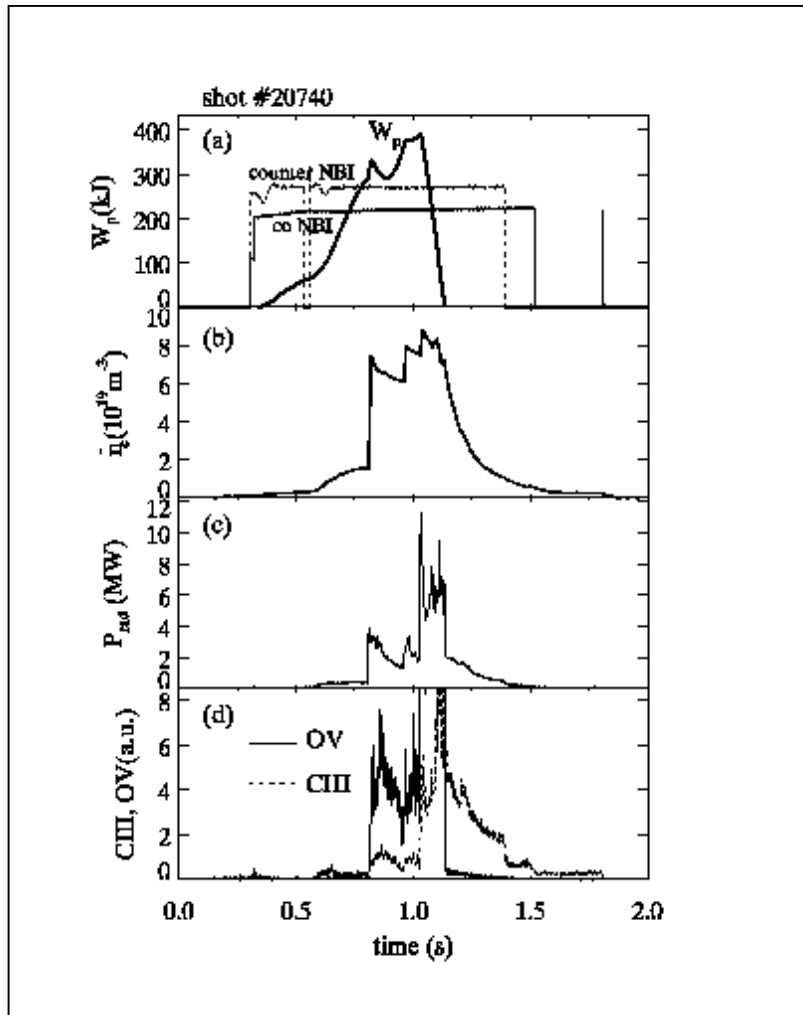
Fig. 4.1.1 Discharge summary for LHD shot #20740 with (a) stored energy from diamagnetic measurements and NBI timing, (b) line-averaged electron density, (c) total plasma radiated power from resistive bolometers and (d) spectroscopic signals from CIII and OV.
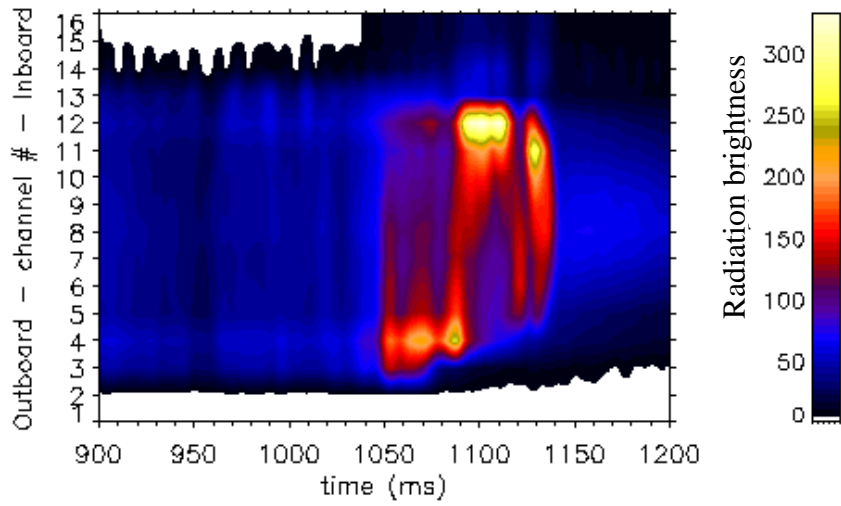
Fig. 4.1.2 Contour plot of radiation brightness from the resistive bolometer array at a bottom port viewing a vertically elongated cross-section (figure by Y. Xu).
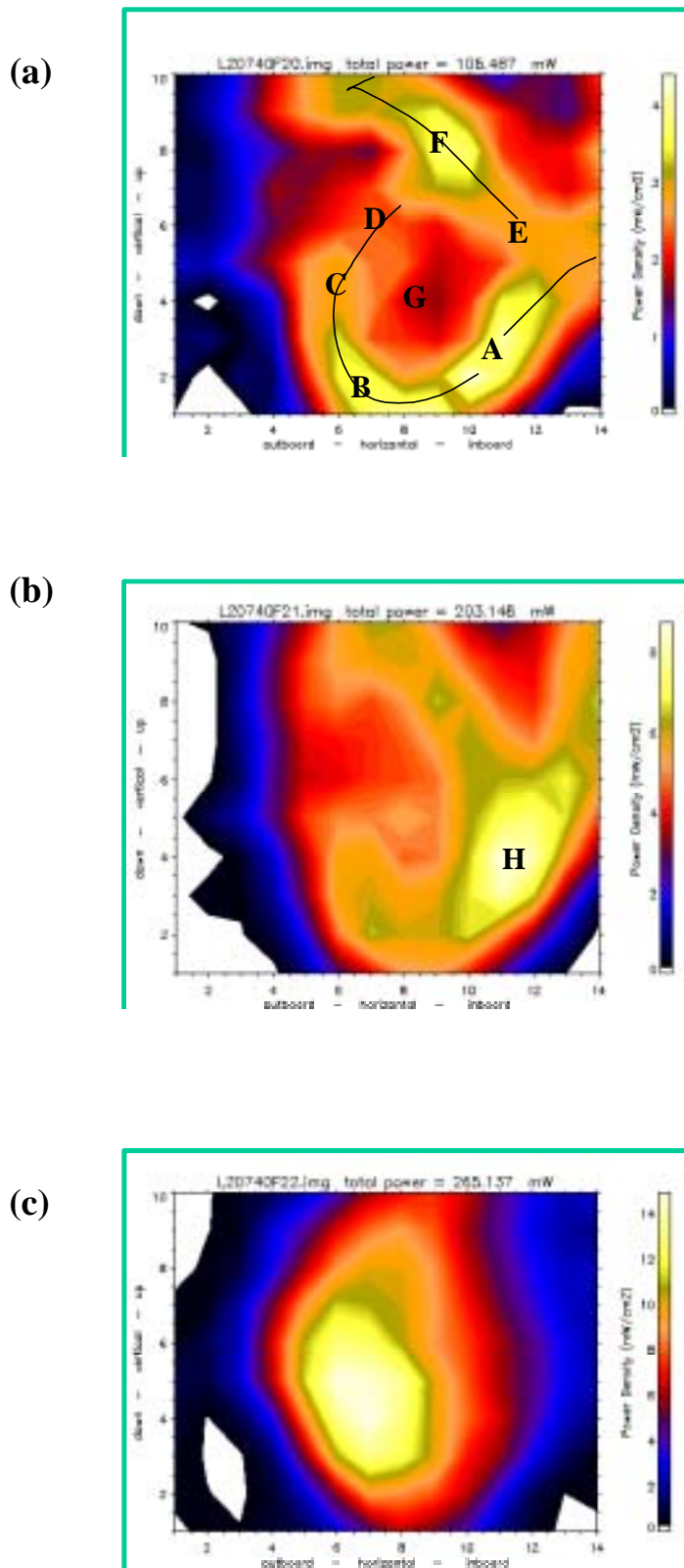
Fig. 4.1.3 Image of two-dimensional radiation from tangentially viewing IRVB at (a) $t = 1.02$ **s, (b)** $t = 1.09$ **s and (c)** $t = 1.16$ **s, for LHD shot # 20740 [33].**
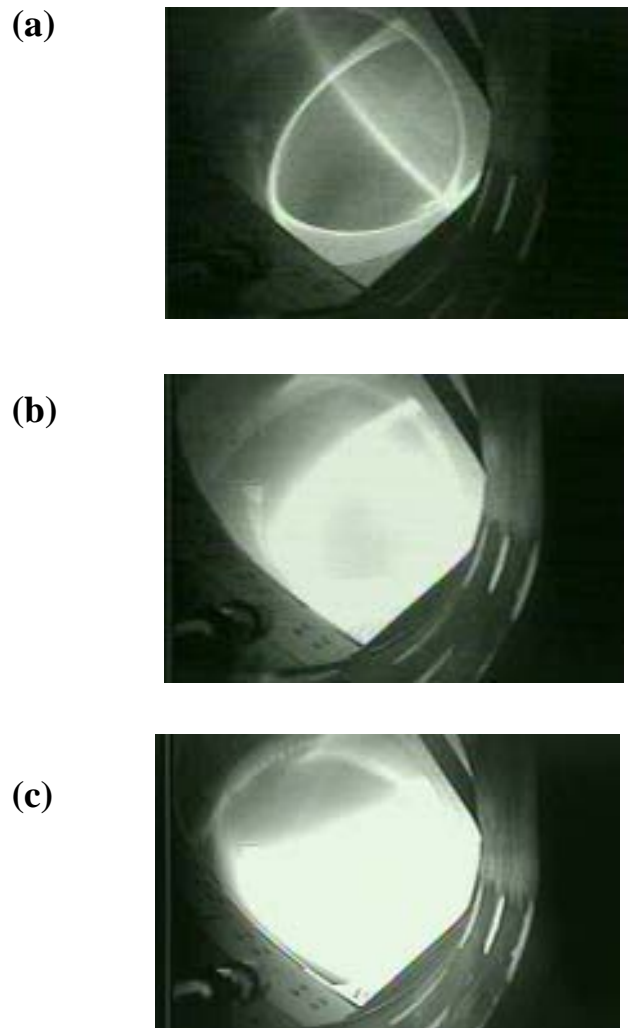
Fig. 4.1.4 Image of CIII radiation from tangentially viewing CCD camera at (a) t **= 1.02 s, (b)** t **= 1.11 s, and (c)** t **=1.17 s for LHD shot # 20740 (by M. Shoji).**
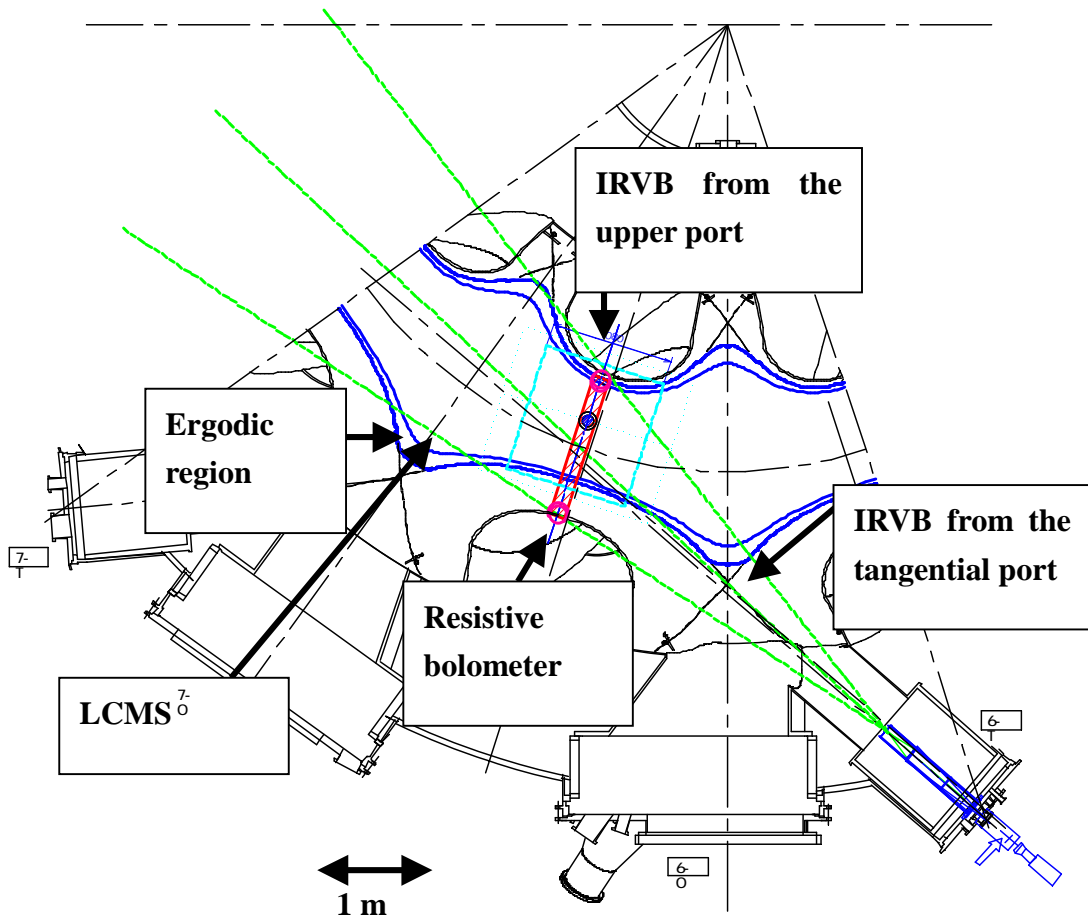
Fig. 4.1.5 the FOV of each bolometer at the midplane. The red one shows the resistive bolometer arrays on the lower port, the green one is the IRVB from the tangential port and the light blue is the IRVB in the upper port. The blue line shows the plasma shape with the LCMS and the ergodic region.

4.2 Comparison of the magnetic field line calculation and the IRVB data

After the LHD 2nd campaign in 1998, the material of the diverter plates was changed from stainless steel to the carbon and the main source of the radiation by heavy impurities was removed. In the absence of heavy impurities radiation profiles should be hollow and the bulk of the radiated power should come from carbon and oxygen radiating from the ergodic region of the plasma outside the last closed flux surface.

Figure 4.2.1 shows the image of the IRVB with the tangential viewing at $t = 0.99$ s for LHD shot # 20744. This image shows the typical hollow profile of the plasma radiation. Figure 4.2.2 shows the results of a magnetic field line calculation with the FOV of the IRVB from the tangential port on LHD [34] and inside the blue rectangle is the FOV of the IRVB. Each blue point indicates each magnetic field line launched in the region around the last closed magnetic surface ($\rho = 1$). Therefore brighter blue regions indicate regions where the IRVB has a more tangential view of the edge ergodic region and should correspond to areas of more intense radiation. However the effects of solid angle are not included in the calculation, therefore the portions of the indicated regions which are far from the IR camera and would radiate less brightly are given the same weight as those near the IR camera that radiate more strongly. But Fig. 4.2.2 very clearly shows the twisted helical structure formed by the magnetic field lines of the ergodic edge region in the FOV of the IRVB.

Comparison between the IRVB data and this magnetic field line model shows the strong helical structure of the plasma radiation predicted by the magnetic field line simulation. In particular the broad radiative structure observed in the lower portion of the field of view (indicated by 'A') is a very bright region due to the fact that it lies in the near field of the IRVB to the core plasma. The bright region in the upper portion of the IRVB image corresponds to the location where the dense regions of the many magnetic field lines overlapped as indicated by point B. The structure seen in the center of the field of view in Fig. 4.2.1 (indicated by 'C') is not so clear in the IRVB

image, which is understood as being in the far field of the IRVB relative to the core plasma. This distance from the IR camera to this region is approximately 6.0 m and incidentally the case of the near field at 'A' is about 1.0 m.

From these results, good qualitative agreement is observed in the comparison of the IRVB image with a corresponding result from the magnetic field line simulation code. From this simulation, the reason for the bright radiation regions having complex structures of the IRVB images using the tangential viewing can be understood, while in the case of using the CAD drawing only it was difficult to understand [35].

For other images from the IRVB, this result of the magnetic field line simulation has been used as a reference for the bright regions.
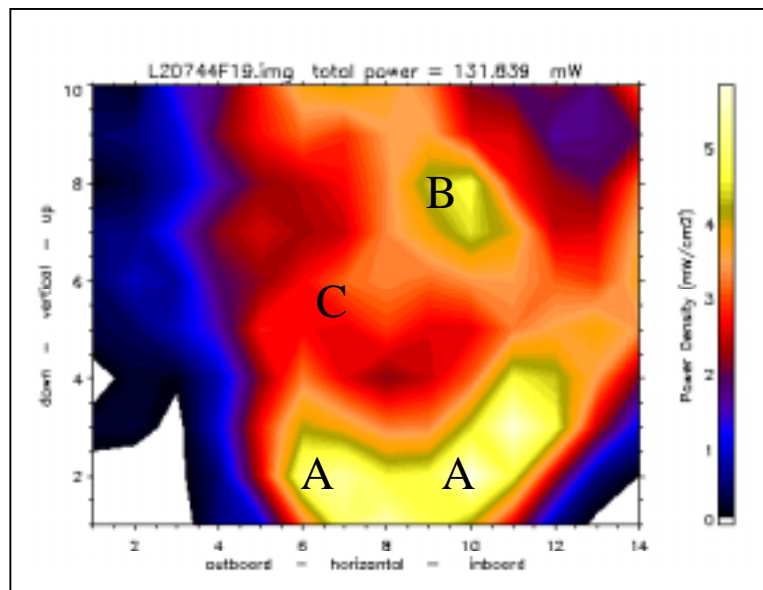
Fig. 4.2.1 Image of two-dimensional radiation from tangentially viewing IRVB at *t* = 0.99 s for LHD shot # 20744. Some letters show the position of the high radiation areas. These are in the positions as in Fig. 4.2.2 [35].
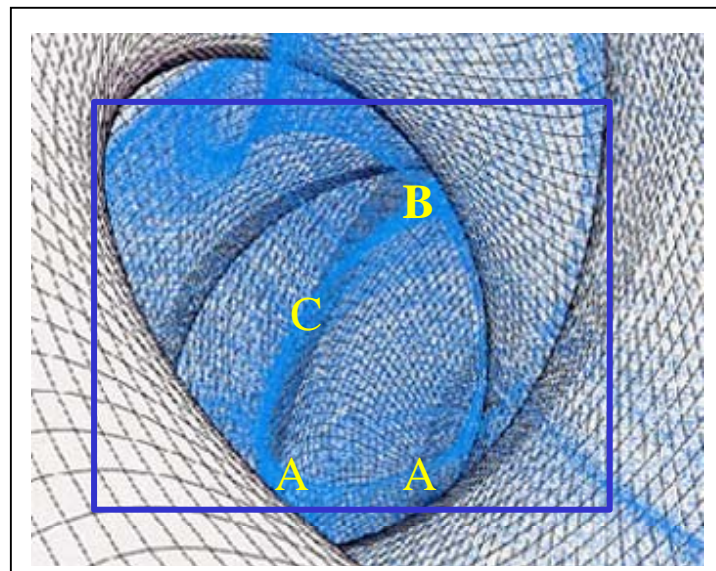

Fig. 4.2.2 The magnetic field line simulation including the ergodic region with a launching point at *ρ* = 1.0. Some letters show the positions of the high radiation areas. These are in the same positions in Fig. 4.2.1 [34].

4.3 Wall limiter experiment

Two different sets of the image data are shown to demonstrate the capabilities of the two-dimensional diagnostics system using the IRVB. The first set of data is from a wall limiter experiment shown in Fig. 4.3.1. This experiment was carried out in the 3rd LHD experimental campaign by changing the distribution of the currents in the helical coil (made possible by three independently driven helical windings in each helical coil) to change the plasma shape such that flux surfaces are fattened in the plane of the helical coils (increasing "gamma"). In this shot, the shot number is #12084, the magnetic field = 1.25 T, the magnetic axis = 3.6 m and $\gamma = 1.28$ ($\gamma = ma_c / lR$, where m is the toroidal pitch number, l is the number of pole, a_c is the plasma radius and R is the major radius). By increasing the γ value, the belly of plasma (this means the thin ergodic side of the plasma at a vertically elongated cross-section) expands in the radial direction and the inboard side plasma touches the wall of the stainless steel at the point of closest approach at the toroidal cross-sections where the plasma is vertically elongated. In this way, the ergodic region of plasma was cut by this wall and the last closed magnetic surface was determined by the position of the wall relative to the plasma. At this point of contact with the wall, the plasma has strong radiation due to the wall interaction and the impurity source coming into the plasma. From the tangentially viewing IRVB, the two dimensional structure during the wall limiter experiment be measured. Figure 4.3.2 shows a CCD data filtered by a H-α filter from a tangential view at the same timing. In this discharge, the recycling of Hydrogen due to heavy plasma interaction should result in a large amount of H-α spectral line, therefore the CCD image with an H-α filter is used as a reference for comparison with the image from the IRVB.

The same region on the inboard side shows intense radiation. Figure 4.3.3 shows the CAD drawing of the IRVB tangential view. The FOV of the CCD data is nearly the same as Fig. 4.3.2.

4.4　Movable limiter experiment

As another representative measurement using the IRVB, the movable limiter experiment is shown in Fig. 4.4.1 [18]. This experiment was performed in the 3rd LHD campaign and the shot number is #11969, the magnetic field = 2.75 T and the magnetic axis = 3.6 m. A large carbon plate limiter is inserted from the lower side. When the movable carbon limiter touches the plasma, this limiter cuts the ergodic region of the plasma and the last closed magnetic surface was determined by the limiter head. It is basically the same effect as the wall limiter, but at a toroidally localized position. With insertion of this limiter, the strong brightness spot at the lower side of the plasma could be measured. Figure 4.4.2 shows CCD data filtered by a CII at the same timing. In this discharge, the bright radiation coming from the carbon limiter was predicted, but only the CCD data filtered by a CII filter was observed from this tangential port, therefore this wavelength for the CCD image is used. This data shows strong radiation from the same region just near the limiter head as shown in the CAD drawing of the FOV of the IRVB including the limiter head in Fig. 4.4.3.

For both results in Secs. 4.3 and 4.4, the discussion using the IRVB and the CCD images about the dominant source of impurities is difficult at present. This investigation should be carefully made by using the data of other diagnostics in LHD.
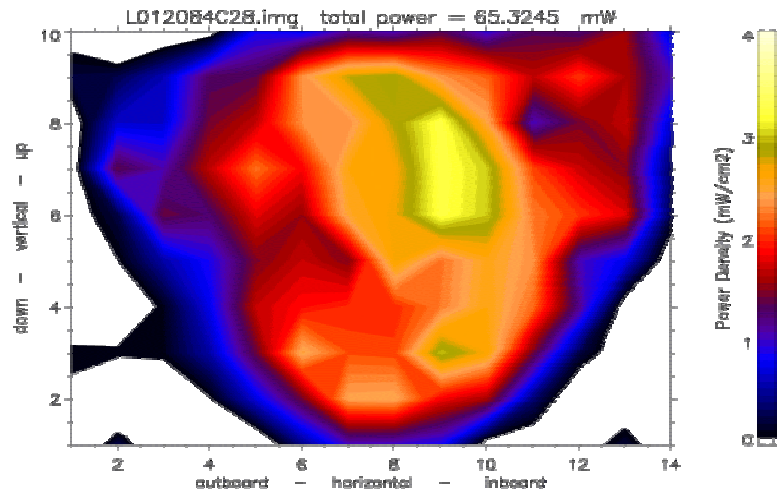
Fig. 4.3.1   IRVB image of the inboard wall limiter experiment from the tangential port for discharge #12084.

Fig. 4.3.2 Tangential view by CCD image with H-α filter for discharge #12084 (by M. Shoji).
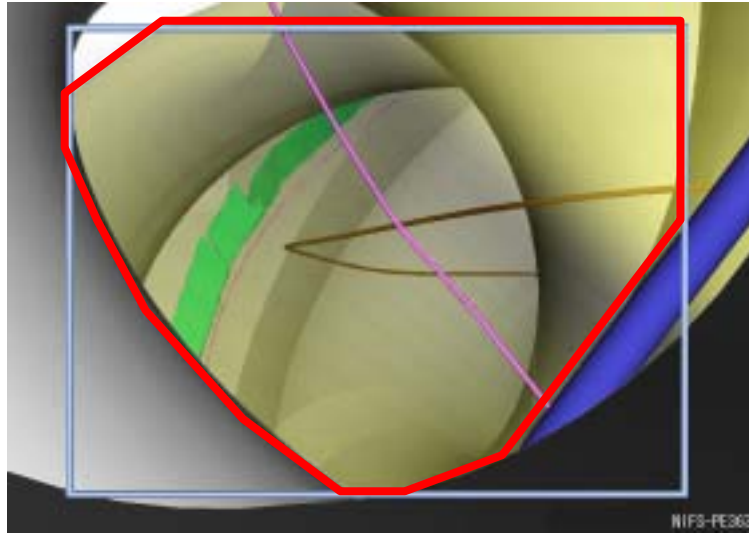
Fig. 4.3.3　CAD drawing of bolometer tangential view. The red line shows the edge of the real FOV of the IRVB. The pink line is the X-point of the magnetic divertor at the 3.6 m configuration. The brown line is the magnetic axis (by H. Kojima).
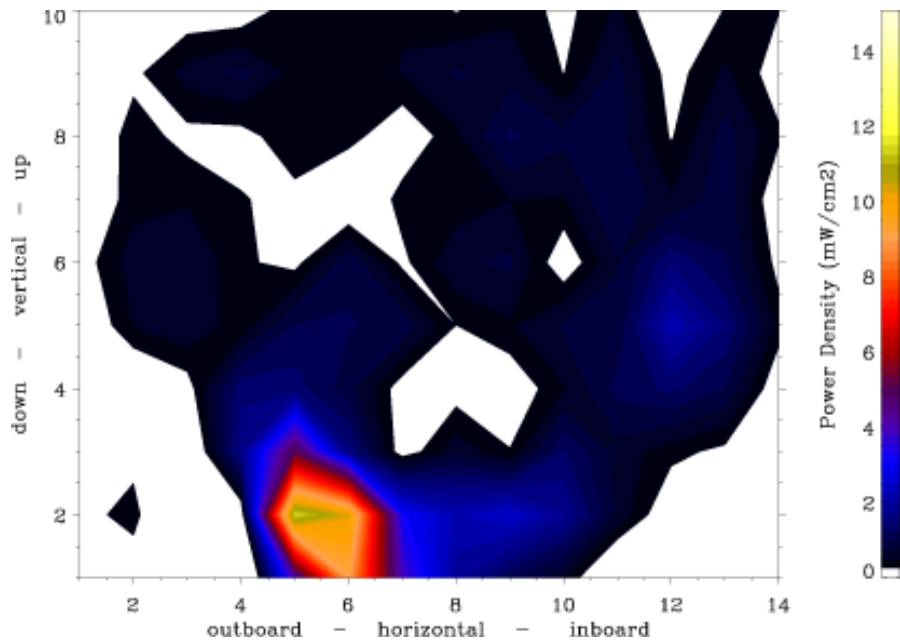
Fig. 4.4.1 IRVB Image of movable limiter experiment for discharge #11969 [18].

Fig. 4.4.2 Image from CCD camera with CII filter for discharge #11969 (by M. Shoji).
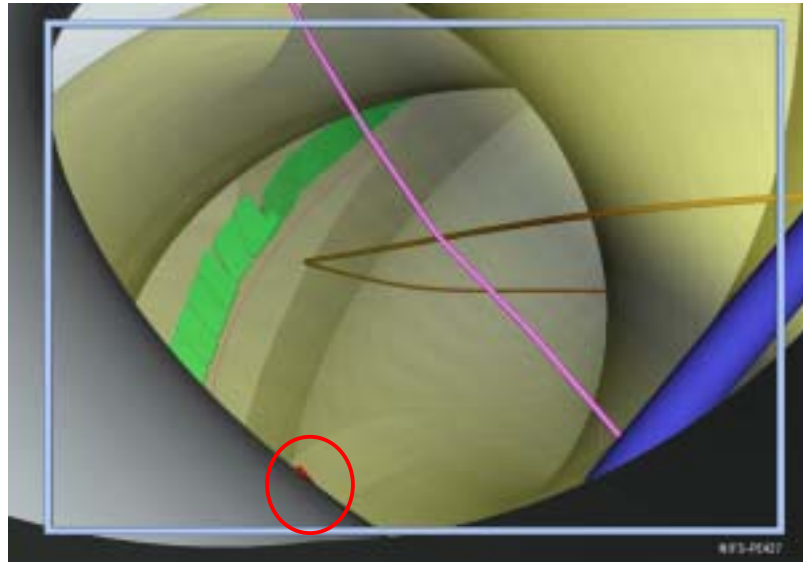
**Fig. 4.4.3 CAD drawing of bolometer tangential view. A pink line is the X-point of the magnetic divertor at the 3.6 m configuration. The limiter is drawn in the lower left side as a small red point in a red circle. The brown line is the magnetic axis (by H. Kojima).**

5 Three-dimensional structure of radiation collapse

5.1 MARFE in Tokamaks

MARFE is a toroidally symmetric loop of intense radiation typically appearing near the inside wall of a tokamak. MARFE is an acronym for Multifaceted Asymmetric Radiation from the Edge. It is poloidally asymmetric and is usually quite localized near the inner wall in tokamak plasmas. The localized radiation region of MARFE has a cold electron temperature of about a few eV and an electron density which is higher than the average density. MARFE phenomena have been observed on some main tokamak machines, for example Alcator C-Mod [36-37], JET [38], ASDEX [38], DIII-D [38], TFTR [38], JT-60U [39], MAST [40], TEXTOR [41-44] and the others.

On the other hand, the density limit is one of the important issues in both tokamak and heliotron/stellarator devices whose goal is the achievement of a thermonuclear fusion reactor. The physical basis for the density limit of plasma is not entirely understood, and quite different density limiting processes appear to be in control, depending on operating conditions, auxiliary heating, pumping, safety factor and pellet fueling. Some of these processes are essentially edge phenomena, while others primarily involve the main plasma, for example the effect of impurity radiation on power balance, leading to a contraction of the current channel due to radial thermal collapse.

The role of magnetic geometry in MARFE formation has been assessed up to the present mainly in numerical modeling. The poloidal homogeneity in the heat flux from the plasma core caused by the Shafranov shift of magnetic surfaces or the existence of an X-point was dependent on a boundary condition [41]. In other work, poloidally asymmetric recycling properties resulted from the proximity of the first wall on the inboard side [42].

5.2 Asymmetric radiation collapse in LHD

In helical devices, the radiation-induced density limit has particular importance, since it is a main cause leading to collapse of the plasma when the radiated power increased with density exceeds some

fraction of the deposited power. In LHD, a MARFE-like inboard asymmetric radiation structure has been observed already [31-32]. In Ref. 30-31, the resistive bolometers measured only at two cross-sections by two arrays as shown in Fig. 5.2.1. Figure 5.2.1(a) shows the time evolution of the radiation brightness profile at the vertically elongated cross-section that shows the inboard asymmetry during the collapse. The other case of the horizontally elongated cross-section is shown in Fig. 5.2.1(b) that shows the symmetric radiation structure during the collapse. Other signatures of the asymmetric radiation collapse in LHD were observed in the electron temperature by the YAG Thomson scattering ($\lambda = 1064$ nm) from the horizontal elongated cross-section and in the electron density by the far infrared (FIR) interferometer ($\lambda = 119$ μm) from the vertically elongated cross-section. Figure 5.2.2 shows the asymmetric electron temperature during the radiation collapse. At 1.8 s, an asymmetric profile was observed in the difference of both side profiles [32]. Figure 5.2.3 shows the comparison of the brightness profile evolution by the resistive bolometer as a contour plot and the FIR interferometer for the LHD shot #3574 [31]. The peaks in FIR line densities are shown with triangles. At the three inboard channels, the interferometer signals are degraded due to the reduction of the beat signal amplitude of the heterodyne interferometer. As one example of the degraded channels, the FIR signal of the line density at R = 3.4 m is show in Fig. 5.3.3 (b). On this FIR channel, the deflected signal due to the high gradients was observed from about 0.96 s to 0.98 s, the period when signal degradation is shown in Fig. 5.2.3 (a) by two plus signs connected by a line.Therefore the phenomenon of an inboard side radiation collapse similar to MARFE in the tokamak was observed at the vertically and horizontally elongated cross-sections, but no information was given on the other cross-sections. To study more details of the asymmetric collapse in LHD, using the two IRVBs the three-dimensional position of the asymmetric radiation source region at the collapse is determined in Sec. 5.3.
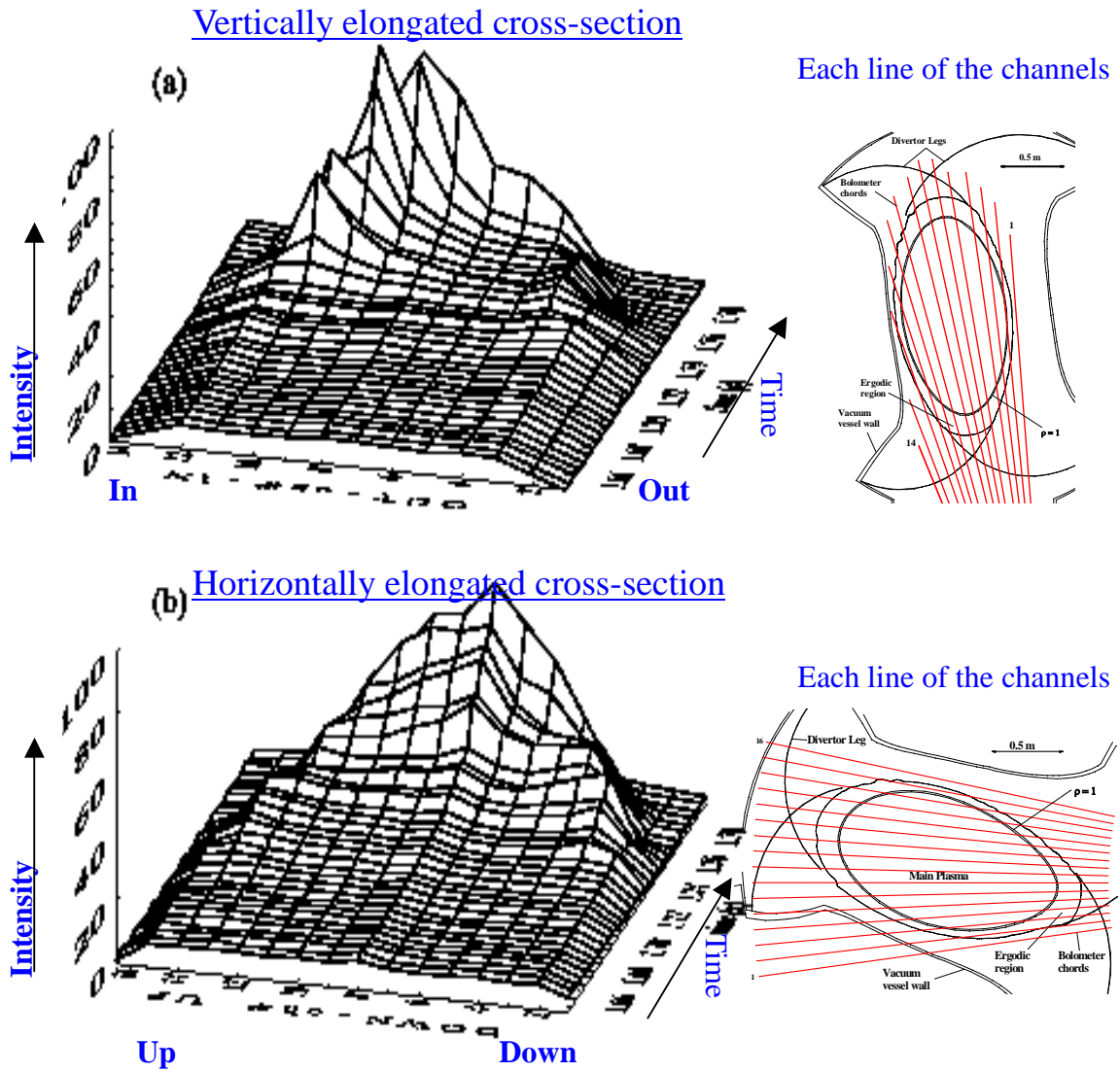
Fig. 5.2.1 Time evolution of the radiation brightness profile by the resistive bolometer arrays for discharge #10272 measured at (a) the vertically elongated cross section and (b) the horizontally elongated cross section [31].
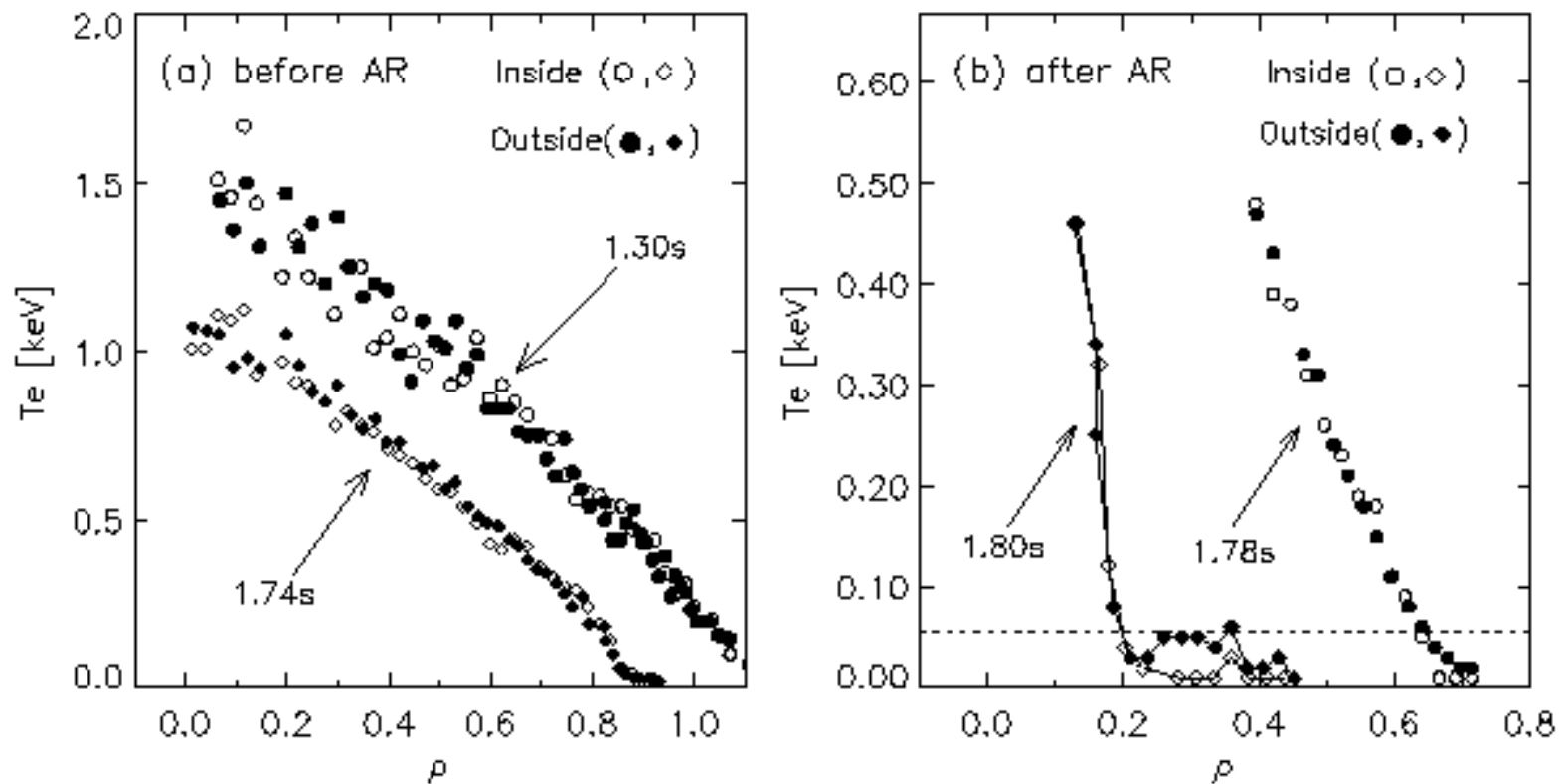
Fig. 5.2.2 Temperature asymmetry radiation (AR) collapse (a) before the radiation collapse and (b) after the radiation collapse. At 1.8 s, asymmetry profile of the electron temperature by the Thomson scattering was observed [32].
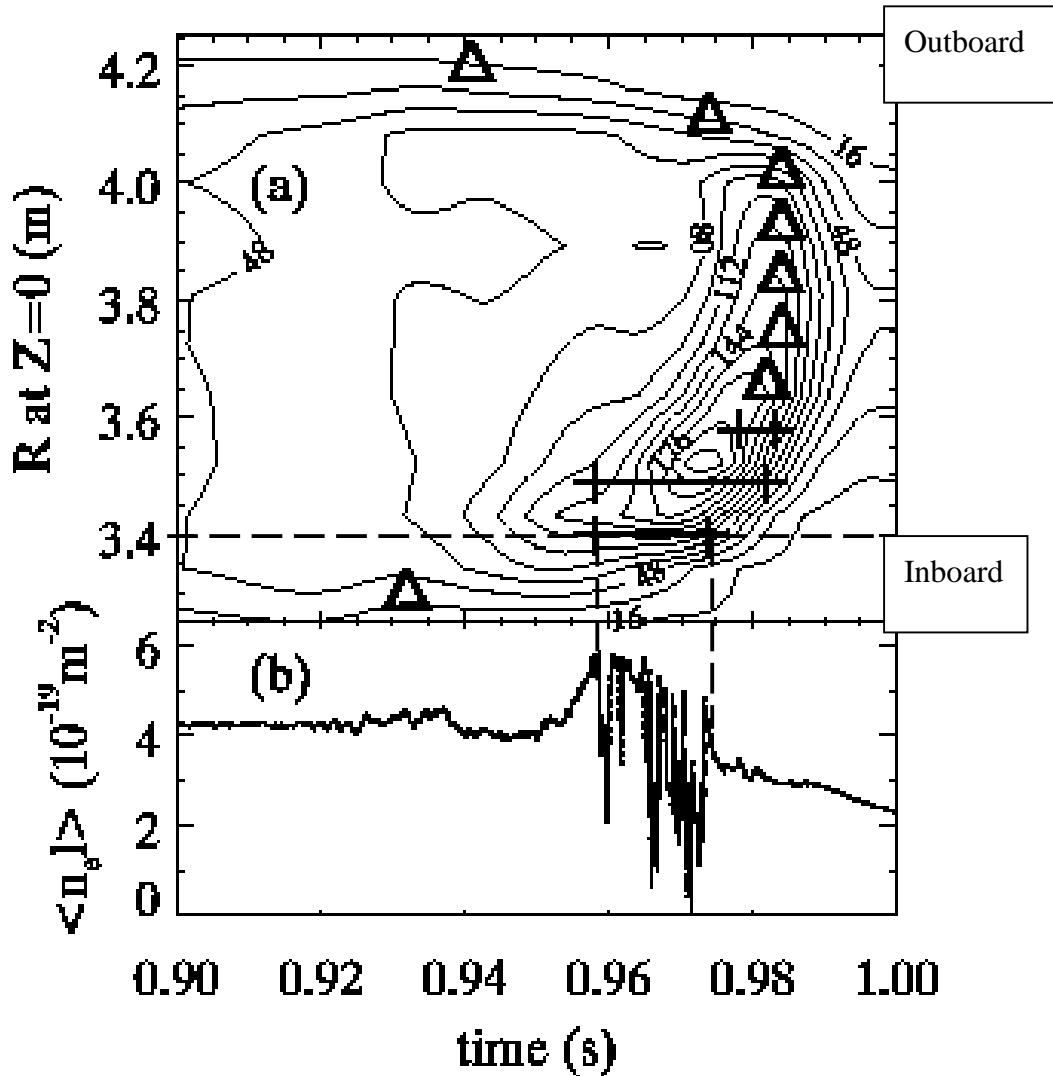
Fig. 5.2.3 The Comparison of the brightness profile evolution by the resistive bolometer as a counter plot and the FIR interferometer for the LHD shot #3574. The peak in FIR line densities are shown in with triangles. The periods of signal degradation for three of the inboard FIR channels are shown as two plus signs. (b) Line density evolution for the FIR interferometer at $R = 3.4$ m (inboard side) [31].

5.3 Images of asymmetric radiation collapse

5.3.1 Shot summary for a typical discharge terminated by radiation collapse

Figure 5.3.1 shows a discharge summary for LHD shot #28961. Two neutral beams (NB) were injected during the interval 0.30 s - 2.30 s and the electron density was increased by hydrogen gas puffing as shown in Fig. 5.3.1 (b). After 2.0 s the plasma develops a thermal instability leading to a sharp drop in the stored energy (Fig. 5.3.1) and rapid increase in the radiated power (Fig. 5.3.1(b)) and spectroscopic signals from CIII and OV (Fig. 5.3.1 (d)) and the plasma was terminated at about 2.10 s by radiative collapse. The timing of these signals is synchronized to within better than 1 ms by using the common LHD trigger.

Figure 5.3.2(a) shows the total radiation power data by the same wide-angle bolometer as Fig. 5.3.1(c) with a sampling frequency of 1 kHz using the LHD trigger. Using this data, the timing of the highest radiated power is 2.162 s.

The contour plot of radiation emissivity profiles from the resistive bolometer arrays at a lower port viewing a vertically elongated cross-section is shown in Fig. 5.3.2(b) which is inverted using the magnetic geometry in terms of ρ. The value $\rho = 0$ corresponds to the magnetic axis and plus ρ is the outboard side, the minus ρ is the inboard side. This contour plot has a 10 ms time resolution, so the collapse time for this data is 2.16 s but this order is sufficient since the frame rates of the IR cameras are slower than 100 Hz. At 2.00 s ("A"), the radiation power has a symmetric structure and after 2.10 s, an asymmetric pattern was observed ("B" and "C"). Around 2.16 s at the collapse timing, the radiation power density was strongest and observed the most localized asymmetric radiation spot "D" on the inboard side. During the radiation collapse, the asymmetric radiation spot was maintained for 30 ms and the radiation power decreased quickly thereafter.

5.3.2 Images of both cameras

5.3.2.1 Tangentially viewing IRVB

First of all, the frame with the radiation collapse has to be found by the localized structure and the highest radiation power density. The localized radiation structure during the collapse is already shown in Fig. 4.1.3(b) but the width and the position on the data are different for each shot, and the FOV was changed from the 4th LHD campaign in Sep. 2000- Feb. 2001 to the 5th campaign in Sep. 2001- Feb. 2002. The highest power density sometimes is due to unabsorbed NBI neutral particles in the afterglow period. The IRVB from the tangential port can measure the strong power from the NBI, but these frames have a very characteristic structure in which only the center is peaked as in frame 39 in Fig. 5.3.3. These NBI frames during the afterglow are excluded from the frames with the highest radiation.

The THV900LW cannot measure a single frame during the radiation collapse period due to a frame rate of only 15 Hz (time resolution of about 67 ms). Using the two-dimensional structure and the highest temperature on the foil for every frame, one frame is chosen as the peak of the collapse. Figure 5.3.3 shows images of the two-dimensional radiation from the tangentially viewing IRVB during the frames numbered 33 to 39 for LHD shot # 28961. The color scale on the right side shows the power density at the foil and a different level is shown for each frame. Using these frames, Frame 37 is determined to contain the collapse data due to the reasons mentioned above.

Frame 38 shows two signals during the afterglow including NBI neutral power "C" and the plasma radiation "B". Frame 39 shows only an afterglow from NBI power "D". The maximum density color " yellow" is shown to be over 50 mW/cm^2 during the above mentioned afterglow. Before the collapse frames, 35 and 36 show hollow profiles similar to Fig. 4.1.3 (a).

5.3.2.2   Upper port IRVB

In Fig. 5.3.4, the top view of the LHD midplane shows the spatial channels of the top viewing IRVB and the FOV of the tangentially viewing IRVB. The black square with mesh is the FOV from the upper port of the IRVB. Three green lines show the FOV from the tangential view of the IRVB

and the two outside lines show the edge of the FOV and the inside one is the center of the FOV. At just the center of the upper port in the toroidal direction, the plasma has a vertically elongated cross-section. Moving toroidally towards the 5-O port side as shown in Fig. 2.3.3 the near, thick ergodic region of the plasma cross-section is rotated towards the outboard side of the vacuum vessel. Moving in the other direction towards the 7-O port as shown in Fig. 2.3.3 the near, thick ergodic region of the plasma cross-section is shifted towards the inboard side of the vacuum vessel. At present, 11(toroidal direction) x 11(major radial direction) channels are formed from the IRVB data after final resampling in the analysis. This channel number of the IRVB on the upper port is considered sufficient due to the NEPD with over $1mW/cm^2$ during a plasma discharge. Some near edge side channels have an FOV that intersects the wall. Additionally area "A" (Fig. 5.3.5) unfortunately is not covered by the tangentially viewing IRVB.

For 11 x 11 channels of the upper port IRVB, each pixel was designated by a toroidal number for the X-axis and a radial number for the Y-axis as shown in Fig. 5.3.5. The toroidal number = 1 is at the 7-O port side as shown in Fig. 2.3.3 and the radial number = 1 is at the inboard side. The plasma continues in the toroidal direction, but channels on toroidal number = 1 and 11 observed negligible radiation that is considered to be incorrect. The reason for these incorrect signals is due to incorrect calibration parameters, these channels are not referred to at present and in the future this problem will be solved using the new calibration parameters derived as described in Sec. 3.1.2.2.

Figure 5.3.6 shows images of the two-dimensional radiation from the upper port IRVB during the frames numbered 131 to 152 for LHD shot # 28961. The camera installed at the upper port is the SC500 with a frame rate of 60 Hz (17 ms). Seeing these frames of data, some different structure is found. From frame 130 to 138, the high radiation region is dispersed in the FOV and the maximum power density is about 6 mW/cm^2. But from frame 139 to 141, the high radiation region broadened and the maximum power density increased to values from 8 to 20 mW/cm^2. Frame 142 shows the hollow high radiation region again and the highest point of the radiation is detected on the inboard

side that is shown by line "A". Then frame 143 shows a clearly different structure from the preceding frames. Only the inboard side observed the high radiation region in an asymmetric structure. Frame 144 shows almost the same structure as frame 143 and the maximum power density is over 30 mW/cm^2, which is also the same. From frame 145, the high radiation region moved towards the bottom of the image and the detected radiation power decreased. Frame 146 shows the start of a separation with a boundary line just at the vertically elongated cross-section of the plasma. Frames 147 and 148 show separated high radiation regions and the maximum of the power density was decreased to the same level as frame 138. Frames 149 and 150 show the afterglow, but this camera did not measure the NBI neutral power, so the detected power was decreasing like the resistive bolometer data in Fig. 5.3.2(a).

For the data of the upper IRVB, the magnetic field calculation is shown in Fig. 5.3.7(a). Each blue point indicates each magnetic field line for R_{ax} = 3.6 m launched in the region around the last closed magnetic surface (ρ = 1). Inside a green square is the FOV of the upper IRVB and the image of the upper IRVB as a hollow profile is shown in Fig. 5.3.7(b). At the upper right indicated by a circle, many blue points were overlapped and at just this point the image shows the high radiation region that is considered good agreement. The other region at the lower side of the image at the outboard side in Fig. 5.3.7 (b) also shows the high radiation region which is considered to be from the thick ergodic region from the upper IRVB as shown in Fig. 5.3.7 (a).

Table 5.3.8 shows the peak radiation signals of frame 143 and 144. Only radial numbers from 8 to 10 are shown due to the channels of the other radial numbers having lower values. The NEPD of the present configuration using the SC500 camera at the upper port is about 680 μW/cm^2 with Δt = 1/60 s, N_{IR} = 64, σ_{IR} = 0.15 in Eq. (3.2.2.2). But in particular, the experimental number is larger than this numerical value. From the resistive bolometer data, the end of the discharge was at 2.298 s (Fig. 5.3.2(a)) which approximately corresponds to the timing at frame 151. Using this frame, the experimental NEPD could be estimated since basically this frame did not measure radiation signals.

Spatial channels near the edge which have the low temperature data from the SC500 camera sometimes have negative values due to the data analysis involving the difference of two small numbers taken during the equalization. Using the other channels, the standard deviation of the NEPD was calculated and this result was about 2 mW/cm^2. In the following, this experimental NEPD is used in this section.

Using the comparison of Fig. 5.3.2(b) and Fig. 5.3.3, the collapse frame should show a strong asymmetric radiation structure on only the inboard side. Using this criterion, frames 143 and 144 fit these conditions.

For next step, the highest radiation channels and their values are considered.

Before more discussion, the information about each spatial channel from the IRVB at the upper port is written as (toroidal number, radial number) = (x, y).

The highest radiation point is data point (8, 9) at frame 143 whose location is the same for frame 144. In frame 143, the highest detected radiation density is about 40.3 mW/cm^2 at point (8, 9) and the second highest one is about 38.3 mW/cm^2 at point (7, 9). The difference of 2.0 mW/cm^2 is not a significant value since this value is the same as the experimental NEPD, that means these two signals are approximately the same signal level for both images. In frame 144, the highest detected radiation density is about 35.1 mW/cm^2 at point (8, 9) and the second one is about 33.8 mW/cm^2 at point (9, 9). Using the comparison of 40.3 mW/cm^2 at point (8, 9) in frame 143 and 35.1 mW/cm^2 at point (8, 9) in frame 144, the difference of 5.2 mW/cm^2 is a significant value, that means the highest signal is at point (8, 9) in frame 143. Using these numbers, it is determined that frame 143 has the nearest timing to the radiation collapse at 2.16 s because this frame has the channel with the highest detected radiation signal and around this point (8, 9) other channels also have high signals.

5.3.3 Timing of both cameras for the LHD relative time

The THV900LW camera uses the LHD trigger but the actual relative time has a delay relative

to the LHD trigger time that is about 200 ms according to a statistical analysis and a jitter that is about 10 ms. The accurate values of this delay time and jitter have not been measured yet.

The SC500 camera does not use the LHD trigger and this camera is controlled manually. This jitter is about 1.0 s.

With respect to the original LHD time data, the relative timings of both cameras are determined using the collapse timing as a reference as shown in Sec. 5.3.2. Figure 5.3.9 shows the timing of both cameras relative to the LHD time. Regarding the CCD data, the delay time and the jitter at 30 Hz are not considered due to lack of information. For the SC500 camera at the upper port, frame 143 is ascribed to the collapse timing. In the THV900LW camera at the tangential port, frame 37 is also ascribed to the collapse timing.

For the actual data both cameras have a delay time and jitter because Fig. 5.3.9 shows only an idealized model. That is to say in Fig. 5.3.9, the relationship between the data of each camera still has a relative uncertainty.

5.3.4   Comparison of the SC500 at 15 Hz and the THV900LW at 15Hz

The original frame rate of the SC500 is 60Hz, but to compare with the THV900LW data the frame rate is changed to 15 Hz by averaging over 4 frames, which is the same frame rate as that of the THV900LW. Figure 5.3.10 shows the images of the two-dimensional radiation from the upper port of the IRVB for LHD shot # 28961 at 15 Hz. The frame numbers in this figure show the original frame numbers in Fig. 5.3.6. For frame number 37 from the tangential port in Fig. 5.3.3, the same timing data from the upper port at 15Hz has four possibilities: "140 –143","141 –144", "142 –145", and "143 –146" since frame 143 is fixed by the collapse timing.

For these possibilities, the comparison of the FOV of the upper port IRVB and the tangential port IRVB is considered. The image of the IRVB from the tangential view during the 5th campaign has 17 x 12 spatial channels and the X-axis is called the horizontal number, Y-axis is called the

vertical and in this section bolometer pixel number is referred to as (the horizontal number, vertical number) = (x, y). On the image of frame 37 from the tangential port, the highest point of the radiation is point (13, 4) and the high radiation region is the rectangle in (11, 5), (15, 5), (11, 2), (15, 2) as shown in Fig. 5.3.12 (a). Figure 5.3.12 (b) shows the cross-section of the spatial channels in the plane of the radial channel number 4 in Fig. 5.3.12 (a) and channels 11 and 15 at the horizontal direction are shown by an arrow as the high radiation region and channel 13 is shown by a blue region as the highest radiation point. In this plane the magnetic flux surfaces have a complicated structure since this plane is not a horizontal cross-section since the FOV of the spatial channels look down to the plasma from the foil of the IRVB.

Due to the limited FOV of the tangential IRVB as shown in Fig. 5.3.4, the tangential FOV on the spatial channels of the upper IRVB having a high radiation region is limited to toroidal channels around numbers 1-5 at the inboard side of the upper port IRVB FOV. For this reason, it is considered that the high radiation region of frame 37 of the tangential IRVB corresponds to the high radiation region around toroidal channel numbers 1-5 at the inboard of the upper port IRVB FOV. Frames "140 –143" and "141 –144" observed high radiation as the total absorbed power but the high radiation region was localized on the 5-O side of the FOV as shown in Fig. 5.3.10, therefore these frames are considered to not correspond to the frame 37 of the tangential IRVB. Using this consideration only two possibilities, "142 –145" and "143 –146" remain.

Table 5.3.12 shows the peak radiation signals of frames "142 –145" and "143 –146". Both frames show an asymmetric radiation structure at only the inboard side and the high radiation belt is spread widely along the wall as shown in Fig. 5.3.10.

The highest radiation point is data point (8, 9) at frame "142 –145" whose location is the same for frame "143 –146". In frame "142 –145", the highest detected radiation density is about 28.0 mW/cm^2 at point (8, 9) and the second one is about 26.9 mW/cm^2 at point (7, 9). The difference of 1.1 mW/cm^2 is not a significant value considering the experimental NEPD of 2.0 mW/cm^2. That

means that both pixels have approximately the same signal level. In frame "143 –146", the highest detected radiation density is about 25.3 mW/cm^2 at point (8, 9) and the second one is about 24.3 mW/cm^2 at point (7, 9). Using the comparison of 28.0 mW/cm^2 at point (8, 9) in frame "142 –145" and 25.3 mW/cm^2 at point (8, 9) in frame "143 –146", the difference of 2.7 mW/cm^2 is a significant value which means that frame "142 –145" has the highest signal level, so frame "142 –145" was determined to be the best frame for the comparison with tangential frame 37 during the radiation collapse. In addition, the channels with over 20 mW/cm^2 of radiation power density are shown in bold print as a high radiation region as shown in Table 5.3.12.

By determining that frame "142 –145" from the upper port is fixed to frame 37 from the tangential port, a forward frame "138 –141" can be considered to be fixed to the frame 36 from the tangential port. Seeing frame "138 –141" as shown in Fig. 5.3.10, this image shows a wide high radiation region that has a symmetric radiation structure. The forward frame 36 of the tangential IRVB also shows a symmetric radiation structure. Therefore by using frame "142 –145" as a time reference the changing structure story of the radiation collapse can be examined.

This high radiation region from the upper port IRVB using frame "142 –145" and from the tangential IRVB using frame 37 is shown in Fig. 5.3.13 as the magnified cross-section of the spatial channels using Fig. 5.3.11(b). The squares with a blue mesh are the high radiation region from the upper port and the green mesh shows the high radiation region of the tangential IRVB from ch.11 to ch.15 and the blue chord is the highest radiation channel ch.13 of the horizontal channels. In addition, the vertical cross-section of the tangential IRVB is shown in Fig. 5.3.14. Each FOV is shown by as a blue line and the extent of the high radiation region on the vertical channel 4 from the tangential IRVB is shown by the red ellipse. At near the inboard wall, this FOV is located under the midplane which is original information from the IRVB data.

For the high radiation region and the highest radiation point as shown in Fig. 5.3.11, the image of the three-dimensional position is shown in Fig. 5.3.15 with the two different boxes.

116

Each region is shown in Fig. 5.3.16 in a view with the last closed magnetic surface and the ergodic surface from the outside port of LHD. Figure 5.3.15(a) shows the left side (7-O side as shown in Fig. 5.3.11) edge of the high radiation region, Fig. 5.3.15(b) shows the out side of the left edge of the highest radiation region (as viewed from the outer side of the torus as seen in Fig. 5.3.16) and the Fig. 5.3.15(c) shows the center of the highest radiation region.

5.3.5 Toroidal and poloidal variation of radiation distribution by IRVB images

Compared to the data of the resistive bolometer, the data of the IRVB can show much more information with the two-dimensional FOV. Figure 5.3.17 shows the comparison of the radial profile of the IRVB and the resistive bolometer on the center FOV of the IRVB. The brightness image of the upper port IRVB is shown in Fig. 5.3.17(a) for the case of a hollow profile with frame 139 at $t = 2.09$ s. At just the center of this FOV, the resistive bolometer array was installed from the lower port and this brightness data is shown in Fig. 5.3.17(c). The brightness data of the resistive bolometer is the detected line-averaged radiation power and using this data the emissivity data is made by means of a tomographic inversion as shown in Fig. 5.3.2(a). Figure 5.3.17(b) shows the radial brightness profile by the IRVB from the same FOV as the resistive bolometer corresponding the toroidal number 6 at $t = 2.09$ s. From these example profiles, the two results using the different two bolometer types show a good agreement.

The images of the IRVB can also show the other radial profiles and the toroidal variation. Figure 5.3.18 shows frame "142-145" during the radiation collapse and Fig. 5.3.18(b) shows the other radial profiles on the toroidal number 3 and 8. From these profiles the full width at half maximum (FWHM) of high radiation regions of the IRVB can be determined. From the spatial resolution of one channel at the midplane of about 11 cm, the FWHM at toroidal number 3 is about 15 cm and at the toroidal number 8 is about 20 cm. The profile of the toroidal variation of frame "142-145" at the toroidal number 10 is also shown in Fig. 5.3.18(c). Due to the lack of a calibration

for the upper port IRVB, in particular the edge channels of the toroidal number 1 and 11 are suspect. Considering that the experimental NEPD is about 2 mW/cm^2, the right side on this image around the toroidal number 8 is higher than the left side around the toroidal number 2.

For the tangential IRVB, the FWHM of the high radiation region on the image was calculated. Figure 5.3.19(a) shows the image of the tangential IRVB frame 37 during the radiation collapse. Centered on the center of the highest radiation point (13,4) as shown in Fig. 5.3.11, the vertical profile at the horizontal number 13 as shown in Fig. 5.3.19 (b) and the horizontal profile at the vertical number 4 are shown. As the fitting analysis, $y = a \cdot x^b \exp(c \cdot x)$ was used, where x is the vertical or horizontal number, y is the power density and a, b, c are fitting parameters. For Fig. 5.3.18 this analysis could not be used due to difficult profiles. The spatial resolution of the tangential IRVB near the FOV of the upper port IRVB is about 9 cm for each direction. Using this number of 9 cm, the FWHMs of the high radiation region from the tangentially viewing IRVB are 18 cm on the vertical profile and 19 cm on the horizontal profile.

5.3.6 Result of horizontally elongated plasma radiation by AXUV diode

Figure 3.5.20 shows the AXUV diode system with two arrays for the horizontally elongated plasma for discharge #28961 at Port 8-O in LHD as shown in Fig. 2.3.3. The differential FOV of each spatial channel with the vertical cross-section are shown in Fig. 5.3.20(a). The black channels are the upper array with 16 channels and the red ones are the lower array with 19 channels. Prior to the radiation collapse at $t = 2.095$ s, the two arrays measured the hollow radiation profile as a wide high radiation region in the FOV as shown in Fig. 5.3.20(b). The high radiation channels are indicated as thin arrows in Fig. 5.3.20(a). During the radiation collapse at $t = 2.162$ s, the two arrays measured different radiation profiles from $t = 2.095$ s as shown in Fig. 5.3.20(c). The channels of the detected high radiation region were only from the midplane to the bottom side from ch.5 to ch.10 of the upper array and from ch.23 to ch.30 of the lower array which is also indicated by thick

arrows in Fig. 5.3.20(a). This result is similar to Fig. 5.2.1(b) in Ref. 31. But based only on these data as shown in Fig. 5.3.20, the position of the high radiation region was not determined and the full two-dimensional characteristics of asymmetric radiation collapse at the horizontally elongated cross-section are not understood at present.
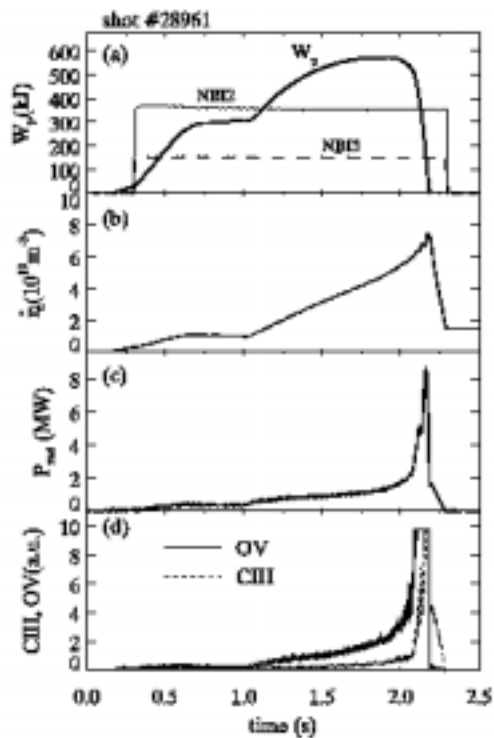
Fig. 5.3.1 Discharge summary for LHD shot #28961 with (a) stored energy from diamagnetic measurements and NBI (#2 and #3) timing, (b) line- averaged electron density, total plasma radiated power from resistive bolometers and (d) spectroscopic signals from CIII and OV

**shot 28961 Power Density at Port 6.5**

(b)
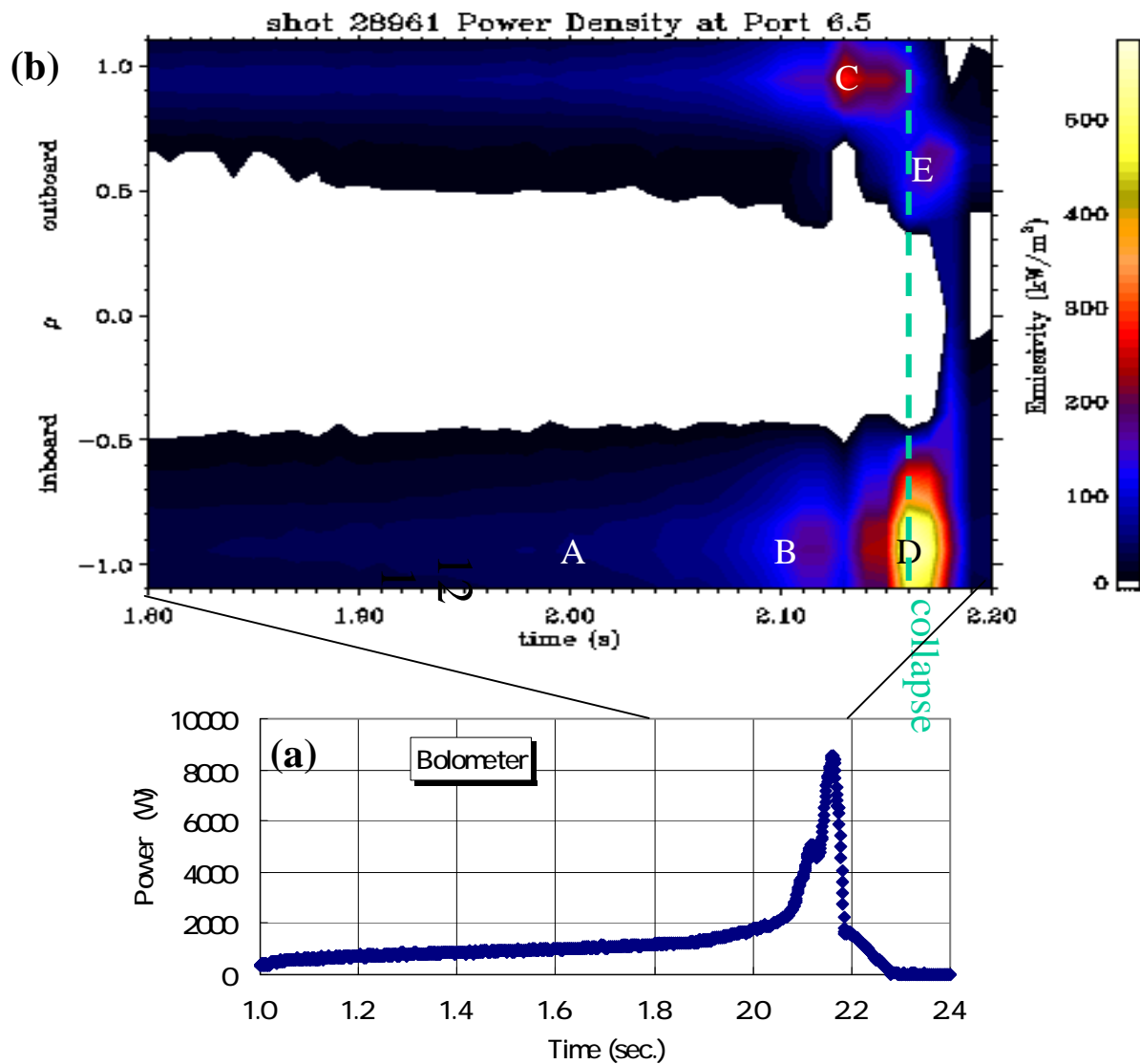
(a) Bolometer

Fig. 5.3.2 (a) The resistive bolometer at 3-O and (b) the contour plot of the radiation emissivity profiles from the 6.5L arrays. (Figure (b) courtesy by Y. Xu)
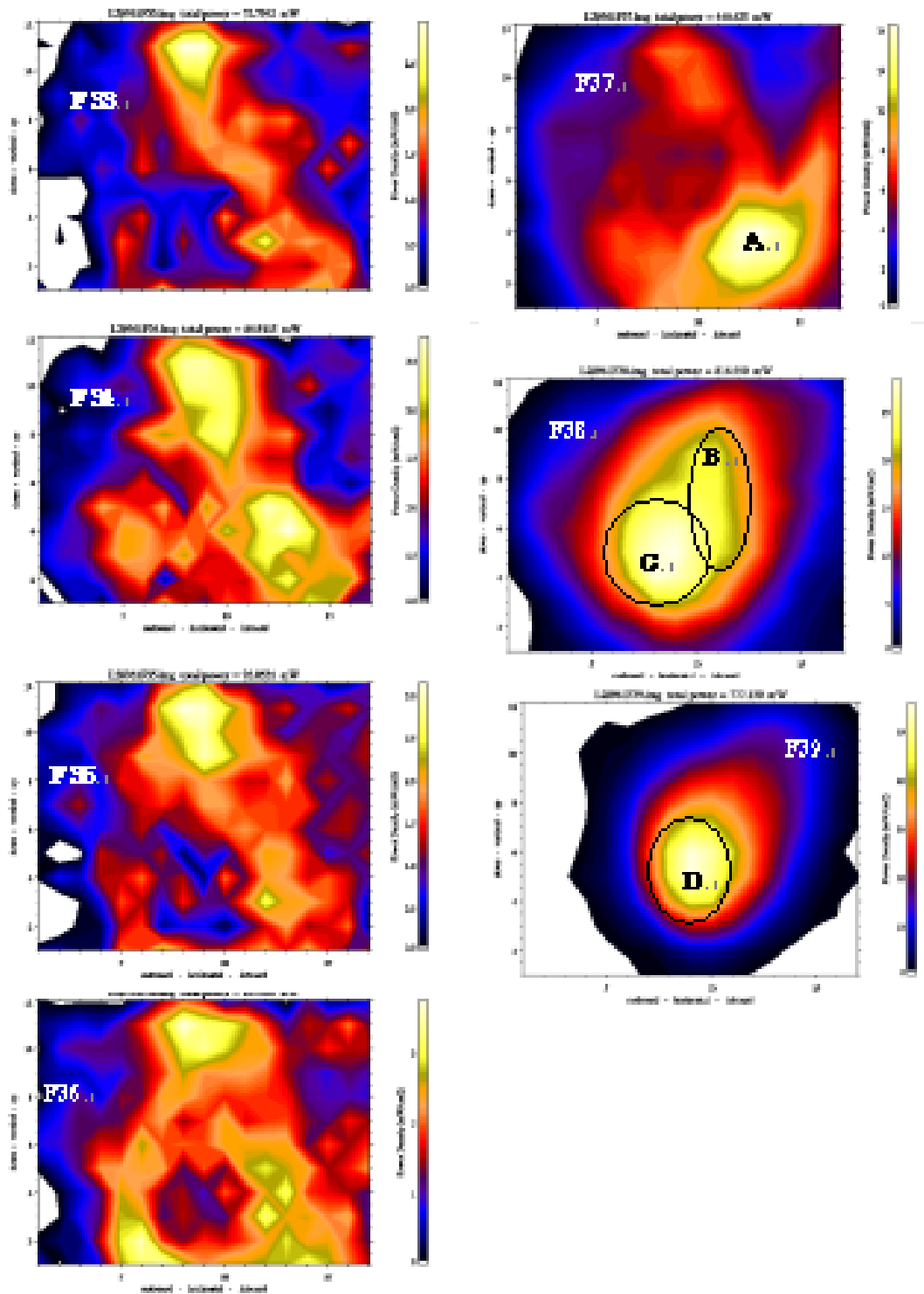
Fig. 5.3.3 Images of the two-dimensional radiation from the tangentially viewing IRVB for LHD shot # 28961.
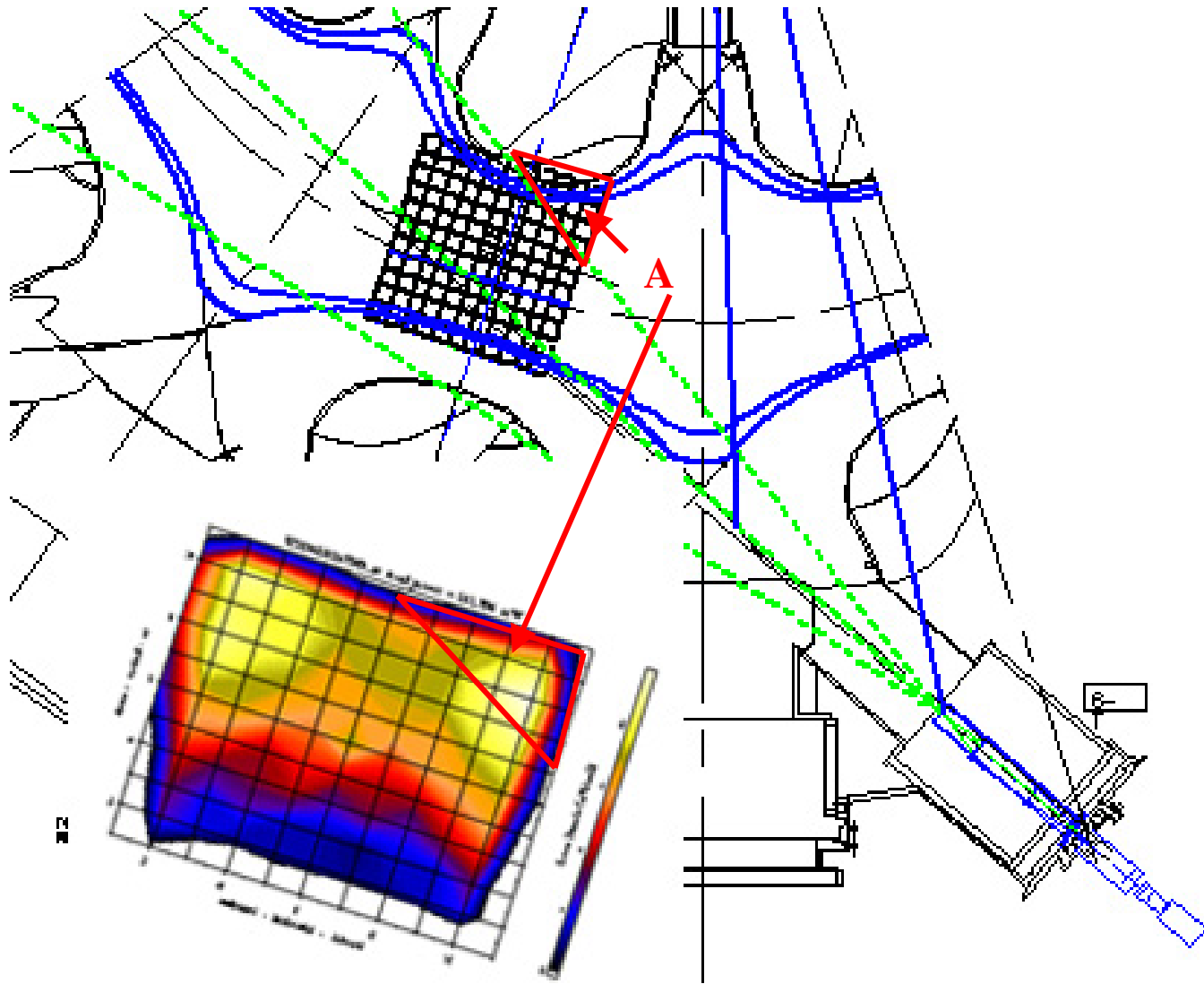
Fig. 5.3.4 The FOV from the upper port and the tangentially viewing IRVB. The red region is not seen from the tangentially viewing of IRVB.
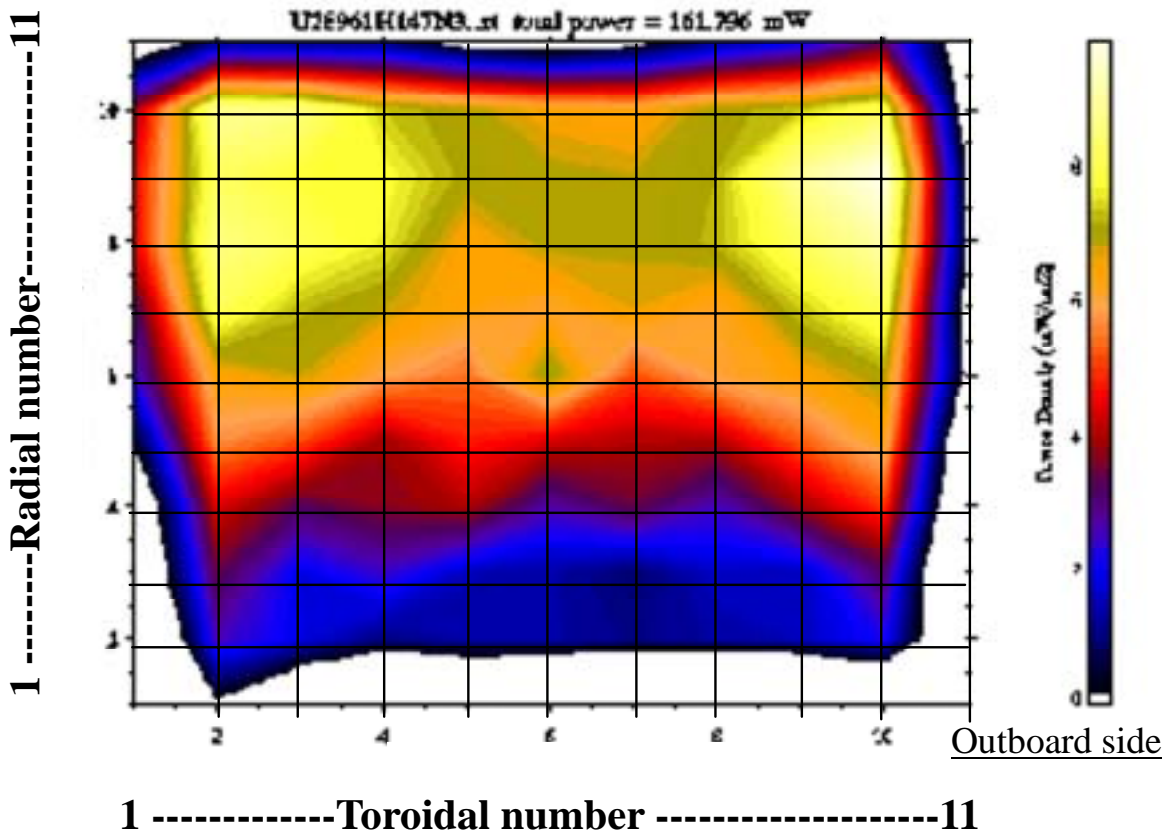
Fig. 5.3.5 Image of the two-dimensional radiation from the upper port IRVB frame 147 for LHD shot # 28961 at 60 Hz.
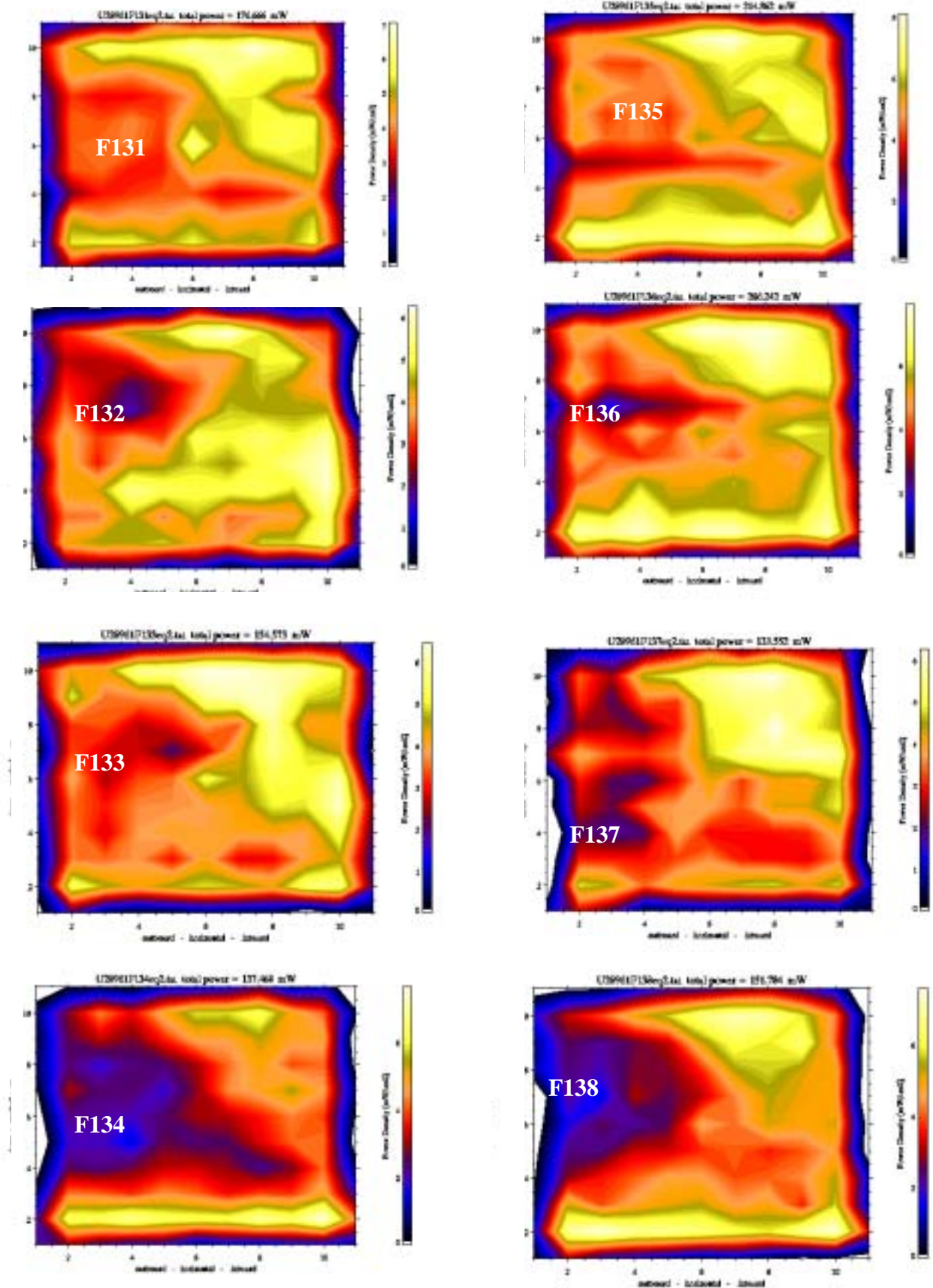
Fig. 5.3.6 Images of the two-dimensional radiation from the upper port IRVB during frame number 131 to 152 for LHD shot # 28961 at 60 Hz (1/3).
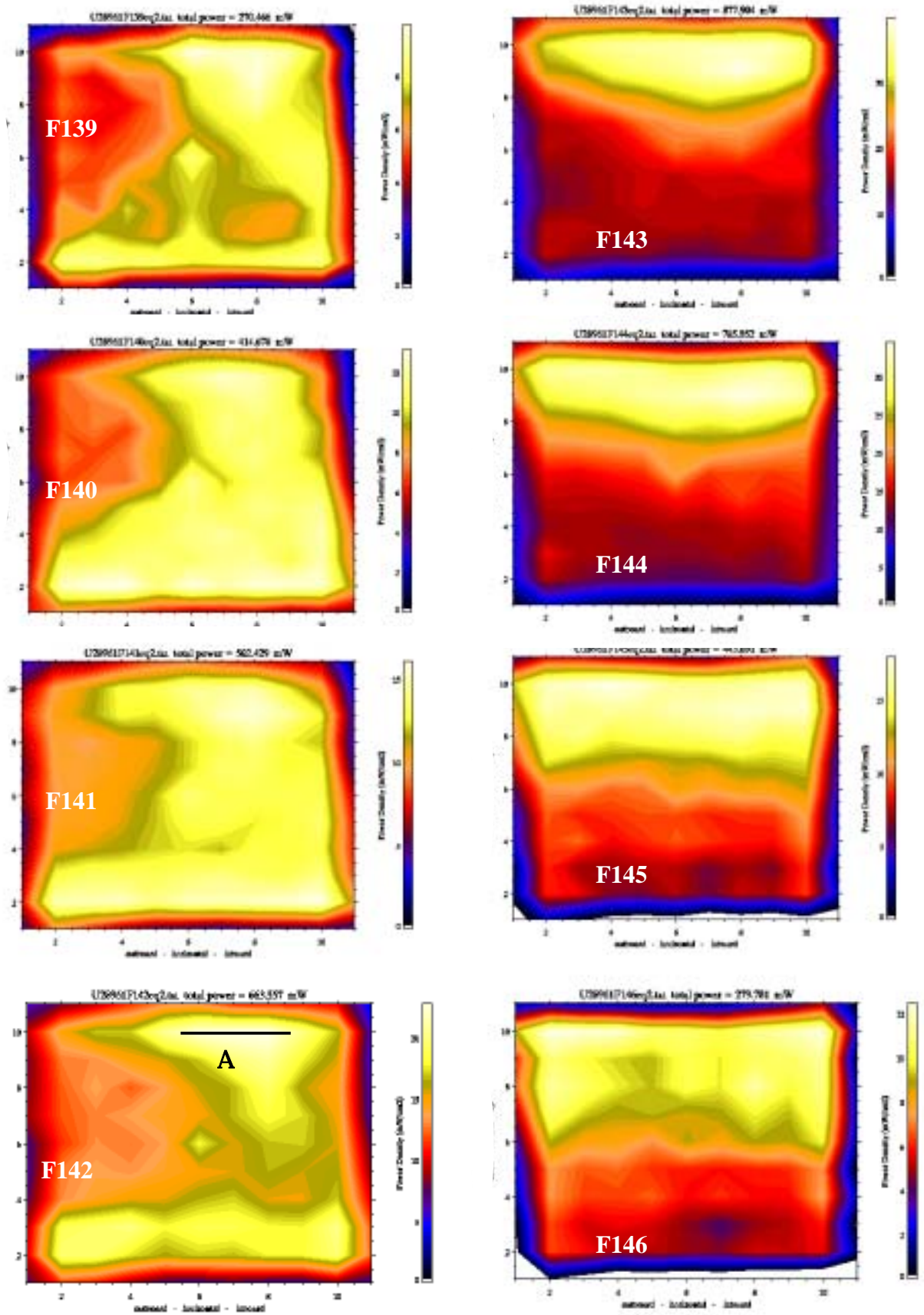
Fig. 5.3.6 Images of the two-dimensional radiation from the upper port IRVB during frame number 131 to 152 for LHD shot # 28961 at 60 Hz (2/3).
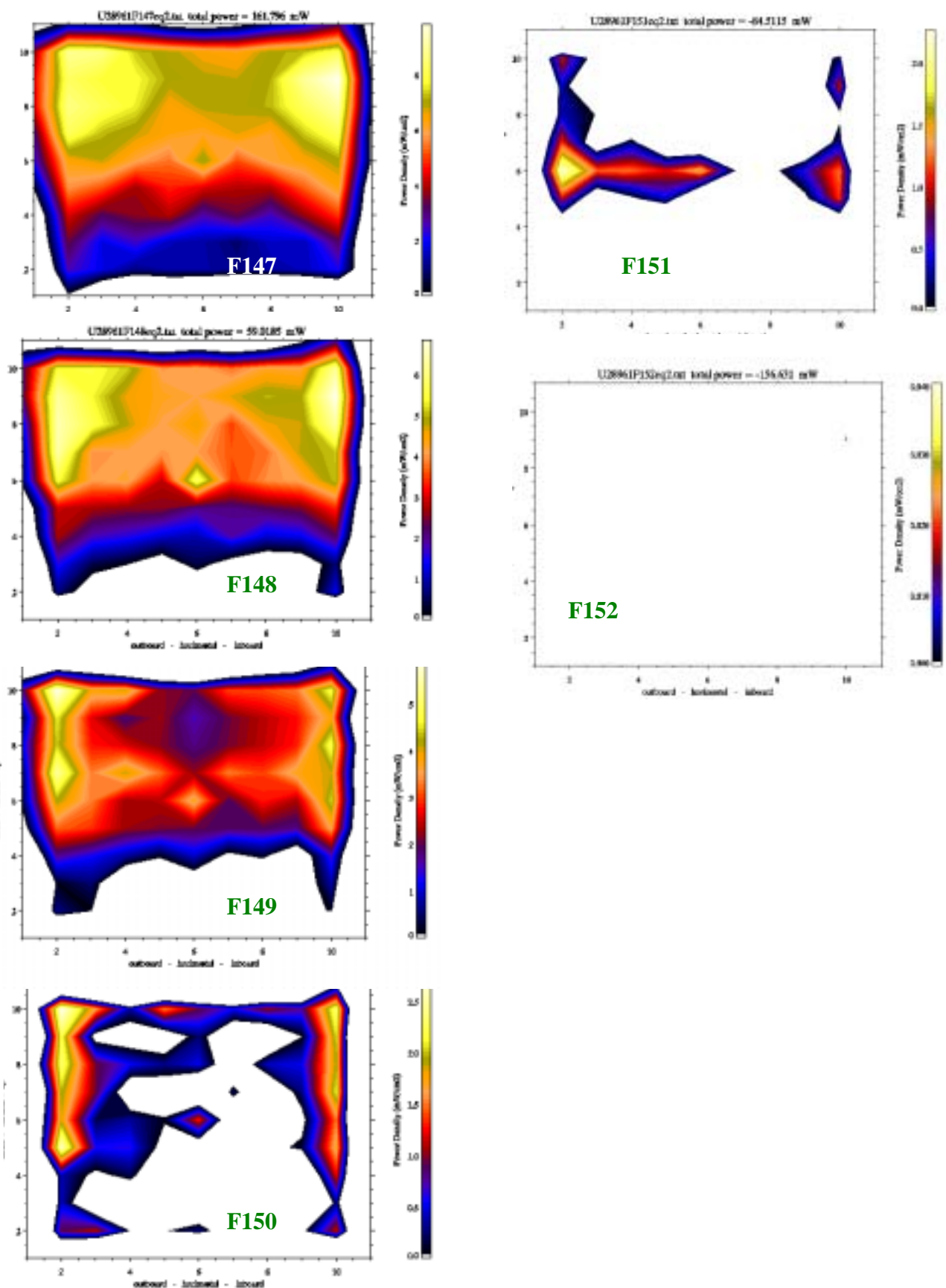
Fig. 5.3.6 Images of the two-dimensional radiation from the upper port IRVB during frame number 131 to 152 for LHD shot # 28961 at 60 Hz (3/3).

(a)

inboard

Outboard

(b)

Inboard

Outboard
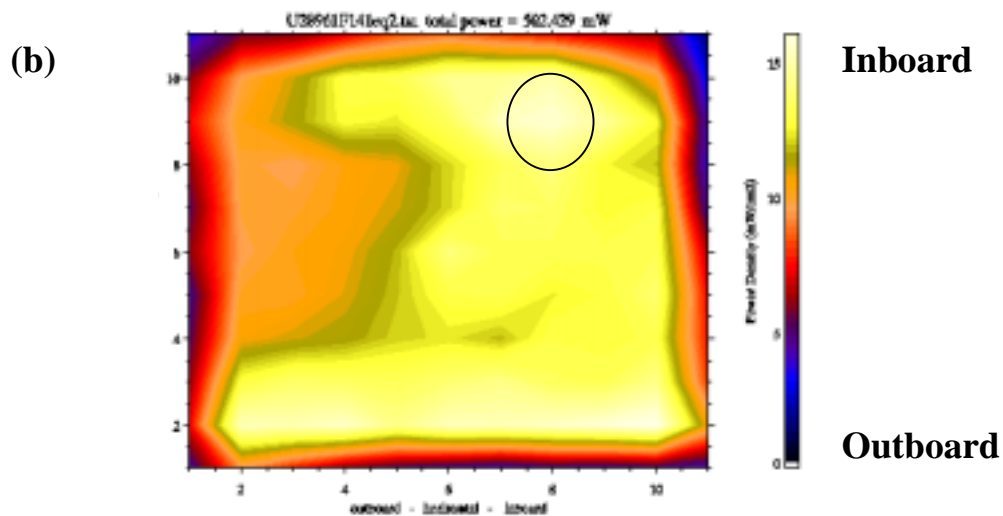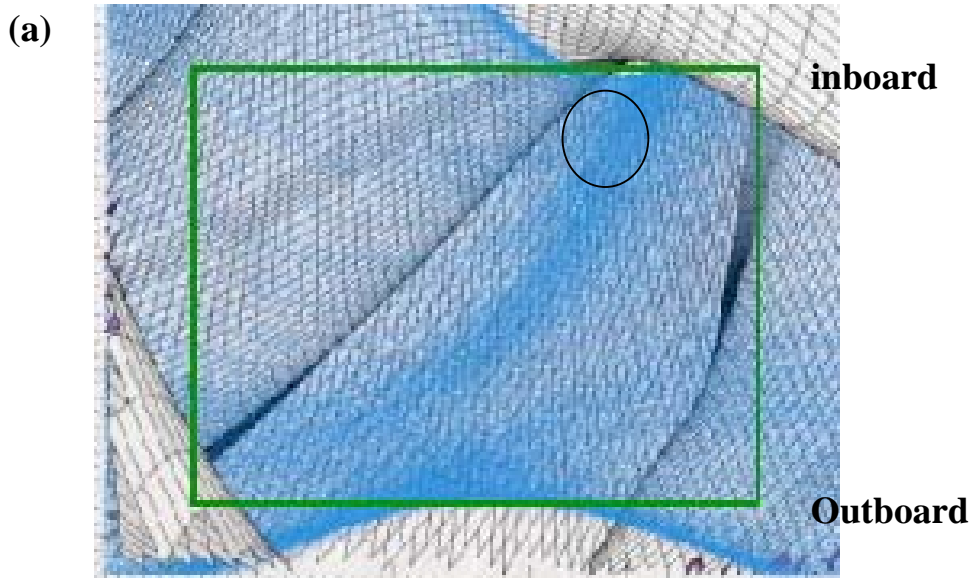
Fig. 5.3.7 (a)the magnetic field calculation in which each blue point indicates each magnetic field line for R_{ax} = 3.6 m launched in the region around the last closed magnetic surface (ρ = 1). Inside the green line is the FOV of the upper port IRVB [34]. (b) the image of a hollow profile by the upper IRVB.

Table 5.3.8   The peak radiation signal during the collapse at the upper port for frames 143 and 144

| Toroidal number	Radial number	mW/cm^2	
		F143	F144
1	10	20.4	22.8
2	10	30.6	31.7
3	10	34.2	32.5
4	10	36.2	32.4
5	10	37.0	31.1
6	10	37.3	29.0
7	10	37.7	29.1
8	10	37.8	30.5
9	10	37.9	32.0
10	10	34.0	28.9
11	10	10.0	10.3
1	9	15.8	19.8
2	9	27.7	28.1
3	9	28.7	29.4
4	9	32.4	30.2
5	9	34.4	31.9
6	9	35.6	32.5
7	9	38.3	33.5
8	9	40.3	35.1
9	9	36.4	33.8
10	9	32.0	32.1
11	9	11.5	11.2
1	8	12.7	13.2
2	8	19.4	23.0
3	8	22.8	23.6
4	8	25.8	24.4
5	8	26.7	26.8
6	8	29.4	28.8
7	8	31.4	27.3
8	8	29.8	28.7
9	8	27.8	26.8
10	8	23.8	24.1
11	8	7.9	8.4

CIIII line by CCD at 30Hz		206		209		213		216				
IRVB from Upper port at 60Hz	F138	F139	F140	F141	F142	F143	F144	F145	F146	F147	F148	F149
IRVB from Tan. port at 15Hz	F36				F37				F38			

Collapse

Bolometer

Power (W) — 10000, 8000, 6000, 4000, 2000, 0

Time (sec.) — 1.0 1.2 1.4 1.6 1.8 20 22 24
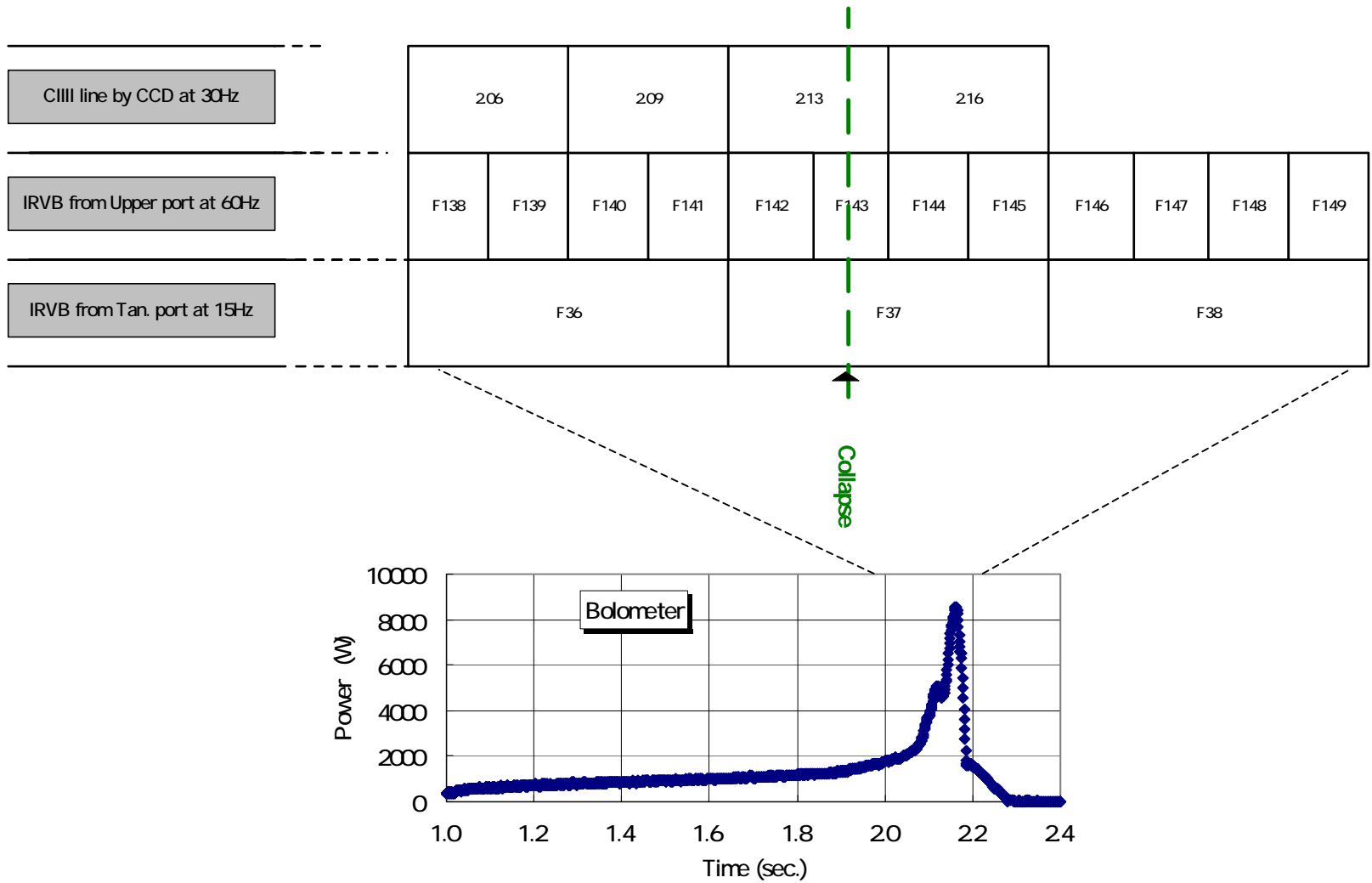
**Fig. 5.3.9 Timing of both cameras relative to LHD timing**
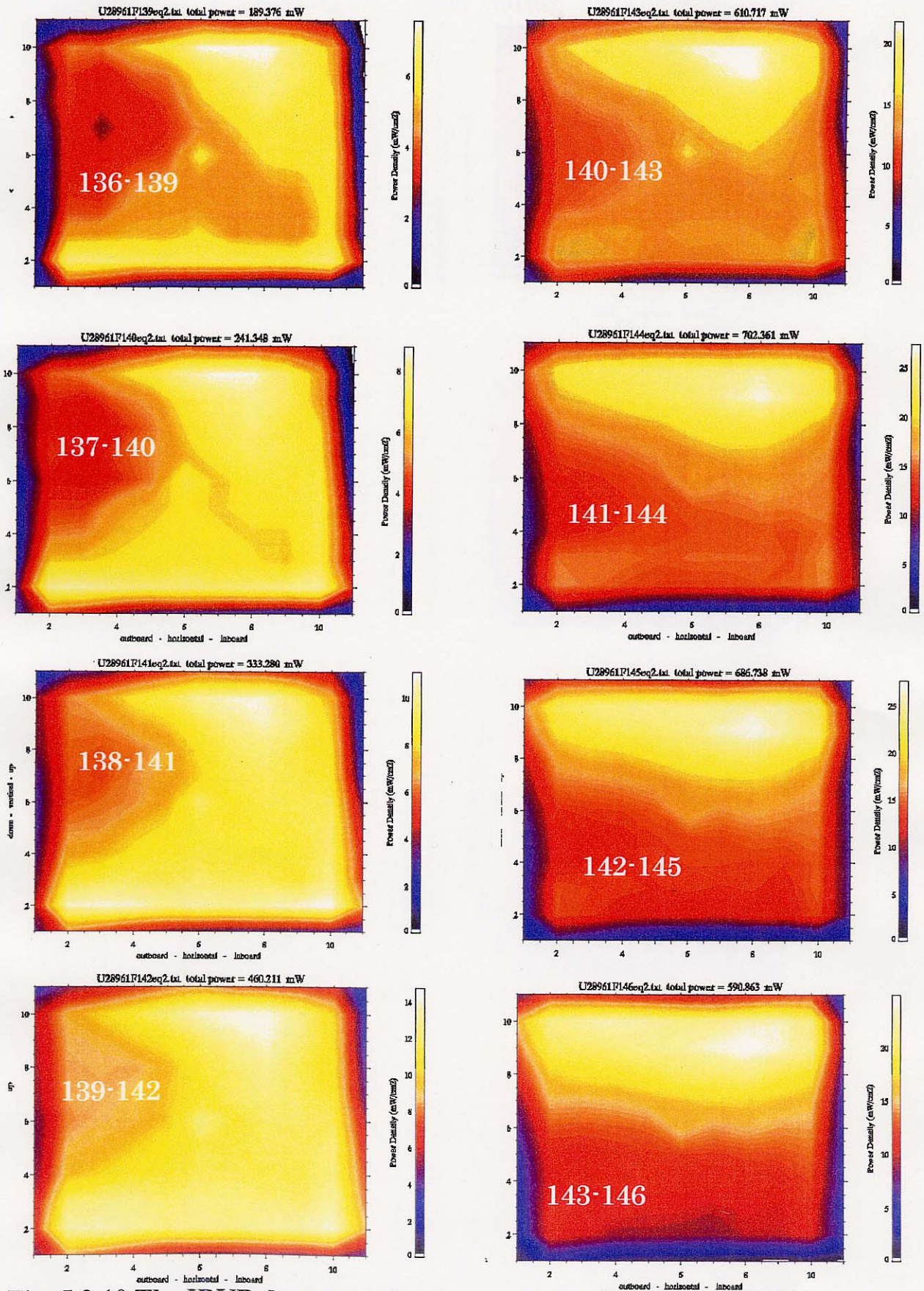
Fig. 5.3.10 The IRVB data from the upper port for LHD shot #28961
at 15 Hz (1/2).
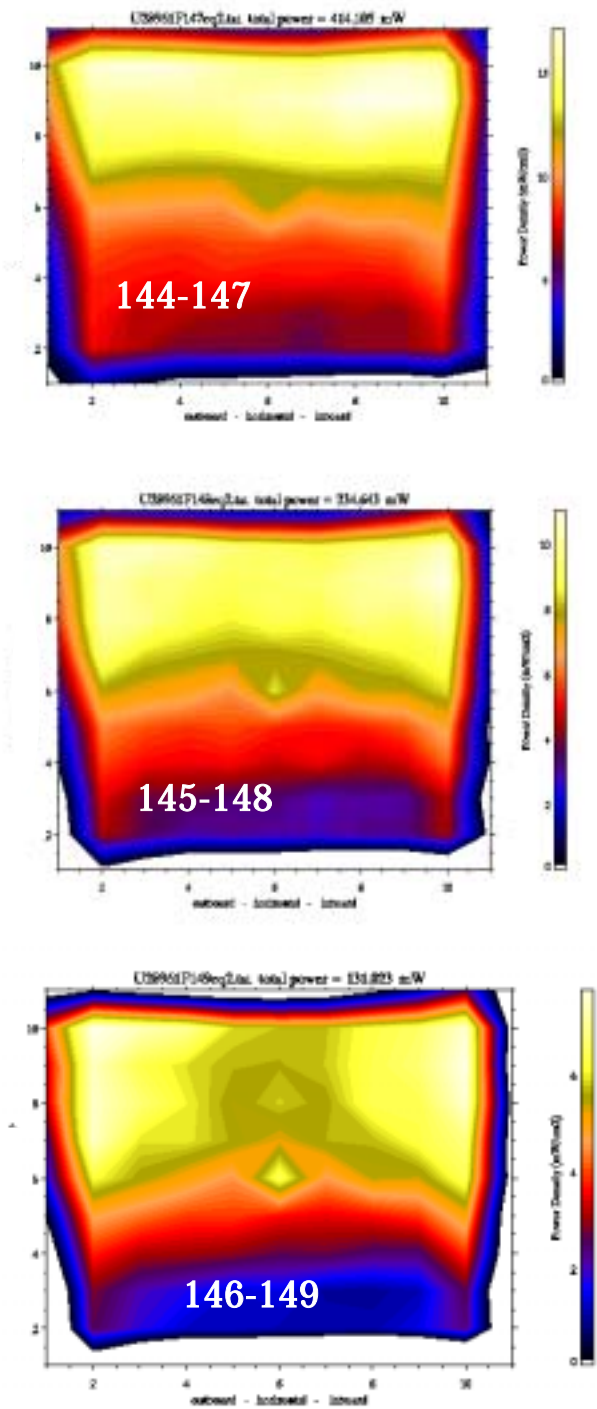
Fig. 5.3.10 The IRVB data from the upper port for LHD shot #28961 at 15 Hz (2/2).

Table 5.3.11 The peak radiation signal during the collapse at the upper port for frames 142-145

| Toroidal number	Radial number	mW/cm^2 142-145	mW/cm^2 143-146
1	10	15.9	15.5
2	10	23.0	22.3
3	10	24.8	23.6
4	10	25.6	24.1
5	10	26.1	23.5
6	10	25.9	23.0
7	10	26.0	22.8
8	10	26.5	23.6
9	10	26.1	24.0
10	10	23.4	22.1
11	10	7.8	7.0
1	9	13.6	12.9
2	9	21.1	20.5
3	9	21.8	20.8
4	9	23.4	22.0
5	9	24.4	22.6
6	9	25.5	23.5
7	9	26.9	24.3
8	9	28.0	25.3
9	9	26.2	24.2
10	9	23.8	22.5
11	9	8.6	7.2
1	8	10.9	10.5
2	8	17.4	17.2
3	8	19	18.2
4	8	19.2	18.5
5	8	20.6	19.4
6	8	22.2	20.8
7	8	22.8	20.9
8	8	23.5	21.6
9	8	21.3	19.7
10	8	19.3	18.4
11	8	7.0	6.0
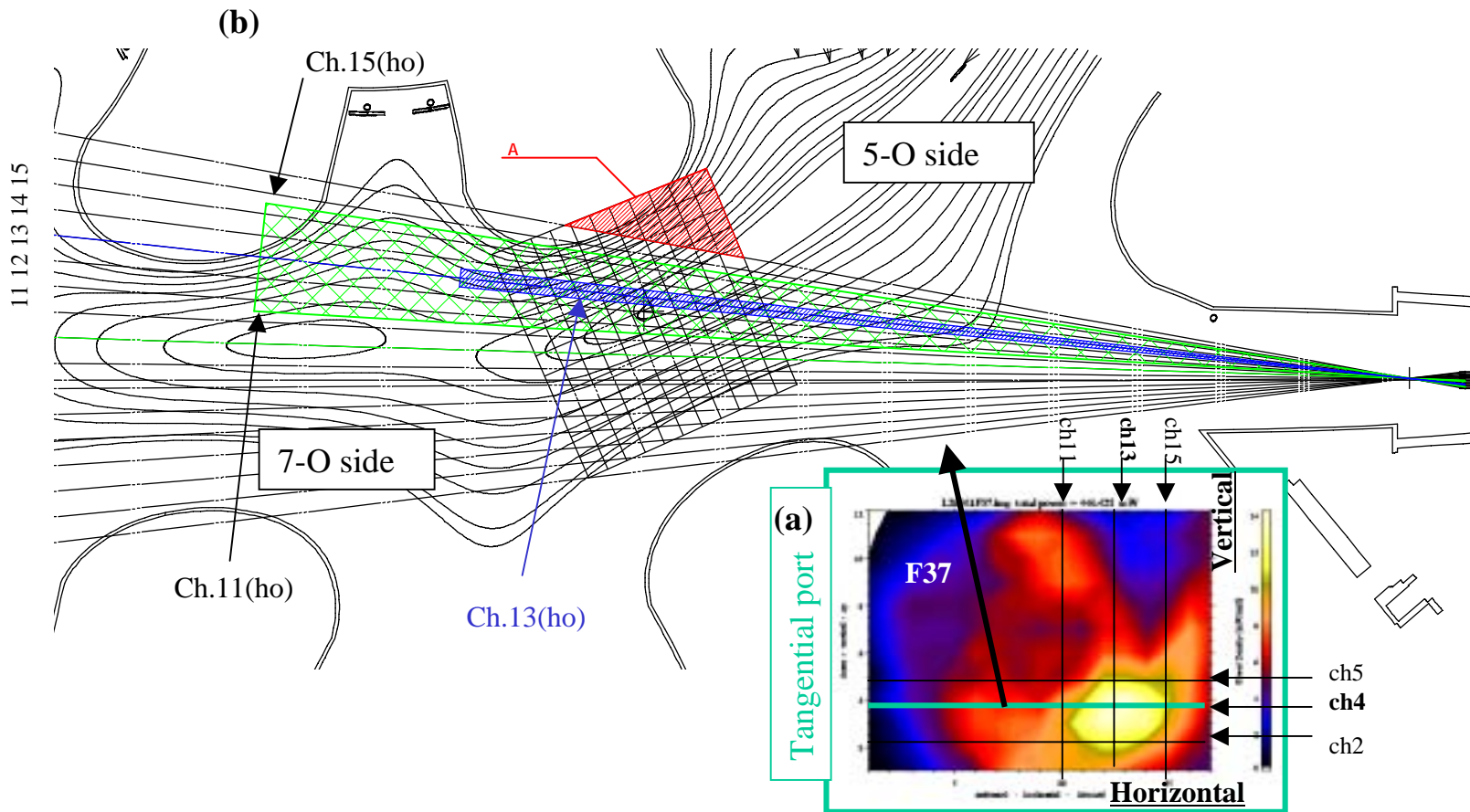
Fig. 5.3.12 (a) Frame 37 of the two-dimensional radiation intensity from the tangentially viewing IRVB and (b) the cross-section of the spatial channels in the plane of the 4th row of the tangentially viewing IRVB. Channels 11 and 15 in the horizontal direction are shown by an arrow and channel 13 is shown by a blue region.
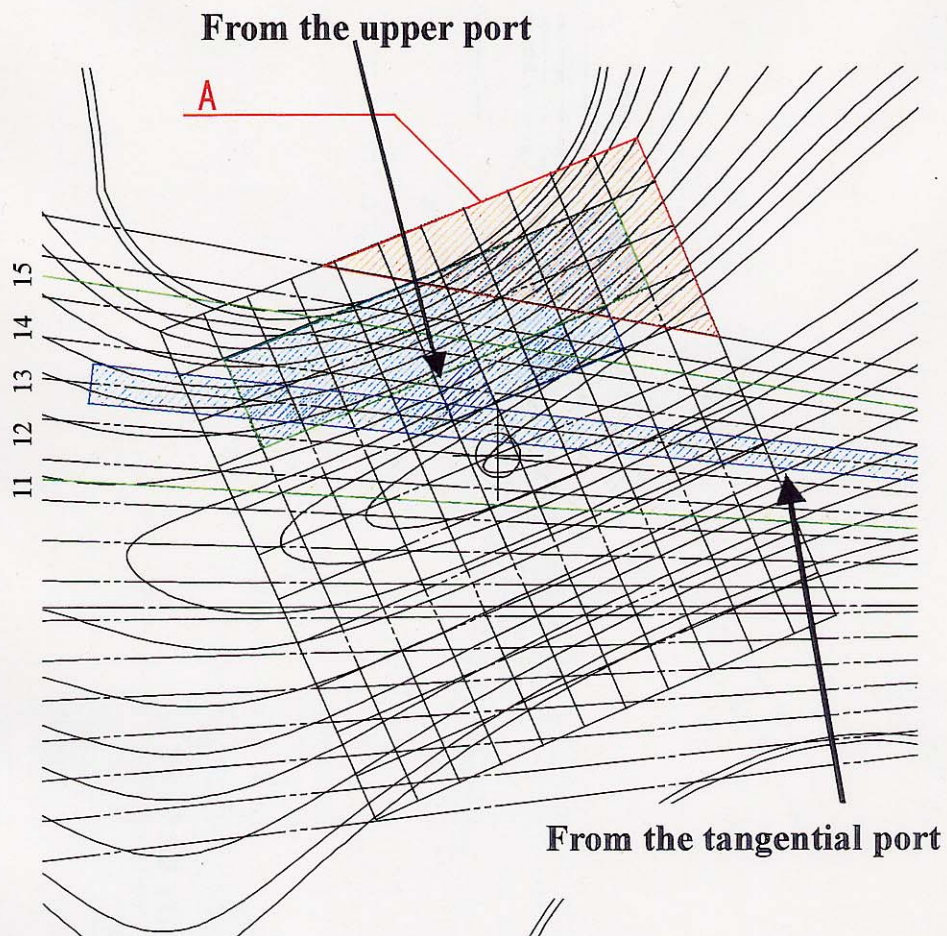
Fig. 5.3.13 Magnified cross-section of the spatial channels in the plane of the 4th row of the tangentially viewing IRVB and the channels of the upper port IRVB. The green mesh shows the high radiation region of the tangential IRVB from ch.11 to ch.15 of the horizontal channels and the blue chord is the highest radiation point at ch.13. For the spatial channels from the upper IRVB, a blue mesh shows the high radiation region.

Upper port

Center of
upper port
IRVB

Upper

IRVB at the tangential port

Midplane

Vacuum
Vessel

Lower

Highest radiation region
on the ch.4 (ver)

Vertical channel 4 of
the tangential IRVB
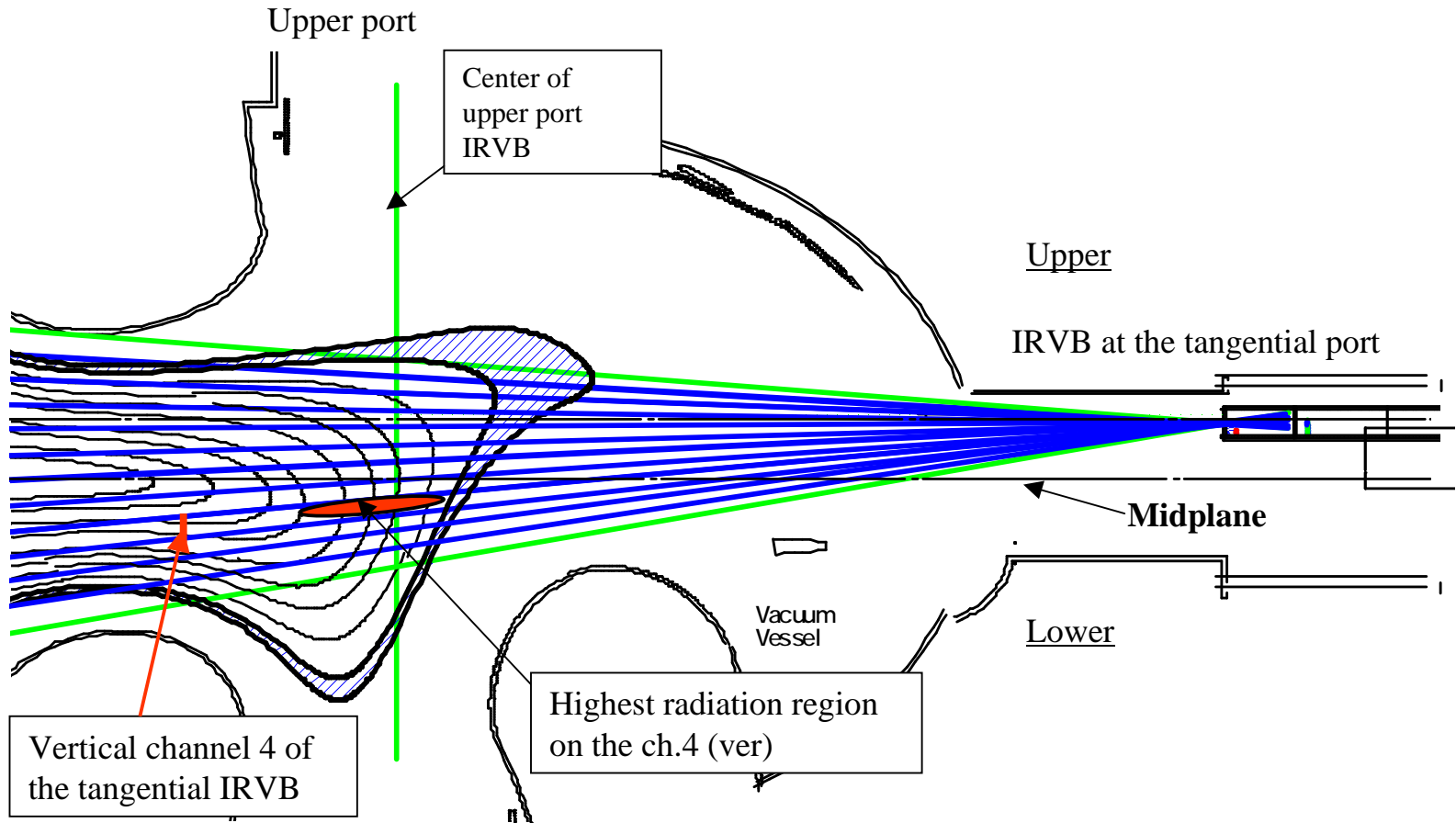
Fig. 5.3.14 The vertical cross-section of the tangential IRVB. The highest radiation region is shown by the red ellipse and the position of the vertical channel 4 near the inboard wall is located under the midplane on the LHD.
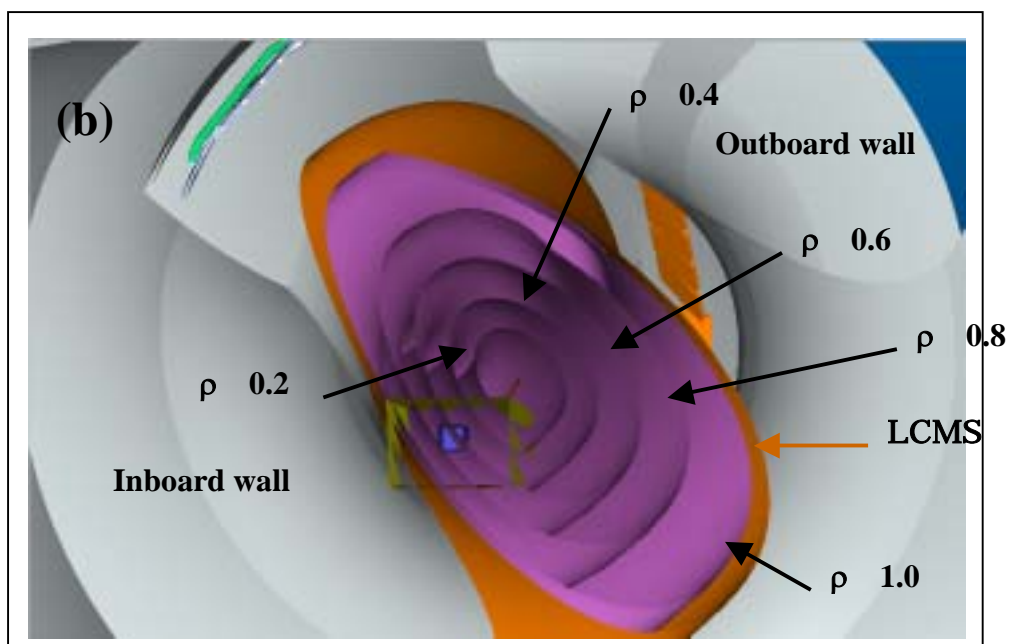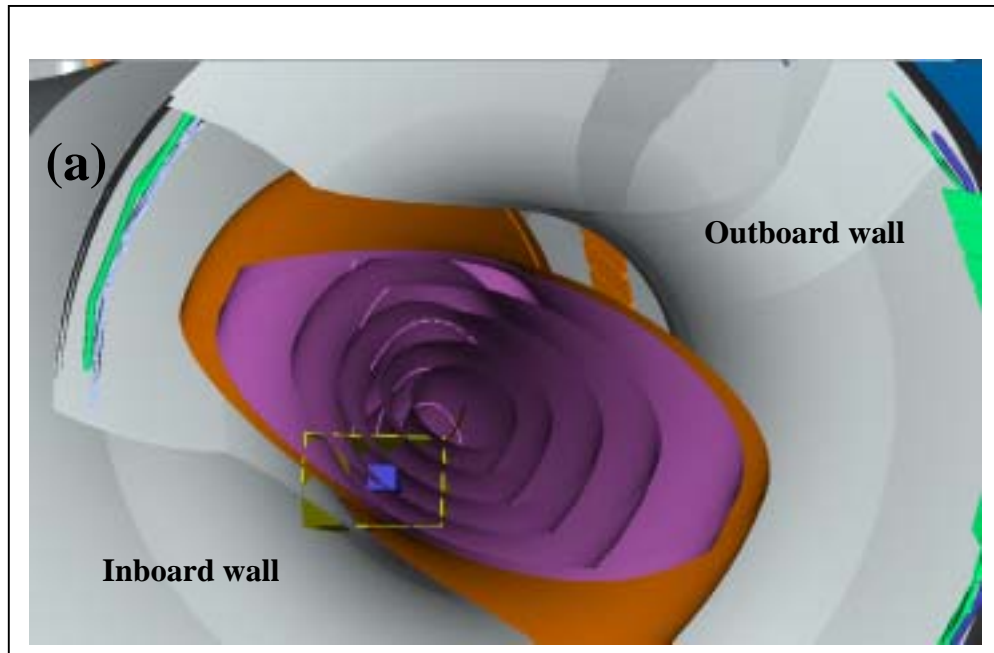
Fig. 5.3.15 Image of the three-dimensional radiation from both IRVBs data (frame 142-145(upper) and frame 37(tangential)) for LHD shot #28961 during the radiation collapse at two different cross sections (a) and (b) with the magnetic surfaces. The small box (blue) shows the highest radiation point and the large box (yellow) shows the high radiation point(1/2) (by H. Kojima).
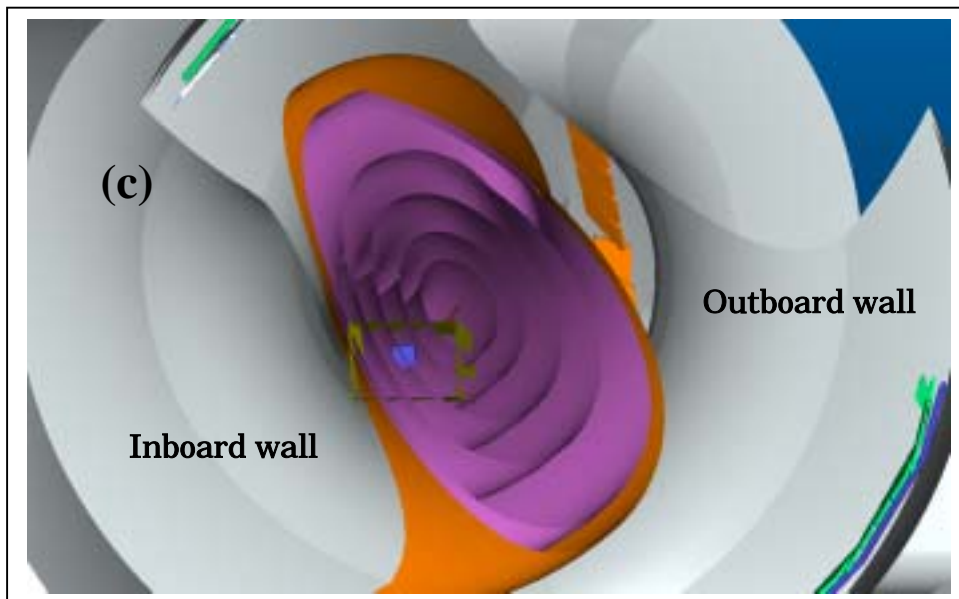
Fig. 5.3.15 Image of the three-dimensional radiation from both IRVBs data (frame 142-145(upper) and frame 37(tangential)) for LHD shot #28961 during the radiation collapse at a different cross section with the magnetic surfaces. The small box (blue) shows the highest radiation point and the large box (yellow) shows the high radiation point (2/2) (by H. Kojima).
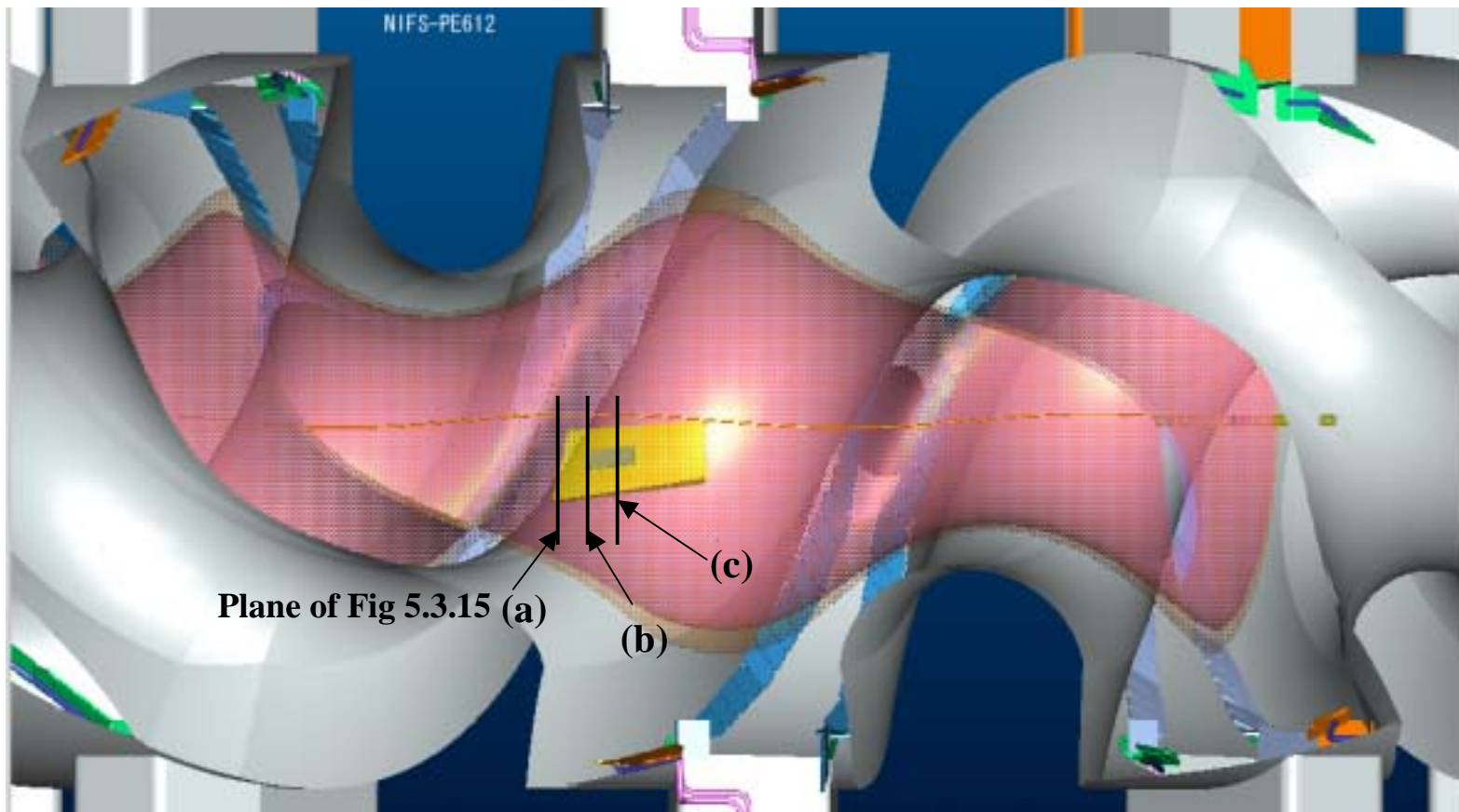
Fig. 5.3.16 The view with the last close magnetic surface (pink) from an outside port in LHD. The small box(blue) shows the highest radiation point and the large box (yellow) shows the high radiation points whose data are from frame 142-145 (upper) and frame 37 (tangential).

(a)

F139

Inboard

FOV of the resistive bolometer

Outboard

(b)

Outboard

Inboard

$t = 2.09s$

Power density (mW/cm^2)

Channel number

(c)

Outboard

Inboard

t=2090ms
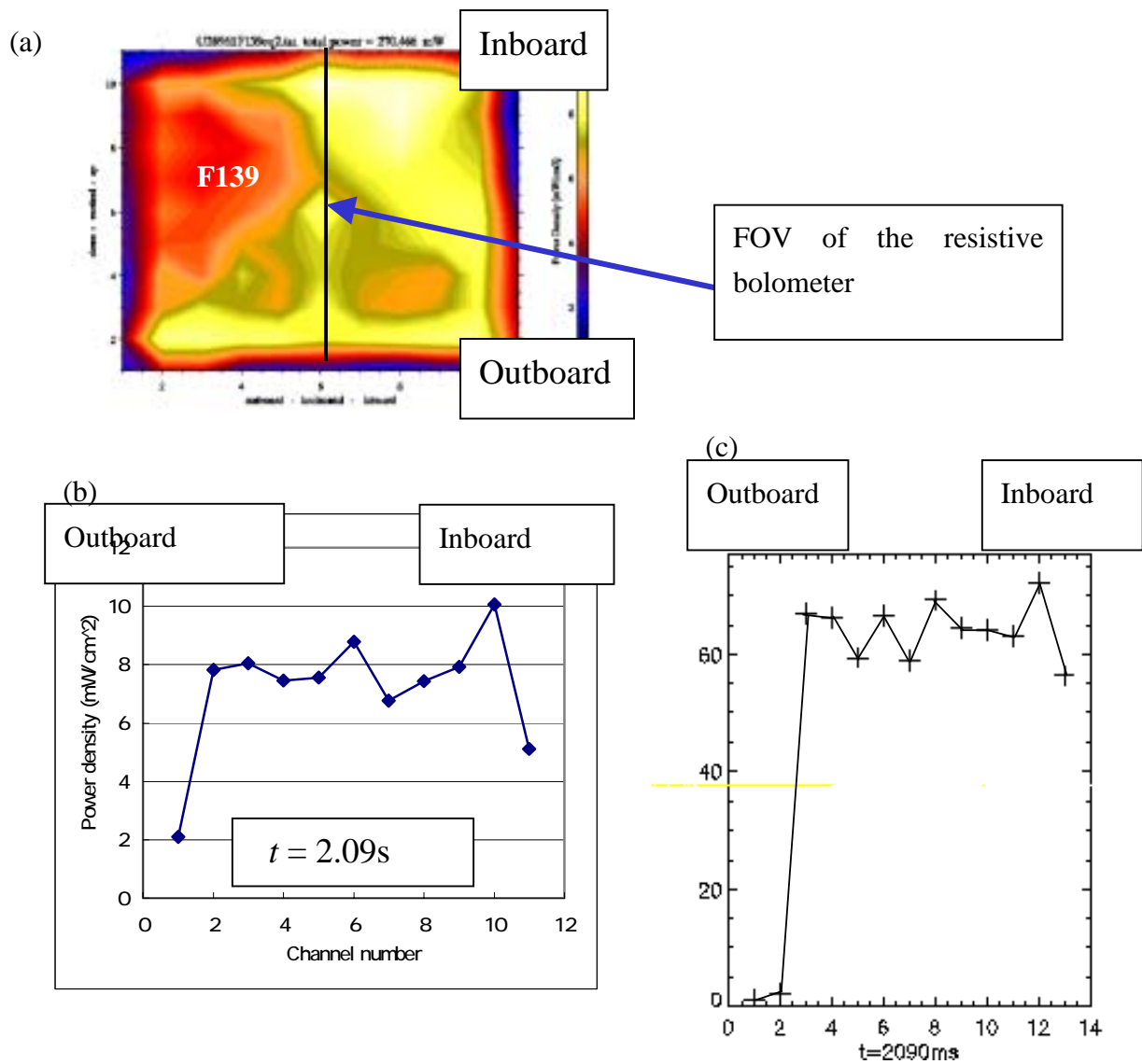
Fig. 5.3.17 The comparison of the radial brightness profiles of the IRVB and the resistive bolometer at the center FOV of the IRVB. (a) the image of the upper port IRVB with frame 139 and (b) the radial profile of the toroidal number 6 by the IRVB at $t = 2.09$ s. (c) the radial profile by the resistive bolometer at $t = 2.09$ s.

140

(a)

(b)
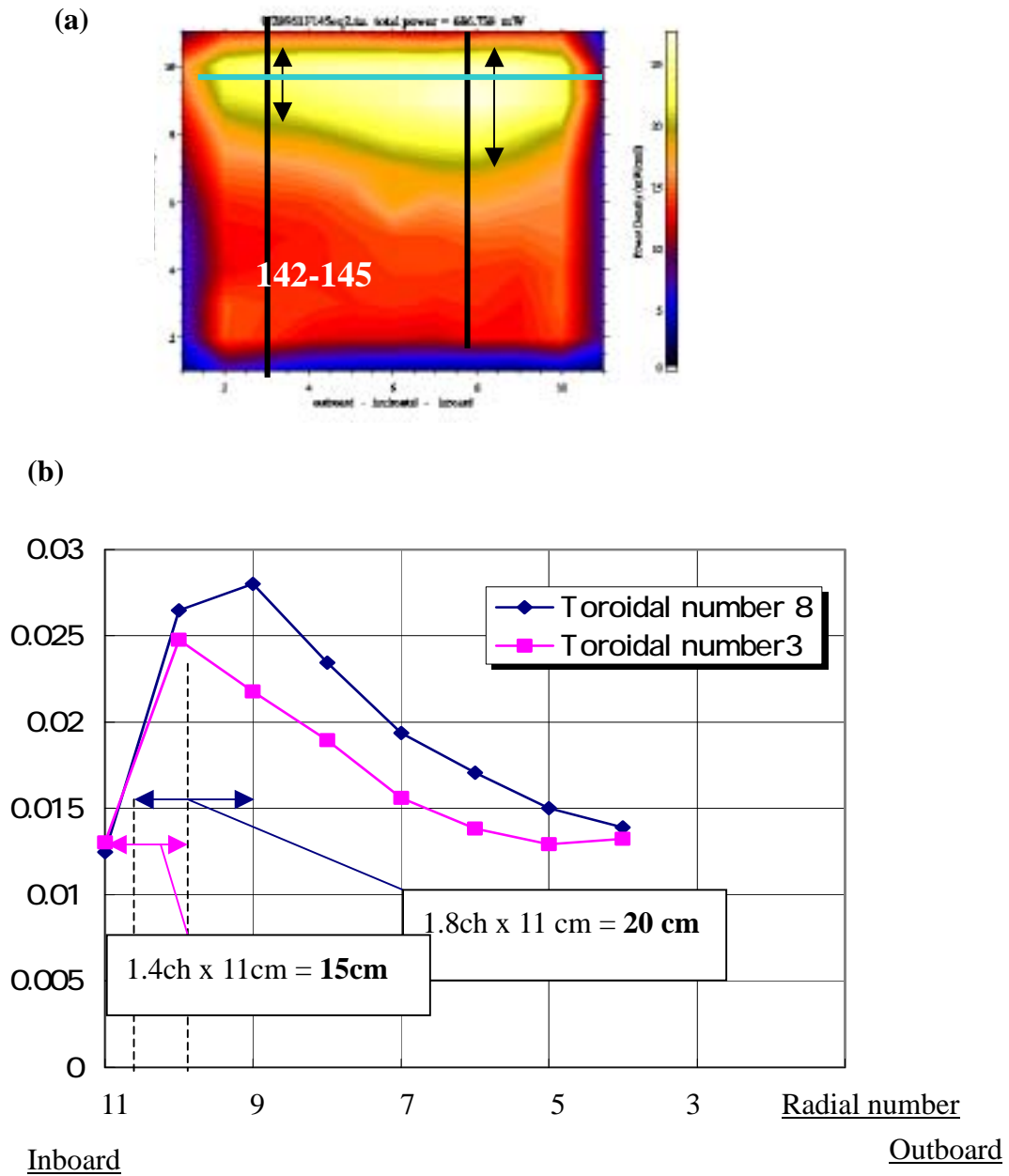
Fig. 5.3.18(a) The image of the upper port IRVB frame"143-145"during the collapse and (b) radial profiles on the toroidal number 3 and 8 using data of (a). the FWHM of the high radiation region is calculated about 15 cm at toroidal number 3 and 20 cm at toroidal number 8.
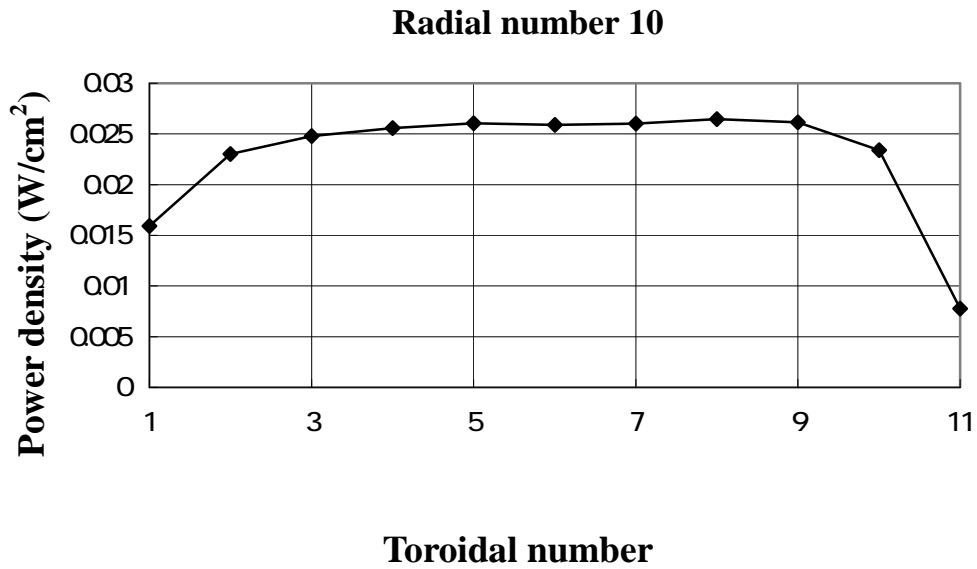
Radial number 10

Fig. 5.3.18 (c) The toroidal variation using the image of the upper port IRVB with frame "142-145" during the radiation collapse.
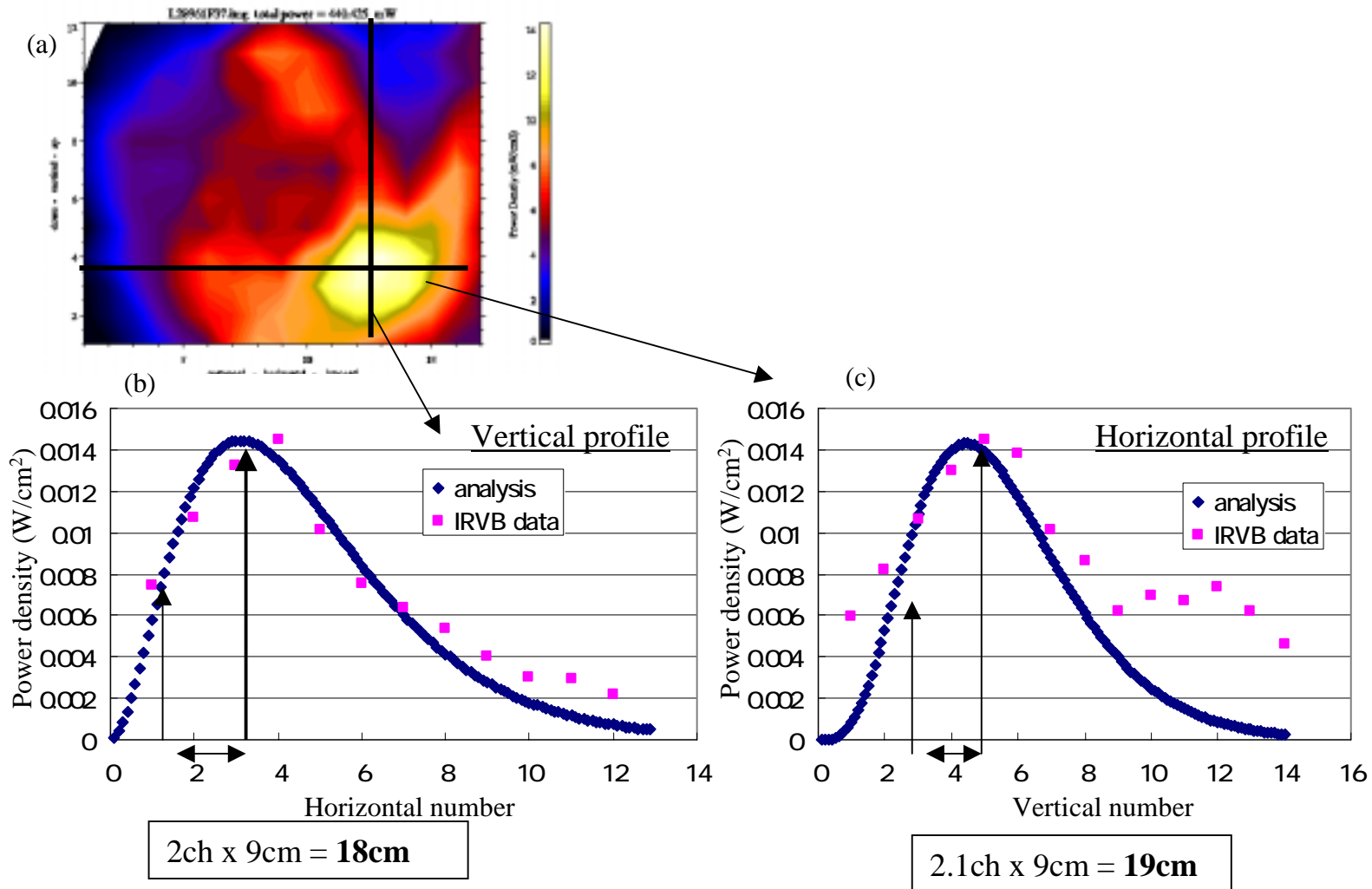
Fig. 5.3.19 (a)The image of the tangential IRVB frame 37 during the collapse. (b) The vertical profile at the vertical number 4 and (c) the horizontal profile at the horizontal number 13. Using Figs. (b) and (c) the FWHM on the high radiation region is calculated as about 18 cm and 19 cm.

(a) Outside port

Prior to collapse

During collapse

(b) Shot No. 28961, t= 2.09500 s

(c) Shot No. 28961, t= 2.16200 s

AXUVD 8O (mkW)

Channel No

bottom   top

bottom   top
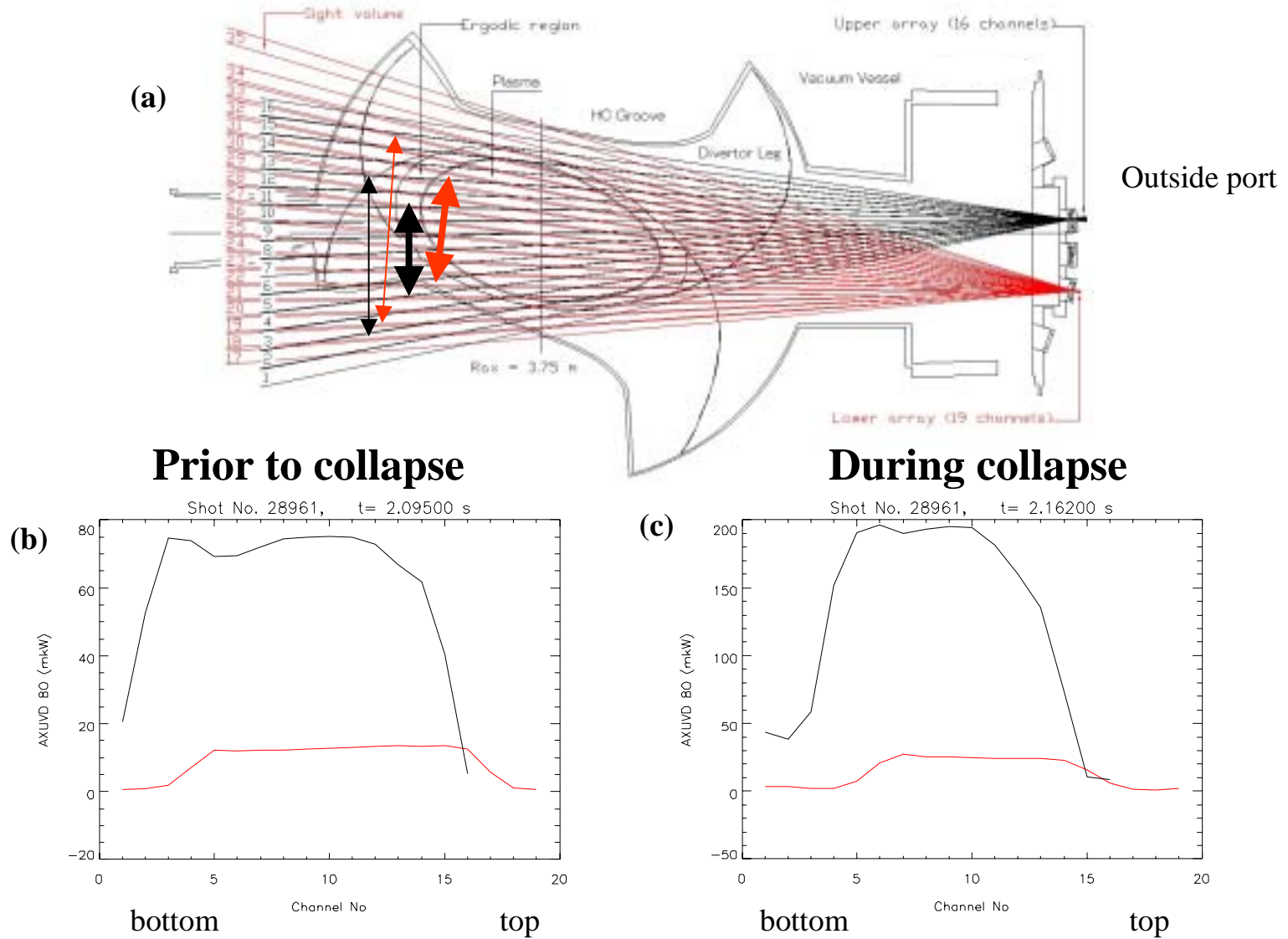
Fig. 5.3.20 AXUVD system with two arrays at Port 8-O (a) the FOV of each spatial channel and (b) brightness profiles before the collapse at *t* = 2.095 s, (c) brightness profiles during the collapse at *t* = 2.162 s for discharge #28961 (by B.J. Peterson and A. Koustrioukov)

5.4 Simulation of asymmetric radiation collapse with three-dimensional structure

Using the both IRVB data as shown in Fig. 5.3.12, the brightness radiation region during the asymmetric collapse was considered. For the simple model, the brightness radiation region was estimated as a belt at the inboard side of the vacuum vessel with a constant poloidal angle.

Figure 5.4.1(a) shows the model of the hollow profile using the estimated typical radiation profile, $S(\rho)$. From $S(\rho)$, the images of both IRVBs are calculated as shown in Figs. 5.4.1(d) and (e) by considering the FOV of the each spatial channel of the IRVB. The detected radiation power density, P_i, at each pixel, i, is given as follows,

$$P_i = \sum_j \frac{\Omega_{ij}}{4\pi} V_{ij} S_j \qquad (5.4.1)$$

where, Ω_{ij} is the solid angle for each channel, S_j is the volume emissivity, V_{ij} is the intersecting volume of i-th detector and j-th plasma volume. From the comparison of the image of the IRVB, (b), and the model, (d) for the tangentially viewing IRVB, in particular the thick ergodic region of the FOV of the IRVB showed the high radiation that is in good agreement for both figures. From the comparison of the image of the IRVB, (c), and the model, (e) from the upper port, the obviously toroidal asymmetry in detector brightness was observed and the right side on these figures at the inboard are shown the high radiation region. At the center of Fig. 5.4.1(c), one spatial channel measured a high temperature rise, this is probably due to the condition of the foil as can be seen in Fig. 3.1.2.4, not caused by radiation.

As a model of the radiation during radiative collapse, the hollow profile was multiplied by a poloidally asymmetric function as shown in Eq. (5.4.2),

$$S(\rho,\theta) = S(\rho) \cdot [1 + F(\theta)] \ , \qquad \text{where} \quad F(\theta) = \left(\frac{1 + \cos(\theta - \theta_0)}{2} \right)^{50} \qquad (5.4.2)$$

The angle, θ, is the poloidal angle in standard toroidal coordinates. Figure 5.4.2(a) shows the case 1 of $\theta_0 = 180°$ in which the high radiation region is situated at the inboard horizontal midplane,

which is at a minimum distance to the inboard wall at the vertically elongated plasma cross-section as shown in Fig. 5.4.2(b). The widths of the high radiation belt at the midplane are about 20 cm x 20 cm. In addition, two other models, (c) and (e) were calculated with the radiation belt shifted in poloidal angle. In Fig. 5.4.2(c) the radiation region is shifted 45 degrees ($\theta_0 = -135°$) as case 2 to a position below the horizontal midplane as shown in Fig. 5.4.2(d). For each poloidal cross-section (constant toroidal angle), the same poloidal angle was kept. In case 3, the radiation belt was shifted 45 degrees ($\theta_0 = 135°$) above the horizontal midplane as shown in Fig. 5.4.2(e).

These results using an axisymmetric radiation belt as an asymmetric radiation model are shown in Figs. 5.4.3. The simulation results from the tangential view, (a), (b) and (d) show the high radiation region clearly above, at, or below the midplane depending on θ_0. But the simulation results from the upper port show interesting structures, basically the right side on this figure shows the brightness region where the plasma rotated as shown in Fig. 5.4.3(e, f, h). From the comparison of the simulation result and the image of the IRVB, the images of the IRVB, (c) and (g) are estimated as a similar to the model of $\theta_0 = -135°$. This result is in agreement with the results of the analysis in Sec. 5.3. But a more detailed consideration of this model should include finer steps in poloidal angle and a variation in the intensity in the toroidal direction.

The use of the images of both IRVBs at the tangentially viewing port and on the upper port makes possible a discussion of the three-dimensional radiation structure.
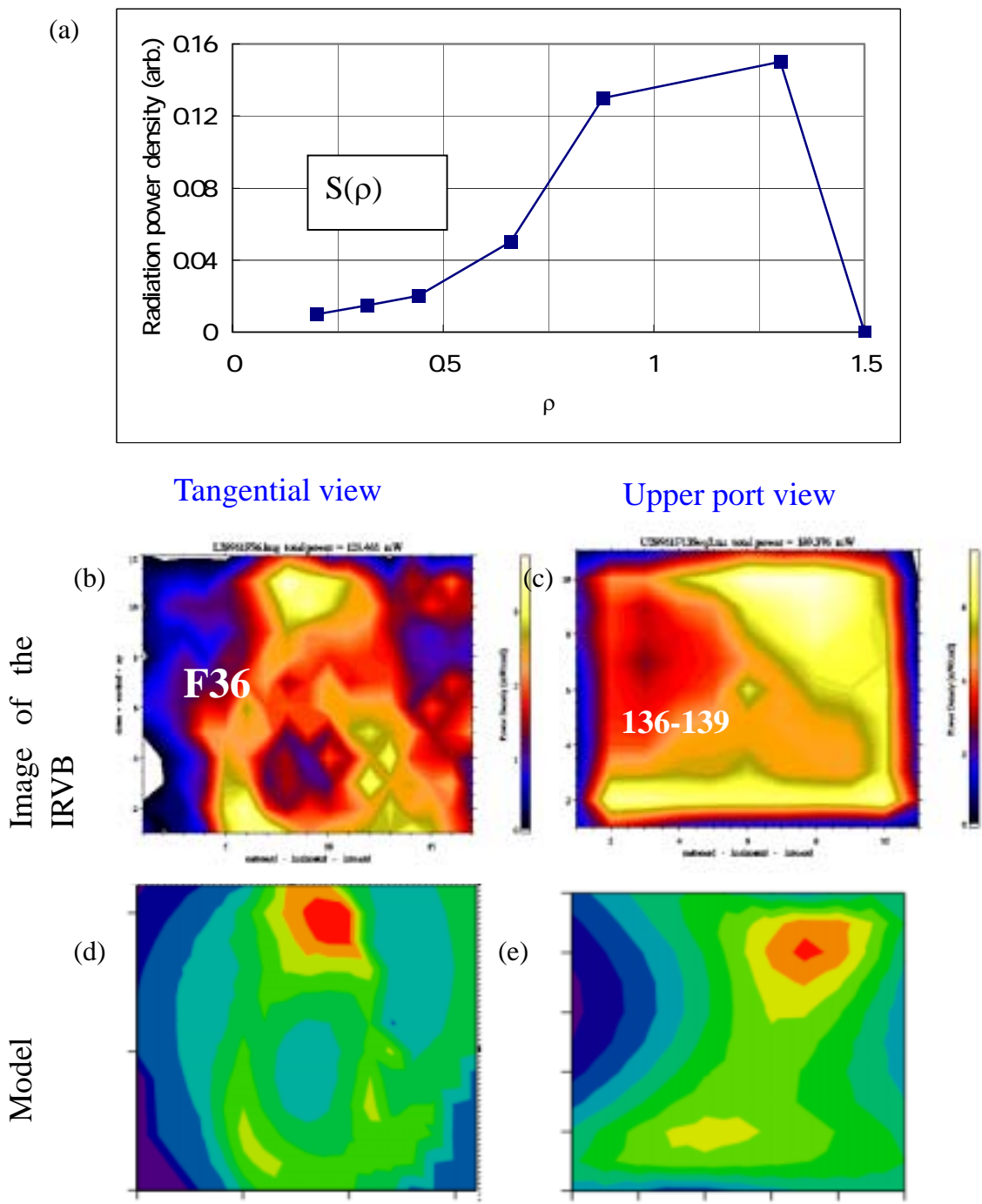
Fig. 5.4.1 (a) Model of the hollow profile using the estimated radiation profile. (b),(c) the images of the IRVB and (d),(e) the simulation result used the hollow profile as shown in (a).(modeling images (d) and (e) by A. Koustrioukov)

(a) Case 1; $\theta_0 = 180$

F(θ)

Poloidal angle θ

(b)

20 cm

20 cm

out   in

(c) Case 2; $\theta_0 = -135$

F(θ)

Poloidal angle θ

i   ii   iii

(d)

out   in

(e) Case 3; $\theta_0 = 135$

out   in
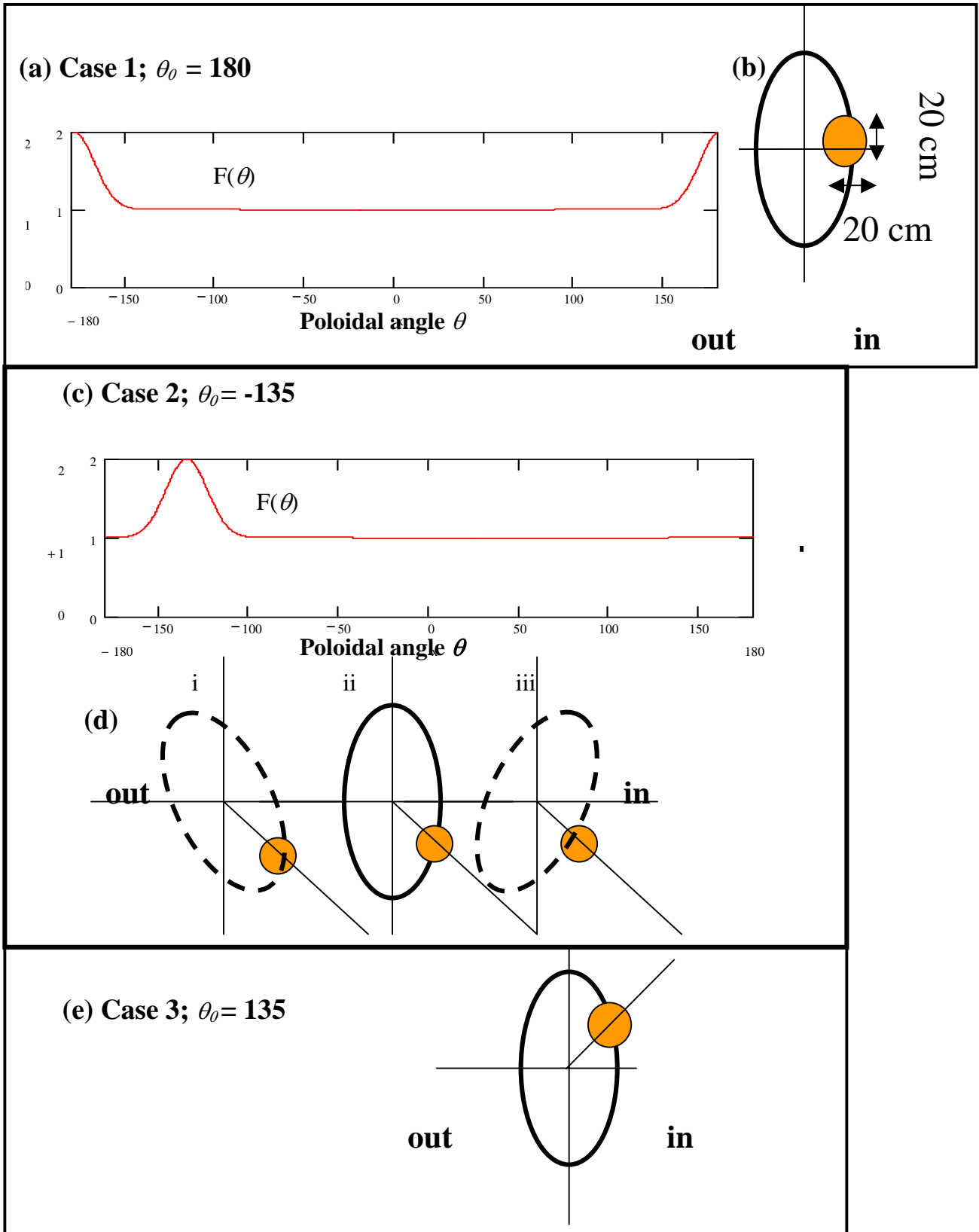
Fig. 5.4.2 Model of the brightness radiation belt at the inboard side. The different position of the belt is shown as (a) $\theta_0 = 180$, (c) $\theta_0 = -135$ and (e) $\theta_0 = 135$.

Tangential view   **Upper port view**

(a) Model $\theta_0 = 135$

(e)

(b) Model $\theta_0 = 180$

(f)

(c) Image of the IRVB — F37

(g) 142-145

(d) Model $\theta_0 = -135$

(h)
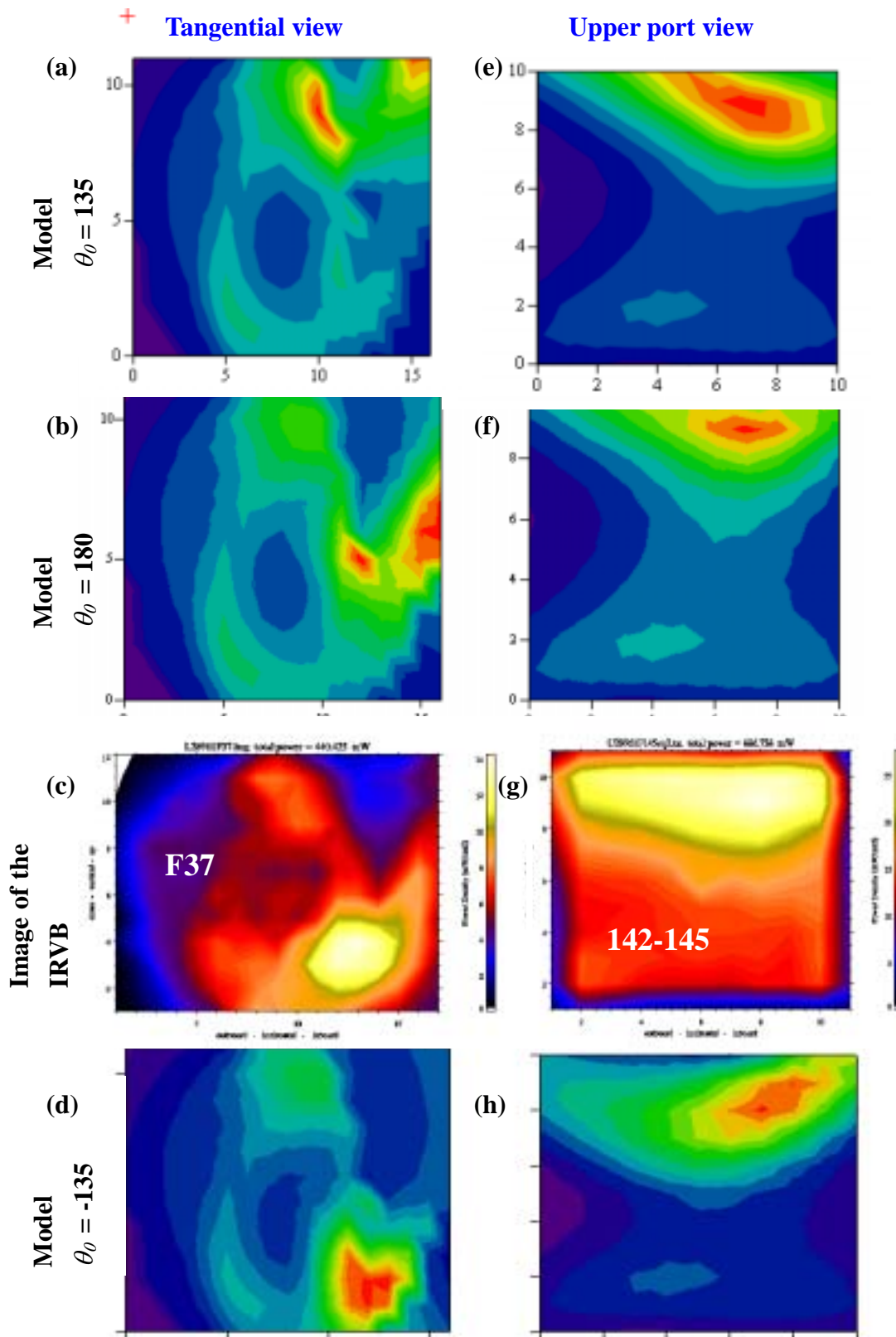
Fig. 5.4.3 Model simulation of the inboard asymmetric collapse. (c) and (g) are images of the IRVB at the tangential and the upper port ,(a) and (e) are model using $\theta_0 = 135$, (b) and (f) are using $\theta_0 = 180$ and (d) and (h) are model using $\theta_0 = -135$ (modeling images (a),(b),(d),(e),(f) and (h) by A. Koustrioukov).

## 5.5   Discussion about the asymmetric radiation collapse in LHD

For the plasma discharge for LHD shot #28961 in 2001, the asymmetric radiation collapse was observed as shown in Chapter 5. Using these results in this chapter, the LHD plasma during the radiation collapse is seen to have a strong radiation source at the inboard side and this radiation source region extends widely around the toroidal position of the vertically elongated cross-section at the inboard side. This three-dimensional position using two IRVBs is located under the midplane along the inboard side around the vertically elongated cross-section. This information could not be measured by other types of bolometers, and is the original information from the IR bolometer system.

From these results, four new pieces of the information were obtained, studied and shown as follows;

1. A series of two-dimensional images like a movie was made by the IR bolometer of the radiation brightness intensity.

2. The wide FOV images from the upper port are shown and using this data the toroidal and radial variation could be shown.

3. From both IRVBs from the tangential and the upper ports, the three-dimensional information on the position of the high radiation region during the collapse is shown.

4. Using a model including the full magnetic structure on the LHD, the possibility of investigation by comparing experimental images and a radiation distribution model is shown.

For the first point, continuous images are shown in Fig. 5.3.3 and Fig. 5.3.6 and using a PC the movie can be shown by these images. From these images, the characteristic structures of the plasma radiation are shown and they are easier to intuitively understand. During the collapse, using the IRVB data at 60 Hz from at the upper port as in Fig. 5.3.6, the motion of the radiation source from the inboard wall to the core plasma are shown.

For the second point, some new radiation profiles for the LHD plasma were shown in Chapter 5. For comparison with the radial profiles from the resistive bolometer, the upper IRVB can observe about 11 chords for the radial direction at present. The upper IRVB also can observe the toroidal variation as shown in Fig. 5.3.6. For hollow profiles, the upper IRVB measured a broad high radiation brightness region widely and during asymmetric collapse the upper IRVB measured the localized high radiation region from the inboard side.

The radiation signals from the resistive bolometer could not show the three-dimensional information of the position, but by the two IR bolometer systems the position of the high radiation brightness region was inferred in Chapter 5. Using this information an axisymmetric model of the high radiation region based on the full three-dimensional structure of the magnetic field was made and using the geometric information of the IR bolometer chord data the two-dimensional brightness profiles of the two IRVBs were reconstructed from this radiation source model.

From the modeling simulation as shown in Sec. 5.4, the case of locating the high radiation region on the inboard side under the midplane shows good qualitative agreement with the measurements.

For the toroidal variation during the collapse, the radiation power density on the image of the IRVB during the collapse shows that the right side on the image on the 5-O side is higher than the left side but this difference is small. Seeing the modeling simulation, a more axisymmetric structure was shown in Fig. 5.4.3. In the future the toroidal variation should be considered. This simulation tested only a large poloidal angle pitch of 45 degrees with symmetry for the toroidal direction, the actual high radiation region may have a more complex structure and variation. But information is observed on the three-dimensional position by the IR bolometer, and a new style of study of the asymmetric collapse and MARFE has been started by using the model of the total radiation from of the three-dimensional structure of LHD.

The effect of the plasma –wall interaction for the asymmetric collapse and MARFE can not be

clearly answered at present, but the highest point during the collapse is not the nearest point from the plasma to the first wall which is an interesting result for LHD discharge #28961. In addition from frame 37 of the tangential IRVB the high radiation region during the collapse appeared at about $\rho = 0.6 - 0.8$. However these conclusions are not definitive at this point.

To answer the question about the relationship between the asymmetric radiation collapse and the wall interaction, in the next 6th LHD campaign, the FOV of the tangentially viewing IRVB will be changed to cover all channels of the upper IRVB from the FOV of the tangential IRVB. In other words, the region "A" as shown in Fig. 5.3.4 will have to be measured and in order to compare the toroidal channel 2 from the upper port with the new FOV from the tangential IRVB around horizontal channel 10.

6　Conclusion

In this thesis, the development of the IR bolometer and the three-dimensional position of the asymmetric radiation collapse using the two IRVBs in LHD were discussed.

In Chapter 1 different types of bolometers in LHD and the two types of IR bolometer that were first developed in NIFS were shown. The IR bolometer is a new bolometer system to measure the plasma radiation using the IR camera and has two different systems, the Segmented mask Infrared imaging Bolometer (SIB) and the Infrared Imaging Video Bolometer (IRVB). The difference between these systems is the type of mask used to absorb radiation. With the mask and metal foil installed inside the vacuum vessel, the IR camera measures the temperature rise on the foil. The IR bolometer system does not have a vacuum feed-through and measures wide two-dimensional images with over 100 spatial channels.

In Chapter 2 the development of the IR bolometer system was shown. Mainly the details of the system hardware were shown in Chapter 2 and in particular the effect of the magnetic field by the superconducting coils in LHD was a big problems for the IR cameras but these problems were solved through experience with the magnetic field.

In Chapter 3 more details of the image data from the IR bolometer were shown. A calibration method was used for the first experiments and data of the IR bolometer show the plasma radiation power density profiles. From this calibration, the noise equivalent power (NEP) of both types of IR bolometers was determined and the first result from the LHD plasma using the SIB system were shown. The limitations of spatial and time resolutions were also shown. Basically the time resolution depends on the frame rate of the IR camera and the number of the spatial channels and the time resolution of the IRVB depend on the noise equivalent power density (NEPD). As a criterion for the sufficient value of the NEPD, 1 mW/cm^2 was used. For the IRVB data, each spatial channel was determined by the numerical algorithm. At present the forward time center space algorithm was used for images but other algorithms were also considered with their errors. From the

results of the errors, the Crank-Nicholson was found to be best algorithm and in the future the Crank-Nicholson algorithm will be used. In addition the applicability to future large devices was shown. One problem of the neutron effects during D-D or D-T plasma experiments was the common problem for the resistive bolometer and from the differences of the system the IR bolometer will be considered to be stronger than the resistive bolometer.

In Chapter 4 some good images of the tangential IRVB were shown during the radiation collapse, the wall limiter experiment and the movable limiter experiment from only one IRVB at the tangential port. To understand the radiation structure on LHD, the comparison of the IRVB image with the hollow profile and the magnetic field calibration launched in the region around the last closed magnetic surface ($\rho = 1$) was shown. From this result, the high radiation point with the hollow profile on the image from the tangential IRVB depending on the thickness of the ergodic region was understood.

In Chapter 5 images during the asymmetric radiation collapse in LHD were shown from the upper port IRVB and the tangential port IRVB. The FOV of the tangential IRVB covered the FOV of the upper IRVB. The asymmetric collapse at the inboard side in LHD was already observed by the resistive bolometer and the characteristics were similar to MARFE in tokamak. The resistive bolometer measured just the vertical elongated plasma and the horizontal elongated plasma but continuing structures during the asymmetric collapse between each cross-section were not observed yet. For this question, using the merit of the IR bolometer, many images of both IRVBs were shown to see the changing radiation structure and using two IRVBs the three-dimensional position of the asymmetric radiation during the collapse was determined. To determine the images having the same timing some discussions about the observed characteristics of the radiation structures and the relationship of the both images were shown. From the results it was estimated that the high radiation region was located at the inboard side and under the midplane.

For more discussion, the comparison of the images of the IRVB and the model calculation with

the localized radiation source at the inboard side was shown. This result also showed the high radiation region during the collapse at the inboard side and under the midplane. In addition a discussion of the three-dimensional structure of the plasma radiation has become possible by comparing the images of two IR bolometers with the results of a model calculation.

From the many results of this thesis, the usefulness of the IR bolometer and its ability to measure the three-dimensional radiation structure during the asymmetric collapse were demonstrated.

References

[1] O. Motojima *et al., Phys. Plasmas* 6 (1999) 1843.

[2] A.W Leonard *et al., J. of Nucl. Mater.* **220-222** (1995) 325-329.

[3] B.J. Peterson, *et al., Nucl. Fusion* **41**,519 (1999)

[4] S. Morita *et al., Physica Scripta*, **T91** (2001) 48-52.

[5] H.J. Karr *et al., Phys. Fluids* **4**, 424 (1961).

[6] H. Hsuan *et al., Nucl. Fusion* **15**,657 (1975).

[7] J. Schivell *et al.*, *Rev. Sci. Instrum* **53** (1982) 1527.

[8] A.W. Leonard *et al., Rev. Sci. Instrum* **66** (1995) 1201.

[9] G. Apruzzese and G. Tonini, *Rev. Sci. Instrum.* **61** (1990) 2976.

[10] R. Maqueda *et al., Rev. Sci. Instrum.* **63**, (1992) 4717.

[11] R.L. Boivin *et al., Rev. Sci. Instrum* **70** (1999) 260.

[12] G.A. Wurden, B.J. Peterson and S. Sudo, *Rev. Sci. Instrum.* **68** (1997) 766.

[13] G.A. Wurden and B.J. Peterson, *Rev. Sci. Instrum.* **70**, (1999) 255.

[14] B.J. Peterson, *Rev. Sci. Instrum.* **71** (2000) 3696.

[15] B.J. Peterson, N.Ashikawa *et al., Rev. Sci. Instrum* **72** (2001) 923.

[16] K.F. Mast, H.Krause, *et al., Rev. Sci. Instrum.* **56**, (1985) 969.

[17] P.E. Stott *et al*. eds., G.A. Wurden *et al.,* "*Diagnostics for Experimental Thermonuclear Fusion Reactors*", (Plenum, New York, 1996), pp. 603-606.

[18] B.J. Peterson, N.Ashikawa *et al., IEEE Trans. Plasma Sci*. **30(1)** (2002) (in press).

[19] M.N. Ozisik, *"Boundary Value problems for Heat Conduction",* (International Textbook, Scranton, 1968), Eq. 3-100, p.152.

[20] W.H. Press, *et al.," Numerical Recipes, the Art of Scientific Computing"*, (Cambridge University Press, Cambridge, 1986), pp. 635-642.

[21] N. Ashikawa, B.J. Peterson *et al., J. Plasma Fusion Res. SERIES* **3** (2000) 436.

[22] F.P. Incropera and D.P. Dewitt, *" Introduction to heat transfers third edition*", (John Wiley & Sons, Inc.,1985), pp.609.

[23] T. Masuzaki, private communication, (1999).

[24] E.R. Muller and F. Mast, *J. Appl. Phys.* **55** (1984) 2635.

[25] B.J. Peterson, *et al., J. Plasma Fusion Res. SERIES* (ITC-8), **1** (1998) 382.

[26] H.S. Carslaw and J.C. Jaeger, *" Conduction of Heat in Solids"*, (Oxford Science Publications, 1946) pp.171.

[27] F.P. Incropera and D.P. Dewitt, *" Introduction to heat transfers third edition",* (John Wiley & Sons, Inc.,1985), pp.767.

[28] B.J. Peterson, private communication, (2001).

[29] P.R. Bevington and D.K. Robinson, *"Data Reduction and Error Analysis for the Physical Science"*,(McGraw-Hill, Boston, 1992), pp.38-52.

[30] R. Reichle, *et al., 28th EPS conference on controlled fusion and plasma physics* (2001).

[31] B.J. Peterson, Yuhong Xu, *et al., Phys. Plasmas* **8** (2001) 3861.

[32] Yuhong Xu, B.J. Peterson *et al., Nucl. Fusion* **42** (2002) (in press).

[33] N. Ashikawa, B.J. Peterson *et al., J. Plasma Fusion Res. SERIES* **4** (2001) 437.

[34] T. Watabnabe and H. Akao, *J. Plasma and Fusion Res.,* **73** (1997) 186 (in Japanese)

[35] N. Ashikawa, B.J. Peterson *et al., 28th EPS conference on controlled fusion and plasma physics* (2001).

[36] B. Lipschultz *et al., Nuclear Fusion* **24** (1984) 977.

[37] B. Lipschultz *et al., Phys. Rev. Lett*. **81** (1998) 1007.

[38] P.C. Stangeby *et al.,"The plasma boundary of magnetic fusion devices*", (Institute of Physics Publishing, 2000), pp.603-614.

[39] T. Ishijima et al*., Plasma Phys. Control Fusion* **41**(1999) 1155.

[40] J.W. Connor and S. You*, Plasma Phys. Control Fusion* **44**(2002) 121.

[41] M.Z. Tokar, *Phys. Plasmas* **6** (2001) 2866.

[42] J. Rapp, *et al*., *Nucl. Fusion* **39**,765 (1999).

[43] U. Samm and the TEXTOR-94 Team*, Plasma Phys. Control Fusion* **41**(1999) B57.

[44] F.A. Kelly, W.M. Stacey and J. Rapp, *Phys. Plasmas* **8** (2001) 4879.